This is to certify that the

dissertation entitled

PROPERTIES OF STEADY-STATE, HIGH

PRESSURE ARGON MICROWAVE DISCHARGES

presented by

James Rustin Rogers

has been accepted towards fulfillment
of the requirements for

Ph.D. degree in Electrical Engineering

Major professor

Date 8/10/82

PROPERTIES OF STEADY-STATE, HIGH PRESSURE, ARGON MICROWAVE DISCHARGES

By

James Rustin Rogers

A DISSERTATION

Submitted to
Michigan State University
in partial fulfillment of the requirements
for the degree of

DOCTOR OF PHILOSOPHY

Department of Electrical Engineering and Systems Science

1982

ABSTRACT

PROPERTIES OF STEADY-STATE, HIGH PRESSURE
ARGON MICROWAVE DISCHARGES

By

James Rustin Rogers

This dissertation examines experimental properties of steady-state argon microwave discharges in the pressure range of 40-1300 torr. The discharges were sustained inside a cylindrical cavity by microwave fields from a well filtered, 2.46 GHz, variable power microwave source. Quartz tubes located coaxially in the cavity were used to contain the discharges and all experiments were conducted with no flow of argon gas inside the tubes. The discharges can be characterized as being contracted, filamentary discharges with diameters of 1-3 mm and lengths up to 16 cm. The principal objectives were to determine discharge properties and to observe the general behavior of these filamentary discharges in a microwave cavity.

Electron density, effective collision frequency and electric field strength were diagnosed by numerically solving an EM plasma/cavity boundary value problem which closely approximated the experimental geometry. Measurements required as inputs to this analysis were the cavity resonant length shift, average discharge diameter, total power absorbed by the cavity and calibrated electric field strength at a reference point in the cavity. Cold plasma theory was used to describe the conductivity in the discharges. Gas temperatures were calculated using a radial heat conduction model and electron temperatures were calculated from the effective collision frequencies assuming a Maxwellian velocity distribution function. Typical

discharge properties at 1 ATM were electron densities of $3 \times 10^{13}/cm^3$ to $3 \times 10^{14}/cm^3$, effective collision frequencies of $1\text{-}3 \times 10^{10}$/sec, gas temperatures of 1100-1300 ^{o}K, electron temperatures of 6000-17,000 ^{o}K and microwave electric field strengths of 27-30 v/cm.

Two related experimental investigations are also included as reference material in the dissertation. High pressure standing surface wave discharges were generated in argon, krypton and xenon gases. These filamentary discharges exhibited many similarities to the argon filaments generated in the cylindrical cavity. Also, low pressure argon microwave discharges were investigated by extending the cylindrical cavity experiment down to pressures between .02 and 1.0 torr. Properties of these diffusion controlled discharges compared well to argon microwave discharges diagnosed with other methods.

To My Father

A. Barde Rogers

ACKNOWLEDGEMENTS

The author is grateful for the encouragement and guidance received from Dr. Jes Asmussen throughout the duration of this investigation. A special note of thanks also goes to Dr. Dennis Nyquist for assistance in several aspects of guided electromagnetic wave problems and for numerous helpful discussions.

This research was supported in part by fellowships from the Schlumberger Foundation and the Michigan State University Graduate Office and by a grant from the NASA/Lewis Research Center.

TABLE OF CONTENTS

LIST OF TABLES

LIST OF FIGURES

ABBREVIATIONS AND NOTATION

EM	electromagnetic
rf	radio frequency
GHz	gigahertz (10^9 cycles/sec)
MHz	megahertz (10^6 cycles/sec)
KW	kilowatt
ATM	atmosphere
e	Charge on electron
m_e	mass of electron
σ	conductivity
β	propagation constant
ε	permittivity
ε_o	permittivity of free space
μ_o	permeability of free space
ω	radian excitation frequency
ω_p	radian plasma frequency of the electron gas
$\vec{E}$	electric field
$\vec{H}$	magnetic field
$\lvert\vec{E}\rvert$	peak absolute value of electric field
E_p	plasma electric field (peak absolute value)
E_e	effective electric field
N_e	electron density
ν_e	effective electron-neutral collision frequency
T_e	electron temperature

T_g	gas temperature
Eff	microwave coupling efficiency
Q	quality factor of a resonator
Q_u	unloaded cavity Q
Q_L	loaded cavity Q
P_i	incident power to cavity
P_r	reflected power from cavity
P_t	total power absorbed by cavity
P_p	power absorbed by the plasma
P_c	power absorbed by the coupling structure
<P>	absorbed power density in plasma
p	gas pressure
p_o	reduced pressure
d_{ave}	average plasma diameter
ΔL	resonant cavity length shift
L_s	cavity length between shorting planes
L_p	excitation probe depth

CHAPTER I

INTRODUCTION

This dissertation describes a detailed experimental investigation into high pressure argon microwave discharges. These discharges can be characterized as being steady-state, weakly ionized plasmas with contracted diameters of 1-3 mm and lengths up to 16 cm. A single cylindrical microwave cavity mode was used to both couple energy into the discharges and diagnose discharge properties. The pressure domain of the experiments was 40-1300 torr and all experimental results are for non-flowing discharges.

The main objectives were to: (1) study the formation of contracted discharges in a microwave cavity, (2) determine the efficiency of coupling microwave power to the discharges, and (3) generate detailed information about argon discharge properties (such as electron density, effective collision frequency and discharge electric field strength). To achieve these objectives, initial experiments were performed to understand the general behavior of the discharges in a microwave cavity and the orientation that the discharges take in different cavity modes. As the experiments progressed, it became apparant that in certain cavity modes the experimental plasma/cavity geometry could be mathematically modeled. Thus, the main focus of the experiments became one of diagnostics; i.e. the discharges were generated in well defined microwave fields in a single cavity mode and the interaction of the discharges with those fields was measured and analyzed.

Although the emphasis of this dissertation is placed on high pressure

argon discharges generated in a cylindrical cavity, two related experimental investigations are described in the appendices. High pressure standing surface wave discharges in argon, krypton and xenon were investigated using a similar diagnostic philosophy. The characteristics of these surface wave filamentary discharges exhibited many similarities with those generated in the cylindrical cavity. Also, low pressure argon microwave discharges were investigated in the cylindrical cavity by extending the experimental techniques (which were independent of gas pressure) down to pressures between .02 and 1.0 torr. These low pressure results were compared to other argon microwave discharges diagnosed with different methods.

The overall layout of the disseration is as follows. Chapter II contains a detailed literature review of other steady state microwave discharges produced at atmospheric pressure. Chapter III describes the experimental system, basic operation of a microwave cavity for sustaining a plasma and several measurements that were made on the cavity EM fields and on the discharges. General observations about the argon discharges are presented in Chapter IV. These observations provide necessary background information for understanding the EM and plasma analysis contained in Chapter V. Discharge properties such as electron density, collision frequency, gas temperature, electron temperature, plasma electric field and coupling efficiency are described in Chapter VI. Overall conclusions and some recommendations for further research are given in Chapter VII. Finally, the appendicies contain the high pressure standing surface wave results (Appendix A), the low pressure argon results (Appendix B) and some basic equations related to the analysis of the discharges (Appendix C).

CHAPTER II

REVIEW OF STEADY-STATE, ATMOSPHERIC PRESSURE MICROWAVE DISCHARGES

2.1 Introduction

This chapter reviews significant work on steady-state, high pressure microwave discharges. Emphasis is placed on discharges produced at 1 ATM for later comparison with experimental results of this dissertation. General reviews of microwave discharges for other pressure regimes are documented elsewhere [1,2].

A microwave coupling structure is a device designed to focus electromagnetic energy onto a plasma. Coupling structures can be classified according to the principal type of EM wave phenomena used by the device to transfer energy to the plasma [2]. These types are:

(1) radiating waves or evanescent fields (non-guided EM waves),

(2) fast EM waves (phase velocity greater than the speed of light), and

(3) slow EM waves or surface waves (phase velocity less than the speed of light).

The review contained in this chapter is organized according to the classification described above. Although a given coupling structure is usually designed for one type of electromagnetic coupling, it can often transfer energy to a plasma through a combination of types of waves [2]. Examples of this will be pointed out in the review.

2.2 Discharges Sustained by Radiating Waves or Evanescent Fields

The most common coupling structure using this type of EM wave phenomena has been called a coaxial microwave "torch" [3] or "plasmatron" [4]. Figure 2.1 describes a coaxial torch showing the location of the discharge and giving representative dimensions [5]. Microwave power in a TEM mode propagates down the coaxial line toward the open end. The center conductor is tapered at the end to aid in focusing the electric field. The discharge is ignited by drawing a small spark from the center conductor tip. Axial gas flow keeps the discharge from arcing to the outer conductor and extends the discharge out from the end of the torch. With higher and higher levels of absorbed power, the axial gas flow eventually becomes insufficient to prevent arcing. Experimentally, this limit has been put at a power level of 10 KW [6]. Discharges produced in a coaxial torch are similar to lower frequency unipolar discharges [7].

In 1951, Cobine and Wilbur reported experimental results on atmospheric pressure discharges produced in a coaxial microwave torch [3]. Their device was coupled directly from a magnetron cavity in which 1 KW tubes of varying frequency (.5 - 1.1 GHz) were used. Impedance matching was accomplished with a stub tuner on the magnetron cavity and a telescopic section in the coaxial line. Gases used in the discharges were CO_2, He, He(+.3% H_2) N_2, O_2, A and air. A discharge was attempted in pure hydrogen but was not successful. A pyrex nozzel was used on the end of the torch to stablize the gas flow and the discharge. The optimum flow rate was reported at 70 ft/min linear velocity at the exit of the torch.

Quantitative measurements by Cobine and Wilbur were limited.

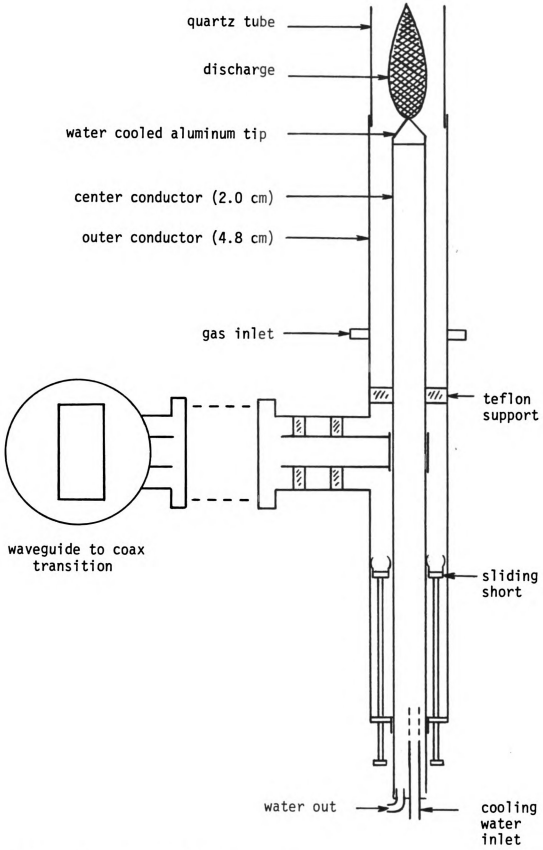

Figure 2.1 Coaxial microwave torch

Electrical probe characteristics were taken by inserting a small, air cooled nickel probe into a nitrogen discharge. Using standard single probe theory, the electron temperature was estimated at 10^5 ^oK and the electron density at $10^9/cm^3$. Treating the probe characteristics as conductivity data, a different estimate of $10^{13}/cm^3$ was made for electron density. Estimates of gas temperature in a nitrogen discharge were made using a bouyant force method and resulted in a range of 1900 - 3700 ^oK.

Cobine and Wilbur made numerous qualitative observations on the visual appearance of the discharges, differences in the different gases, and the effect of the discharges on center conductor tip materials. Photographs of the discharges are included in the paper. A typical nitrogen discharge of absorbed power approximately 350 watts was 2 cm long and about .5 cm in diameter, looking very similar to a horizontal flame. An important observation by Cobine and Wilbur was that discharges in the monatomic gases (argon and helium) were cool compared to discharges in the polyatomic gases. This difference was attributed to the molecular dissociation - recombination mechanism, allowing the coupling of more power per unit volume into the polyatomic gas discharges.

In 1974, S. Miyake, et al., published a detailed investigation of a nitrogen discharge at atmospheric pressure produced with a coaxial torch [4]. Their power source was a 3 KW, CW magnetron operating at 2.45 GHz. Power was coupled into the torch through a rectangular waveguide system containing a circulator, standing wave meter, directional couplers and a waveguide to coaxial transition. A water cooled tungsten electrode formed the tip of the center conductor. A quartz tube extended out of the torch in order to stablize the gas flow. Axial flow rates were 30 - 200 liters/min.

Miyake made several types of quantitative measurements. Power transmitted to the discharge and to radiation was measured as incident minus reflected power using the directional couplers. Electron density was measured in N_2 + 5% H_2 by spectroscopically measuring the Stark broadening of the H_β line. Radiated power from the end of the torch was estimated with a small loop antenna. Impedance was measured using the standing wave meter. Relative spectral intensity measurements of the H_β line were made and reported in arbitrary units. Using the electron density measurements, electron temperature was determined from the Saha-Eggert equation assuming local thermal equilibrium in the discharges.

A typical nitrogen plasma at 2 KW transmitted power was 10 cm long and about .5 cm in diameter. The maximum temperature was 6700 ^{o}K and the maximum electron density was 7 x $10^{13}/cm^3$. Several graphs are reported showing axial profiles of plasma temperature, electron density, microwave radiation and spectral intensity. Radial distributions of temperature and emission intensity are also reported. The functional dependence of plasma properties on transmitted power and gas flow rate are presented.

In 1975, Batenin, et al., described an atmospheric pressure hydrogen discharge produced with a coaxial torch [8]. The power source was a variable power, 5 KW magnetron of frequency 2.45 GHz. The transmission system and method of impedance matching was similar to Miyake's, except that no directional couplers or standing wave meter were included. A quartz tube containing the discharges extended out of the end of the torch. A significant difference is this coupling structure as compared to those previously described was the placement of a resonant cavity on the end of the torch. The power transmitted to the discharge was

reported to be enhanced by proper adjustment of the cavity length. Thus, the actual microwave coupling to the discharges probably represented a combination of evanescent fields and fast waves. The cavity walls and center conductor were water cooled and all power absorbed measurements were made calorimetrically on the cooling water.

The principal diagnostic techniques employed by Batenin were spectroscopic methods. The major point of the article was to generate spectroscopic data on atmospheric pressure hydrogen microwave discharges in order to compare with earlier controversial results by Kapitza [9] (described in the next section). A detailed description of Batenin's equipment and spectroscopic analysis is given in the article. The results for a 2 KW discharge were an electron density of $3.5 \times 10^{15}/cm^3$, electron temperature of 10,000 ^oK and a gas temperature of 8500 ^oK. Batenin's conclusion was that the discharge represented a cold, weakly ionized, nearly equilibrium plasma.

2.3 Discharges Sustained by Fast EM Waves

Coupling fast EM waves to a high pressure discharge usually involves the use of a microwave cavity. A rectangular resonator, similar to the one used in reference [6] is illustrated in Figure 2.2 and a cylindrical cavity is described in detail in Chapter III. A simple description of a cavity is that it consists of a section of waveguide (supporting fast waves) terminated by two short circuits, forming a standing wave. Power is coupled into the cavity through probe or loop excitation or by aperture coupling from another waveguide. When a plasma is generated inside a resonant cavity, the Q usually drops significantly (indicating that power is now being absorbed mainly by the discharge instead of the cavity

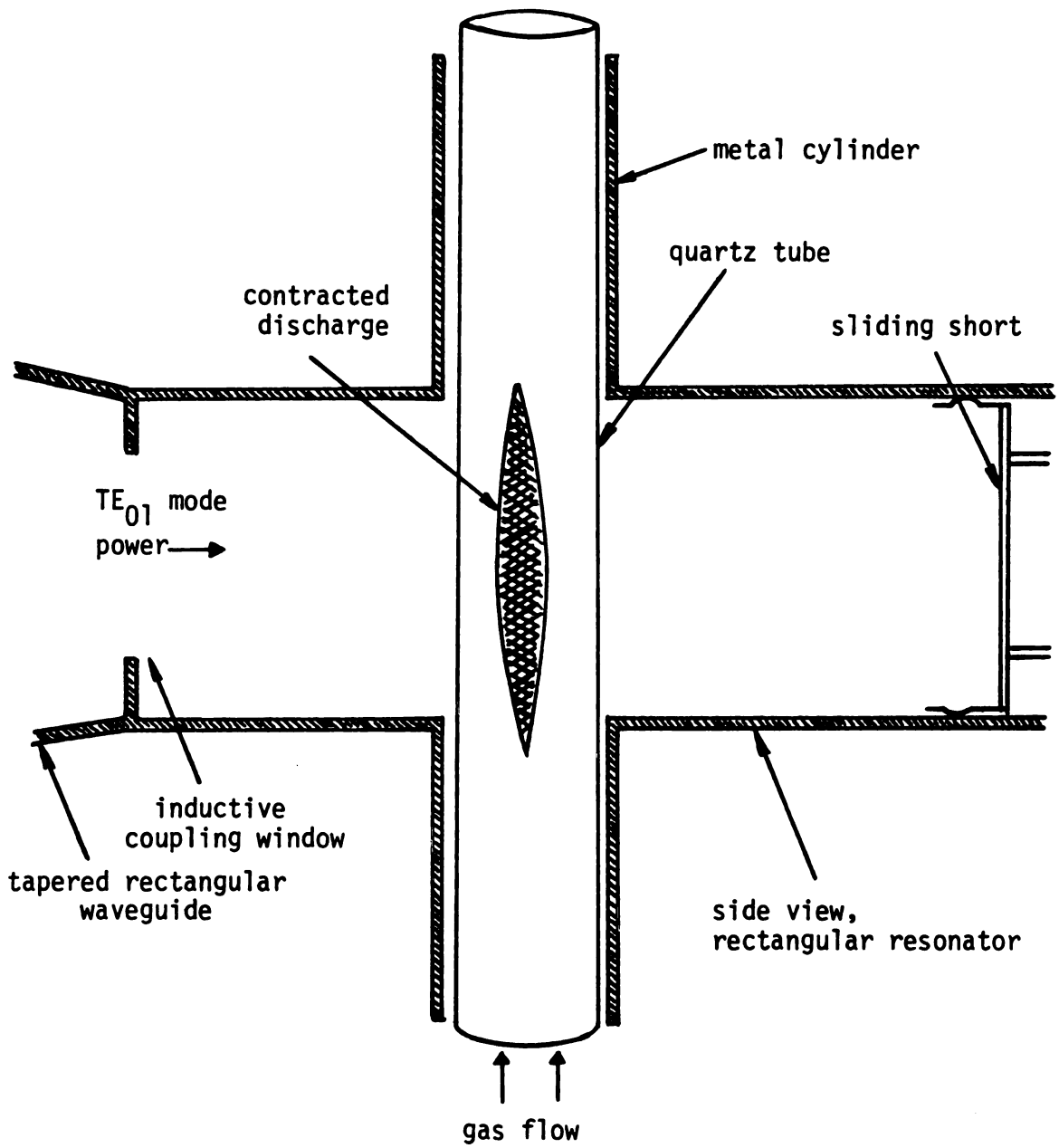

Figure 2.2 Retangular resonator for coupling fast EM waves to a plasma column

walls) and the dispersion characteristics change (requiring frequency tuning or cavity length tuning). In simple plasma/cavity geometries, these effects can be modeled mathematically. Thus, the microwave cavity can also be used as a diagnostic tool. General descriptions of microwave plasma/cavity operation are given in references [10,11]. An important note is that the discharges described in this section are electrodeless as compared to those generated by a coaxial torch.

From 1950-1970, P.L. Kapitza led an investigation of hydrogen microwave discharges at atmospheric pressure. A 1970 paper [9] summarized his experimental system, results and conclusions; and a 1972 paper [12] described in more detail his apparatus and measurement techniques. The experiment consisted of a 175 KW magnetron of frequency 1.55 GHz, aperture coupled to a 20 cm diameter cylindrical cavity. The cavity was operated in a TM_{01n} cavity mode which has a maximum of longitudinal electric field on the cavity axis. Length tuning of the cavity was accomplished with a sliding short around which electrical contact was made with a hydraulically inflatable thin walled copper tube. Cavity walls and sliding short were water cooled and power absorbed to the discharge was determined calorimetrically on the cooling water. The cavity was sealed by using air cooled quartz windows over the coupling aperture and over small observation holes on the cavity wall. Pressures up to 5 ATM could be maintained with most of the experimental work being done at 1-2 ATM.

Discharges were ignited by placing a small tungsten wire attached to a quartz rod near the center of the cavity. The tungsten wire was rapidly rotated parallel to the longitudinal electric field and then quickly removed to prevent melting. Once ignited, the discharges tended to float upwards due to the bouyancy force. To maintain the discharges

"freely floating" in the center of the cavity, a gas circulation system was used. Typical contracted hydrogen discharges (or "filaments") were described as being about 1 mm in diameter and several centimeters long. The filaments formed most easily in and were parallel to the maximum longitudinal E-field in the center of the cavity. Plasma length increased with power to a maximum of about 10 cm (1/2 the resonator wavelength). Further increases in power caused the diameter to increase until the filament broke up into two shorter and thinner filaments. Discharges were obtained in absorbed power levels up to 20 KW. A large drop in cavity Q due to the plasma was determined by measuring relative strengths of electric field inside the cavity. These measurements indicated that most of the power was absorbed by the discharges and little was lost directly into the cavity metal walls.

Kapitza's diagnostics were primarily emission spectroscopy. Electron density was measured from Stark broadening for absorbed power levels below 10 KW and were of the order of $10^{15}/cm^3$. Above 10 KW, the magnitude of the Stark broadening decreased to where at 17 KW the electron density was calculated to be only on the order of $10^{13}/cm^3$. Kapitza concluded that this phenomena was due to a masking effect by a cloud or sheath of cold plasma surrounding a dense hot filament. To obtain density information for power levels above 10 KW, a specially designed spectrometer for use in the infared region was constructed. At 12.4 KW, an electron density of $7.3 \times 10^{15}/cm^3$ was determined with this method where Stark broadening gave only $1.4 \times 10^{13}/cm^3$. The optics employed by Kapitza were refined enough to give emission intensity distributions transversely across the filament (where the dimension was about 1 mm).

Electron temperature was estimated in two ways and presented the

most controversial results. An intense continuous spectrum of radiation in the wavelength range of 1050-1350 $\mathring{A}$ was observed. Assuming this radiation to be bremsstrahlung, relative emission intensities corresponded to an electron temperature of 10^6 ^oK - indicating a "hot" or fully ionized core of the plasma filament. Using the electron density information and assuming the existence of a hot core of plasma surrounded by a cold equilibrium sheath, the electron temperature was calculated to be 10^6 - 10^7 ^oK for the core and 6 - 7 x 10^3 ^oK for the sheath. To account for this large temperature discontinuity, Kapitza proposed the existence of a double layer of charge (or space charge sheath) on the boundary of the hot plasma core. This double layer was assumed to be sufficiently strong to contain energetic electrons within the core.

In analyzing Kapitza's spectroscopic data, Dymshits and Koretskii [13] reached a different conclusion regarding the electron temperature of the hydrogen filaments. For a wavelength region of 1050 - 1250 $\mathring{A}$, they calculated the relative contributions of recombination radiation and bremsstrahlung for a cold, equilibrium plasma (electron temperature of about 10^4 ^oK). It was found that the intensity of the recombination spectrum was much greater than the intensity of the bremsstrahlung, and that the order of magnitude of the recombination spectrum was sufficient to explain Kapitza's experimental results. Dymshits and Koretskii also calculated the intensity contribution of the wings of the Lyman -α line (1216 $\mathring{A}$) for a temperature of 9000 ^oK and concluded that this factor must also be considered in explaining the experimentally determined radiation intensities. After pointing out other experimental results of Kapitza that indicate that the temperature of the discharges was low, Dymshits and Koretskii concluded that the hydrogen filaments were most probably cold, equilibrium discharges.

Arata, et al., investigated atmospheric pressure microwave discharges in nitrogen (1976) [6] and in hydrogen (1978) [14]. Both studies used the same experimental system and basic measurement techniques. The power source was a 30 KW, .915 GHz magnetron. A rectangular waveguide system containing a circulator, directional coupler and an E - H tuner transported microwave power to a rectangular resonator, similar to the one illustrated in Figure 2.2. Incident microwave power could be varied continuously up to the maximum of 30 KW. The coupling structure was water cooled in the vicinity of the discharge tube and absorbed power to the discharges was determined by calorimetry on the cooling water. Impedance matches were good with only a few percent of the incident power being reflected. All powers were reported in incident power with the understanding that the absorbed power was at least 80% of the incident power. A helical flow of gas was necessary to keep the discharges centered in the pyrex tube which ran transversely up through the resonator (as indicated in Figure 2.2). The discharges were ignited by a movable tungsten wire which was removed from the discharge tube after ignition.

At an incident power level of 5 KW, the length of the nitrogen discharges filled the transverse section of the resonator. Upon adding more power, the length and diameter of the discharges continued to increase. At 20 KW, the length was approximately 30 cm. The size of the pyrex discharge tube was found to have a large effect on nitrogen discharge diameters. For example, in a 20 KW discharge the diameter was 1.5 cm in a 4 cm diameter pyrex tube but only .5 cm in a 2 cm pyrex tube. Tube size also affected plasma properties (diagnostics were the same as Miyake, et al., [4]). For the 20 KW discharge in the 4 cm tube, electron density was $1.3 \times 10^{14}/cm^3$ and plasma temperature was 6300 ^{o}K.

At the same power in the 2 cm tube the electron density was $3.5 \times 10^{14}/cm^3$ and the temperature increased to 6800 ^oK.

Results of Arata in hydrogen made more extensive use of equilibrium and nearly equilibrium plasma modeling. An extensive discussion of the spectroscopic results was included in the paper along with a comparison with the conclusions of Kapitza. A typical hydrogen plasma produced by Arata was 1 mm in diameter and 20 cm in length at a power level of 20 KW. The electron density was $5 \times 10^{15}/cm^3$ and the electron temperature was 8900 - 12,000^oK depending on the plasma model. Arata reached the same conclusion as Batenin and Dymshits that atmospheric pressure hydrogen filamentary discharges were cold, nearly equilibrium, weakly ionized discharges.

The fact that Arata's hydrogen and nitrogen discharges extended well outside the rectangular resonator (into the transverse cylinder) indicates the presence of energy transfer from the fast wave inside the resonator to another type of traveling wave. Arata suggested that this traveling wave was a TEM wave with the plasma acting as the center conductor of a coaxial line. However, as was pointed out by Moisan [15], the more probable explanation is that the traveling wave was a surface wave.

2.4 Discharges Sustained by Slow EM Waves

A surface wave launcher that has been used to produce high pressure microwave discharges is shown in Figure 2.3 [16]. This coupler consists of a coaxial cavity with a short gap between the center conductor and front cavity wall. Microwave power is introduced into the cavity through a microcoaxial line, terminated by an excitation loop. Upon proper

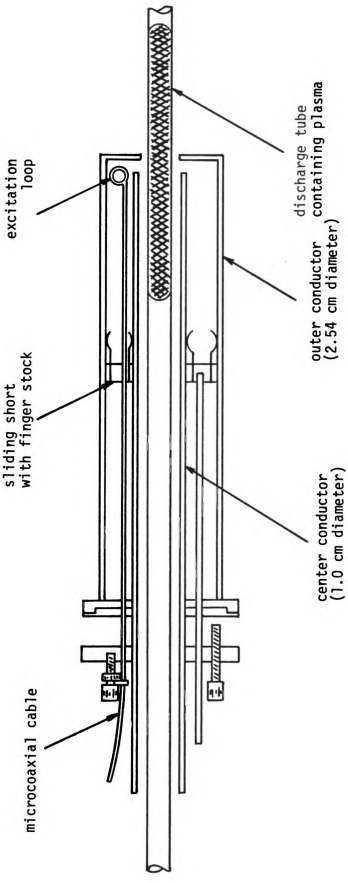

Figure 2.3 Coaxial re-entrant cavity

adjustment of the cavity, intense electric fields are generated in the gap region causing breakdown of the gas in the quartz tube (which runs coaxially inside the center conductor). After breakdown, the microwave electric fields launch traveling surface waves extending the plasma column away from the gap. Since the traveling wave is transferring energy into the plasma, it attenuates. When the wave is insufficiently intense to maintain a high enough electron density in the plasma, the wave is cut off and the plasma column ends.

In 1979, Hubert, et al., reported on properties of atmospheric pressure surface wave discharges in argon gas [17]. Using the surface wave launchers similar to Figure 2.3, Hubert investigated discharges over the frequency range of .28 - 1.7 GHz. Their coupling structure was called a "surfatron" [18]. All discharges were contained in thin quartz tubes ranging from .5 - 5.0 mm inner diameter. Little external cooling of the tube or internal gas flow rate was needed to prevent melting of the quartz. A coaxial type transmission system transported power from the oscillator to the surface wave launchers. Power absorbed was measured using directional couplers and power meters located in the transmission system. Absorbed powers ranged from 50 - 150 watts for most of the experimental results reported in the paper.

A 100 watt argon discharge in a 5 mm tube was approximately 14 cm long with a contracted diameter of approximately 1 mm. Flow rate of gas produced little change in discharge dimensions in the 5 mm tube. Keeping the absorbed power constant, a small increase in plasma diameter was noted with increasing frequency. Electron densities were measured in argon + .5% H_2 using Stark broadening. The addition of hydrogen did not affect the macroscopic appearance of the argon discharges. Electron

densities of 2 - 5 x $10^{14}/cm^3$ are reported depending on absorbed power. Gas temperatures were estimated in argon + .3% N_2 using a spectroscopic measurement of a N_2 rotational line. In this case, the addition of nitrogen greatly affected the appearance of the discharge by causing its length to decrease to about 1/2 of the length in pure argon for the same power level. Typical rotational temperatures were 2100 - 2800 ^oK depending on input power. Neither the electron density nor the rotational temperatures were affected by excitation frequency.

In a 1980 paper [15], Moisan et al., continued the investigation of atmospheric pressure argon surface wave discharges. Stark broadening measurements of electron density were compared with densities obtained with numerically generated dispersion curves. Treating the plasma as a homogeneous, lossy dielectric, the dispersion curves were obtained by solving the EM boundary value problem for surface wave propagation. The electron densities obtained in this manner were about 50% lower than those determined from the Stark broadening. Both measurements represented an average electron density over the cross section of the discharge and the discrepancy between the results was not explained.

2.5 Literature Review Summary

Properties of the atmospheric pressure microwave discharges reviewed in this chapter are summarized in Table 2.1. Average power densities were calculated from information given in the papers.

experiment	gas	electron density l/cm^3	power density w/cm^3	electron temperature ^oK	gas temperature ^oK	coupling structure
Cobine [3]	N_2	$10^9 - 10^{13}$	1200	10^5	3700	coaxial torch
Miyake [4]	N_2	5.0×10^{13}	1300	-	6500	
Batenin [8]	H_2	3.0×10^{15}	1.4×10^4	10,000	8500	
Kapitza [9]	H_2	7.3×10^{15}	1.2×10^5	10^6	9000	cavity
Arata [6]	N_2	4.0×10^{14}	5000	-	6800	
Arata [14]	H_2	5.0×10^{15}	1.3×10^5	12,000	9000	
Hubert [17]	A	3.5×10^{14}	900	-	2500	surface wave launcher
Moisan [15]	A	6.0×10^{14}	2600	-	-	

Table 2.1 Summary of atmospheric pressure microwave discharge properties for the literature reviewed in Chapter II.

CHAPTER III

EXPERIMENTAL SYSTEM, MEASUREMENTS AND PROCEDURES

3.1 Introduction

The experimental system to be described in this chapter consists of: (1) a microwave circuit for generation, transmission and measurement of microwave power; (2) a cylindrical cavity for transferring the microwave energy to the discharges; and (3) a quartz tube for containing the discharges in varying gas pressures and flow rates. This system is very similar to one described in detail by Fritz [1]. Since the microwave cavity is used to both generate and diagnose the discharges, a section concerning its performance as a resonator is included. Also described in this chapter are the basic measurements made on the plasma and the cavity fields for use in diagnosing discharge properties.

3.2 Description of Experimental System

The microwave circuit is described in Figure 3.1. The power source was a well filtered, 2.459 GHz, variable power (0 - 500 watts) magnetron. When operated above approximately 30 watts, frequency drifts of the source were less than 0.5 MHz. Microwave power from the source was coupled into a rectangular waveguide system containing a water cooled ferrite circulator and two 20 dB directional couplers. A 30 dB attenuator and a power meter were attached to each directional coupler. The incident power was isolated from the reflected power as shown in the figure. There was no measureable attenuation or cross coupling in the circulator, ensuring that power readings of incident and reflected power in the

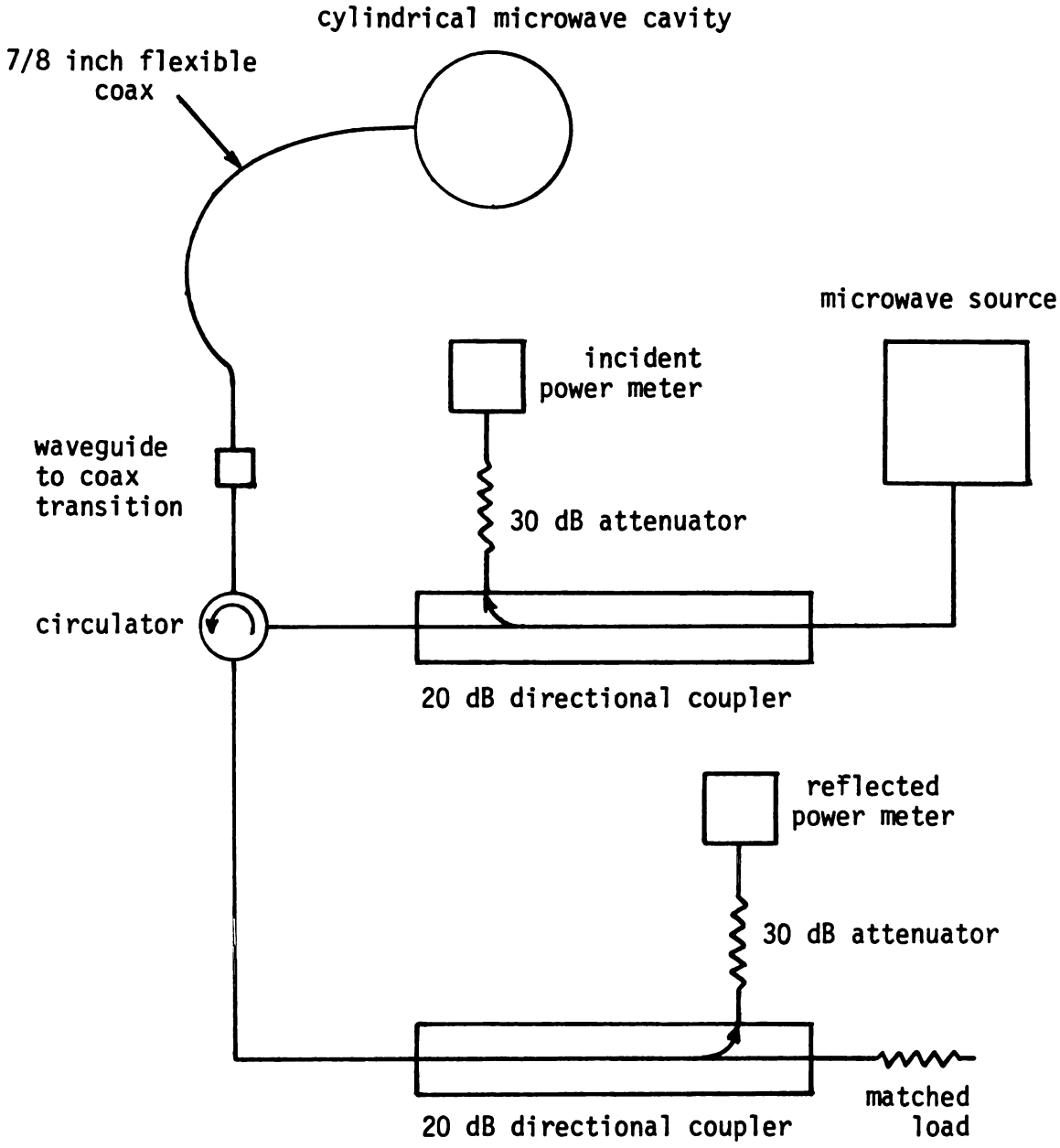

Figure 3.1 Diagram of microwave circuit

waveguide system were accurate.

Microwave power from the waveguide system was transported to the cylindrical cavity through a 7/8 inch flexible coaxial cable. Attenuation in this cable was measured to be approximately a .46 dB drop (measured through two waveguide to coax transitions). Coupling of microwave power into the cylindrical cavity was accomplished with a coaxial transition, shown in Figure 3.2, attached to the end of the flexible coax. Essentially, this transition extended the center conductor of the coaxial line into the cavity to a depth that could be manually varied. A series of fingers machined into the outer conductor of the transition provided excellent electrical contact with the coupling port of the cavity.

Figure 3.3 describes the microwave coupling structure. The resonant portion (or "cavity") was formed by the 17.8 cm diameter cylindrical brass pipe and the two transverse brass shorting planes (or "shorts"). One of the shorts was adjustable to provide a variable cavity length of from 6 to 16 cm. Water cooling was provided by copper tubing soldered on the brass pipe and the two shorts exterior to the cavity. The discharges could be viewed and photographed through a copper screened window. A rectangular brass piece was soldered onto the top of the coupling structure and seven E-field probe diagnostic holes spaced 1.8 cm apart were drilled through this piece and the cavity wall. A single hole was drilled through the fixed short as indicated in the figure to allow a shielded loop to be put into the cavity. The diagnostic probe and loop are described later in this chapter. Figure 3.4a defines the cavity length, L_s, and the coupling probe depth, L_p, for later use in the dissertation.

Quartz tubes of varying diameter were located coaxially in the

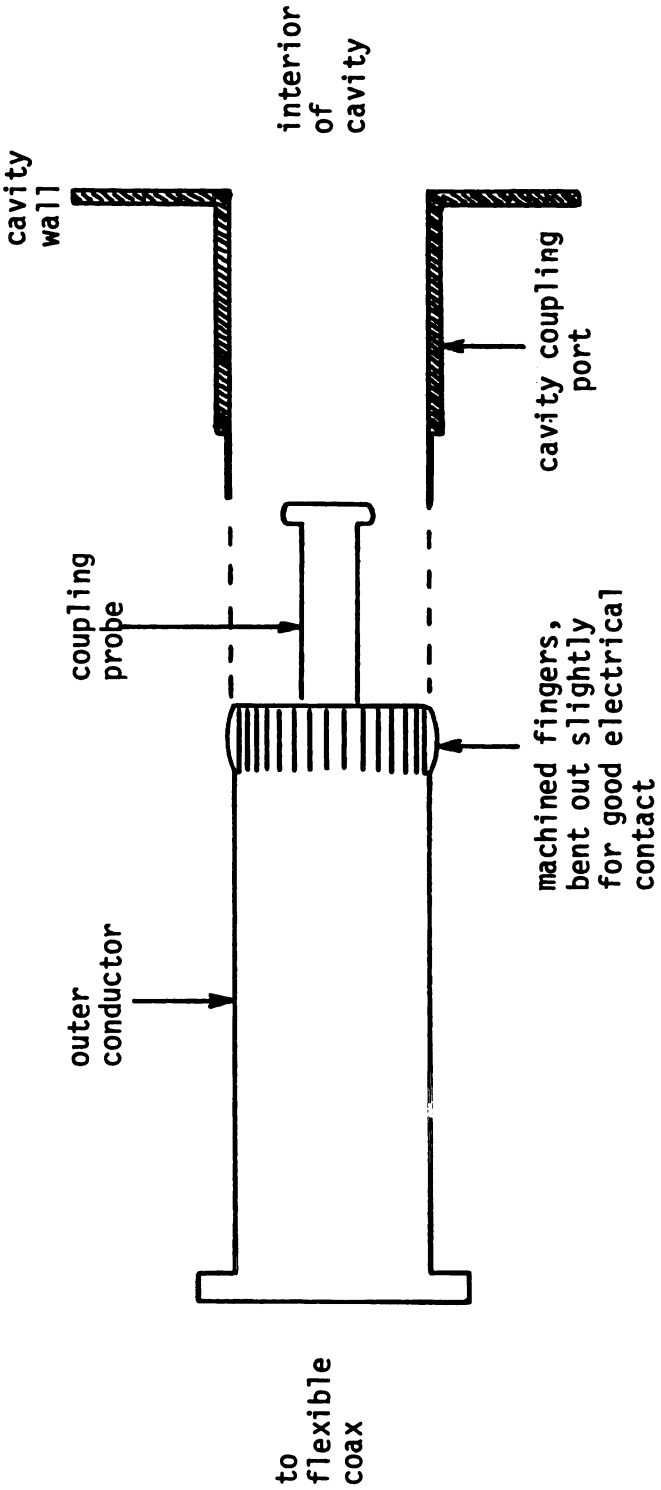

Figure 3.2 Variable depth excitation probe coupling system

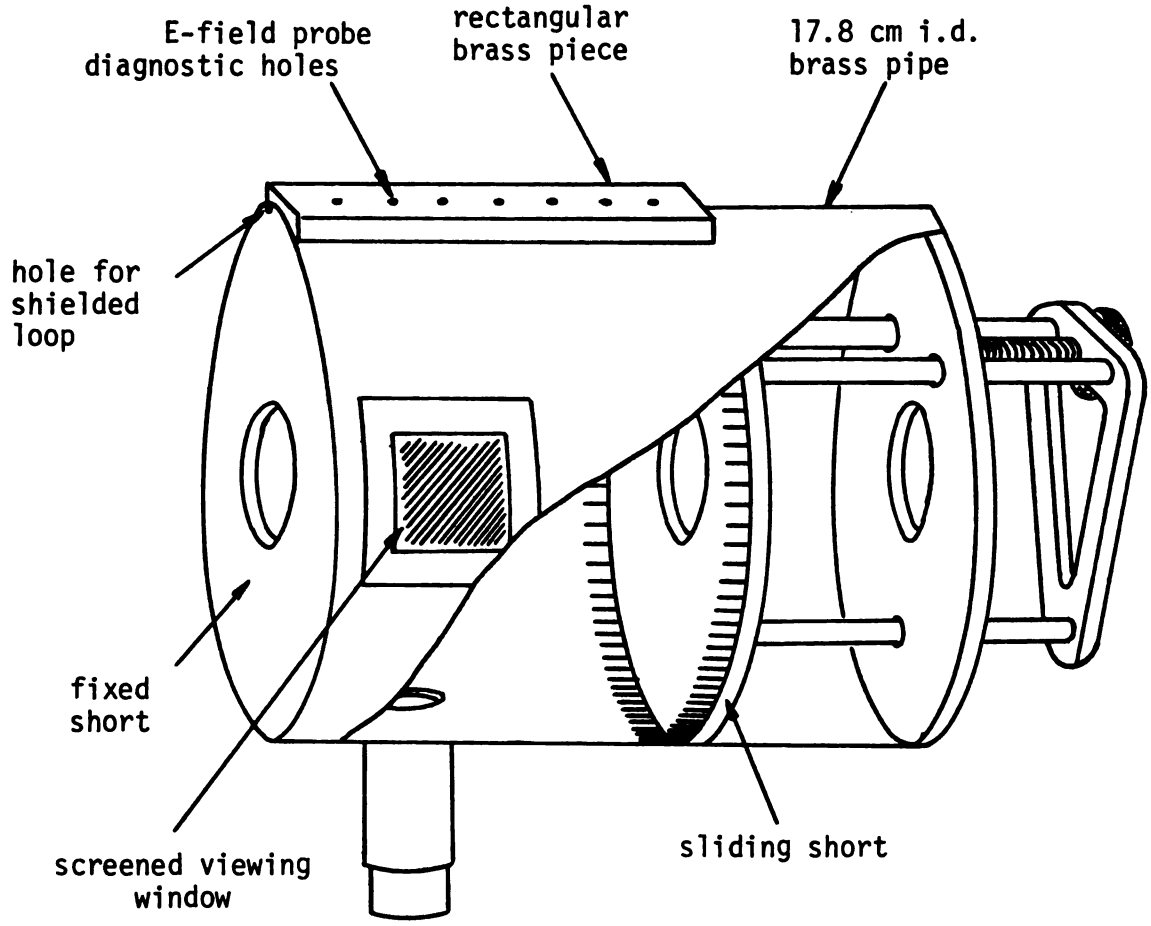

Not shown: (1) coupling port used in all experiments, located directly opposite screened window 3.7 cm from inside wall of fixed short. (2) copper cooling tubes on cavity exterior

Figure 3.3 Experimental cylindrical cavity

a. definitions of L_s and L_p

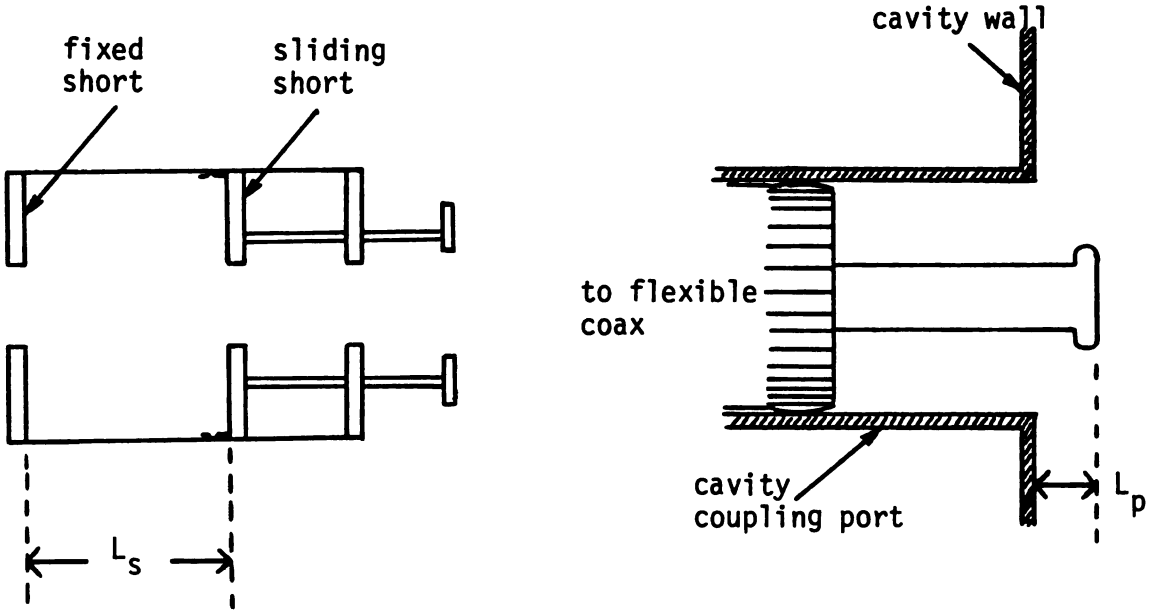

b. location of brass collars

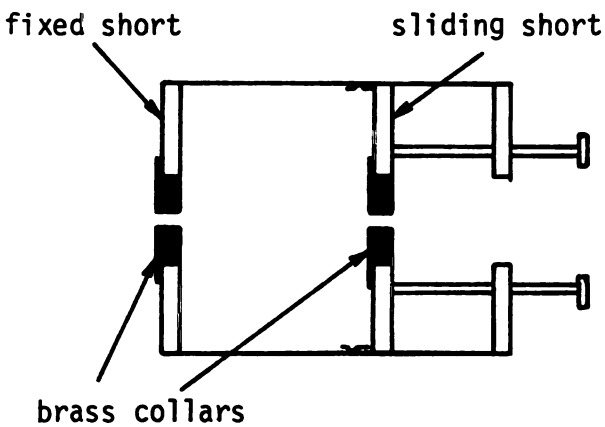

Figure 3.4 a. Definition of cavity length, L_s, and excitation probe depth, L_p. b. Location of brass collars if used in the experiments.

coupling structure. When tubes of 1.0 cm or less outside diameter were used, brass collars were inserted into the open holes on both the fixed short and the sliding short as shown in Figure 3.4b. The collars aided in maintaining the cavity mode field orientation in the region of the open holes as long as they were motionless and did not touch the quartz tube (which often vibrated). For quartz tubes larger than 1 cm o.d., the collars had little beneficial effect and were not used. For protection from microwave radiation, 5 cm diameter copper screen cylinders were attached around the open holes exterior to the coupling structure. The quartz tubes ran coaxially inside these screen cylinders.

The vacuum and flow systems are described in Figure 3.5. All experiments were done using argon gas and no measureable flow rate, although a slight amount of gas flow was actually present to ensure purity of the gas. A mercury manometer was used to measure gas pressures from 40 - 1300 torr. Prior to each experiment, the entire system was evacuated to approximately .001 torr, outgassed and flushed with argon.

3.3 Performance and Operation of the Cylindrical Cavity

3.3.1 Microwave Circuit Definitions

A simple description of a microwave cavity has already been given in Section 2.3. The basic theory of microwave circuits and cavities is given in many EM texts [19-21] and is omitted here. However, this dissertation makes use of some essential terminology which is described briefly below and in more detail in references [21-23].

(1) Resonance curve - a plot of power absorbed by the cavity or circuit as a function of frequency (for a fixed cavity length) or as a function of cavity length (for a fixed excitation

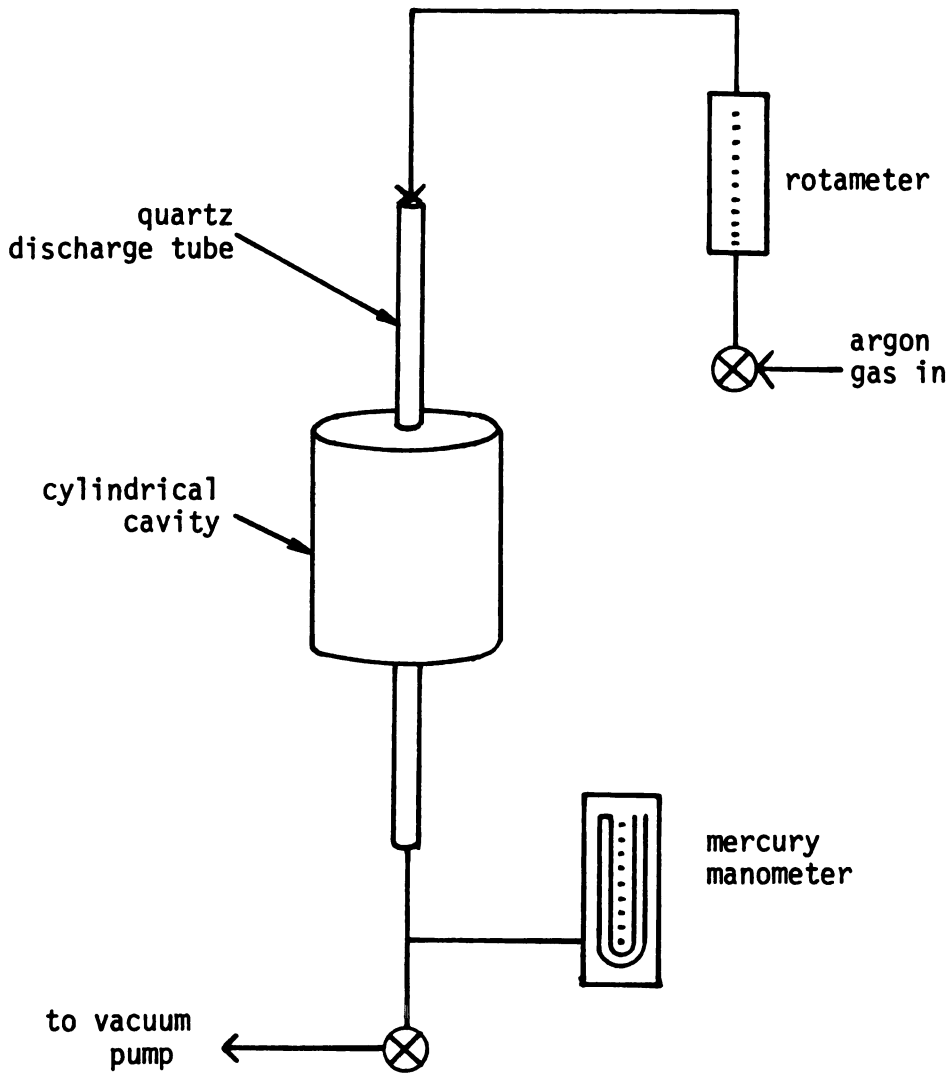

Figure 3.5 Vacuum and flow system

frequency).

(2) Critically coupled - the impedance looking into the cavity is matched to the transmission line at the resonant frequency. When this condition is met, all the incident power to the cavity at the resonant frequency will be absorbed and none will be reflected.

(3) Undercoupled and overcoupled - the impedance at the resonant frequency is not matched. When undercoupled, the real part of the cavity impedance is greater than that of the transmission line; and when overcoupled, the reverse is true.

(4) Unloaded cavity Q (Q_u) - an indication of the magnitude of losses in the cavity walls and in the dielectric (or plasma) contained in the cavity. Q_u can also be thought of as an indication of the frequency selectivity of coupling power into the cavity hypothetically not connected to the transmission line.

$$Q_u = 2\pi f_o \times \frac{\text{Stored energy in cavity}}{\text{Power dissipated in cavity}} = \frac{f_o}{\Delta f}$$

where f_o is the resonant frequency and Δf is the frequency width at the half power points on the cavity resonance curve.

(5) Loaded Q (Q_L) - essentially the Q of the cavity coupled to the external circuit. Q_L is normally measured and then related to Q_u.

$$Q_L = 2\pi f_o \times \frac{\text{Stored energy in circuit}}{\text{Power dissipated in circuit}} = \frac{f_o}{\Delta f}$$

where now Δf is defined in terms of the circuit resonance curve.

In definitions (4) and (5) above, the generic meaning of the word "loaded" is referring to the cavity acting as a load on the transmission line and is not referring to the presence or absence of dielectric losses in the cavity. Q_u will be used throughout the dissertation as the quality factor of the cavity which contains both metal wall losses and plasma losses and Q_{uo} will denote the unloaded cavity Q of the cavity without plasma present. Also, in the measurement of Q_L, the stored energy is approximately entirely in the cavity and the dissipated energy is approximately in the parallel conductances of the cavity and the source. When the cavity is critically coupled, $Q_u = 2Q_L$ and when nearly completely undercoupled $Q_u = Q_L$.

3.3.2 Experimental Empty Cavity Modes and Q_{uo} of the TM_{012} Mode

A resonant cavity is excited in discreet cavity modes. When the excitation frequency is fixed, the modes of a cylindrical cavity correspond to distinct cavity lengths (or eigenlengths). Table 3.1 lists the theoretical eigenlengths for an ideal empty cavity of the same dimensions as the experimental cavity at 2.45 GHz. Since any deviations in cavity geometry (such as the open holes or excitation probe) caused the ideal cavity mode to be perturbed, the experimental eigenlengths of the modes never exactly corresponded to theory. Table 3.1 also lists the experimental eigenlengths for the empty cavity with and without the

mode	theoretical eigenlength cm	experimental cavity without collars		experimental cavity with collars	
		L_{so} cm	L_{po} cm	L_{so} cm	L_{po} cm
TE_{111}	6.69	(1)		6.82	0.58
TM_{011}	7.21	7.43	0.22	7.29	0.24
TE_{211}	8.24	8.37	-0.27	8.40	-0.06
TE_{011}	11.27	11.24	1.90 (2)	11.27	1.90
TM_{111}	11.27	10.28 10.38	0.61 0.37 } (3)	11.57	1.15
TE_{112}	13.39	(1)		13.55	0.81
TM_{012}	14.41	14.56	0.00	14.47	0.12
TE_{311}	15.50	15.66	-0.08	15.67	-0.08

(1) could not identify mode

(2) not critically coupled

(3) two different resonances of the same dipole mode, polarity of fields different

Table 3.1 Theoretical cylindrical cavity mode eigenlengths compared with the experimental eigenlengths (L_{so}) for the empty cylindrical cavity with and without collars. Excitation frequency - 2.45 GHz. Probe depths (L_{po}) were those required for critical coupling unless otherwise noted. L_{po} varied slightly depending on Q_{uo}.

brass collars in place. The coupling probe depths listed in the table are those required for critical coupling except where otherwise noted. These coupling probe depths are all small - indicating that the excitation probe only slightly perturbed the cavity modes when critically coupling the empty cavity.

Q_L of any mode was measured by sweeping the empty cavity, as shown in Figure 3.6, and displaying the resonance curve on an oscilloscope. This was accomplished when critically coupling the cavity so that $Q_{uo} = 2Q_L$. The accuracy in measuring Q_{uo} was estimated at $\pm$ 10% of the measured value. Several factors affected the experimental values of Q_{uo}. Although the brass collars aided in maintaining the proper mode field patterns, they significantly lowered Q_{uo} in most modes. For example, Q_{uo} in the TM_{012} mode at 2.459 GHz dropped from 12,100 to 6000 because of the collars. Q_{uo} in the TE_{011} mode, however, was relatively unchanged. The absence of the radiation screening and the cleanliness of the cavity also affected Q_{uo}. Without screening, Q_{uo} in the TM_{012} mode dropped by over 1/2 indicating that unshielded large open holes can cause radiated power losses which could present a significant safety hazard. With the screen on, Q_{uo} in the TM_{012} mode ranged from 8,000 to 12,100 depending on cleanliness of the cavity. The highest value of Q_{uo} achieved in the TM_{012} mode at 2.459 GHz was 12,100 which compared reasonably well with the theoretical limit of 15,500 in this mode at the same frequency [20].

Actual experimentation with a plasma was done only in the TM_{012} mode for reasons explained in Chapter V, although a plasma could be sustained in any cavity mode and in a variety of other modes not present in an empty cavity [24]. The theoretical empty cavity field patterns

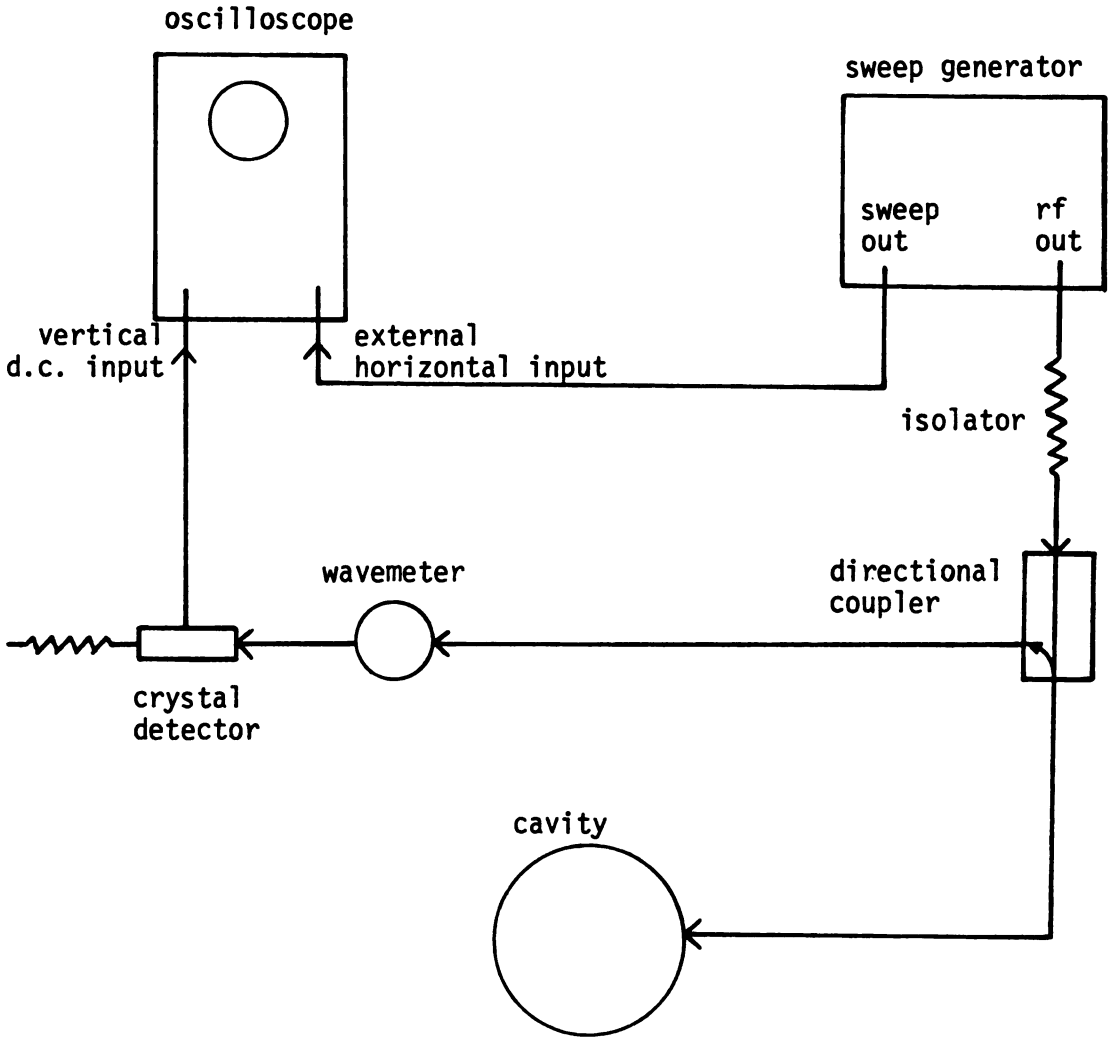

Figure 3.6 Circuit used for the measurement of loaded Q, Q_L, of the empty cavity.

for the TM_{012} mode are described in Appendix C for reference. Typical resonance curves in this mode for the empty experimental cavity are shown in Figure 3.7. L_s was fixed at 14.48 cm for these curves and the horizontal axis was calibrated in terms of frequency. The resonance curves illustrate that coupling to this mode was very sensitive to probe depth. When L_p was increased to greater than 1.0 cm, the resonance curve became so broad that it was difficult to find precisely. It can also be seen from Figure 3.7 that L_p affected the resonant frequency. Thus, when operating at a specific frequency, L_p affected the eigenlength of the cavity.

3.3.3 Basic Cavity Operation for Generating and Maintaining a Discharge

The discharges were ignited in the experimental cavity at any gas pressure with the following procedure. A moderate amount of power (10 - 20 watts) was coupled into the empty cavity in the TM_{012} mode by adjusting L_s and L_p to the correct positions for critically coupling the cavity. The positions were not precisely the same as those listed in Table 3.1 due to the presence of the quartz tube. Breakdown of the gas was subsequently easily achieved by using a Tesla coil to inject a few electrons into the discharge zone. The discharges could be started most easily in the pressure range of 1 - 10 torr. Breakdown of the gas could also be accomplished without the use of the Tesla coil if sufficient power was coupled into the cavity. This technique was avoided, however, because of the increased risk of arcing elsewhere in the cavity (such as around the brass collars) due to the high field strengths required for breakdown.

After breakdown was achieved, the cavity was mismatched due to the

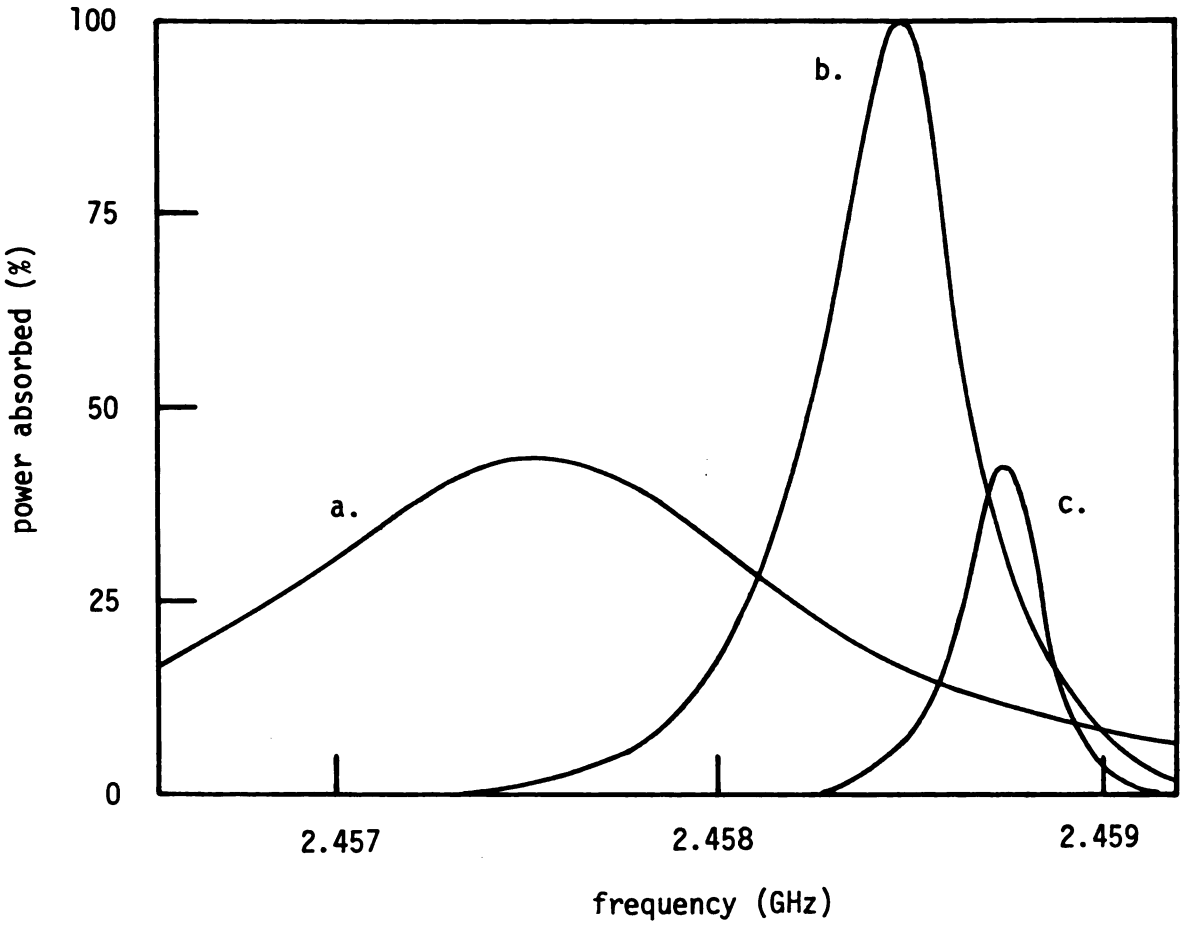

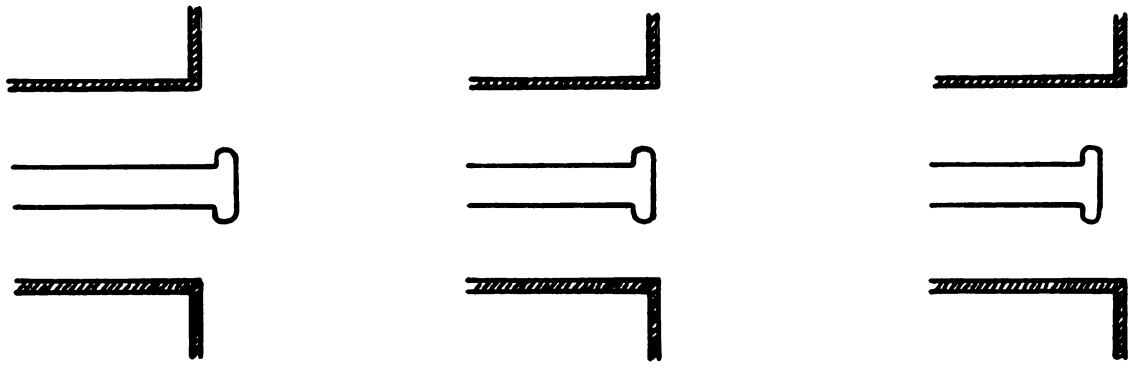

a. overcoupled
L_p = .45 cm
Q_L = 1637

b. critically coupled
L_p = -.09 cm
Q_L = 6550

c. undercoupled
L_p = -.55 cm
Q_L = 10,600

Figure 3.7 Typical resonance curves of the TM_{012} mode showing the effects of changing L_p on Q_L and the resonant frequency. (screening attached to cavity, no collars, empty cavity, L_s = 14.48 cm)

presence of the plasma. This mismatch was the result of: (1) the plasma losses tending to undercouple the cavity (requiring an adjustment of L_p) and (2) the dielectric nature of the plasma causing the eigenlength of the cavity to shift away from L_s. To return the cavity to resonance (i.e., to critically couple the cavity), both L_p and L_s had to be adjusted. In practice, these adjustments were not independent because of the dynamical nature of coupling to the discharges. As one parameter was adjusted, the plasma volume or properties changed due to increased power absorption requiring further adjustments of the other parameter.

The basic tuning process was accomplished by observing the reflected power meter in the rectangular waveguide system. Assuming that the pressure and incident power level were set at the desired values, L_s and L_p were varied to produce a minimum of reflected power. For a high pressure argon discharge of length 8 cm in the center of the cavity, this minimum could always be made zero (i.e., the cavity could always be critically coupled for this plasma geometry). When the lengths of the discharges extended across the entire length of the cavity (as was desired for the analysis), critical coupling was often not achieved. In these instances, however, the reflected powers were all small - typically 5% or less of the incident power which is nearly critically coupled.

When a plasma is sustained by a resonant circuit, a discharge/circuit instability can occur under high Q (i.e. low plasma loss) operation when critically coupling the cavity [10]. This instability was not encountered when coupling to the high pressure argon discharges due to the large losses in the plasma, lowering Q_u to less than 100. The circuit instability was encountered in lower pressure experiments (less than 1.0 torr) and is described briefly in Appendix B.

3.4 Plasma and Cavity Diagnostic Measurements

3.4.1 Identification of Experimental Measurements

Once a desired geometry or length of plasma was generated and the cavity properly tuned, four measurements were taken: (1) total power absorbed into the cavity (P_t), (2) resonant cavity length shift (ΔL), (3) calibrated radial E-field at a reference point at the cylindrical cavity wall (E_{rw}), and (4) average discharge diameter (d_{ave}). These measurements and definitions associated with them are described in this section. How these measurements are utilized in the analysis to determine discharge properties is described in Chapter V.

3.4.2 Total Power Absorbed by the Cavity (P_t)

Various powers in the microwave circuit can be defined as follows:

P_i - incident power at the terminal plane of the cavity

P_r - reflected power at the terminal plane of the cavity

P_t - total power absorbed by the cavity which includes both plasma losses and cavity wall losses

P_p - power absorbed by the plasma

P_c - power absorbed by the cavity walls

Obviously, $P_t = P_i - P_r$. The determination of P_i and P_r involved correcting the actual power meter readings in the waveguide section for the attenuation in the flexible coax and calibration factors on the directional couplers and attenuators. The waveguide system itself was assumed lossless.

3.4.3 Determination of Resonant Cavity Length Shift (ΔL)

Assuming that the cavity (with plasma and quartz tube present) was

properly tuned for resonance in the TM_{012} mode (or as near to resonance as possible), then L_s became the experimental eigenlength of the cavity. Defining L_{so} as the empty cavity experimental eigenlength in the TM_{012} mode, ΔL was determined by:

$$\Delta L = L_s - L_{so}$$

Length shifts were determined on the tuning mechanism exterior to the coupling structure and were measured with a vernier caliper. Typical shifts were on the order of 3-4 mm and accuracy was estimated at $\pm$ .1 mm. The measurement of ΔL was complicated by the fact that cavity configuration changes, coupling probe depths and frequency drifts of the source all affected the experimental empty cavity eigenlength. These effects were all accounted for in the determination of ΔL.

3.4.4 Determination of E_{rw}

Small electrical probes, constructed from 2 mm o.d. microcoax, were inserted into the diagnostic holes of the cavity to probe the $|E_r|$ and $|H_\phi|$ distributions of the TM_{012} mode. Figures 3.8 and 3.9 describe these probes and their location in the cavity. The straight probe (E-field probe), was inserted into one of the seven diagnostic holes on the top of the cavity. This probe coupled out a small fraction of power assumed proportional to $|E_r|^2$ which was measured with a power meter. A typical axial distribution of the measurements of the straight probe is compared in Figure 3.10 to the theoretical distribution of $|E_r|^2$. The shielded loop was sensitive to $|H_\phi|^2$ and confirmed a similar axial distribution as to that in Figure 3.10 but with maximums and

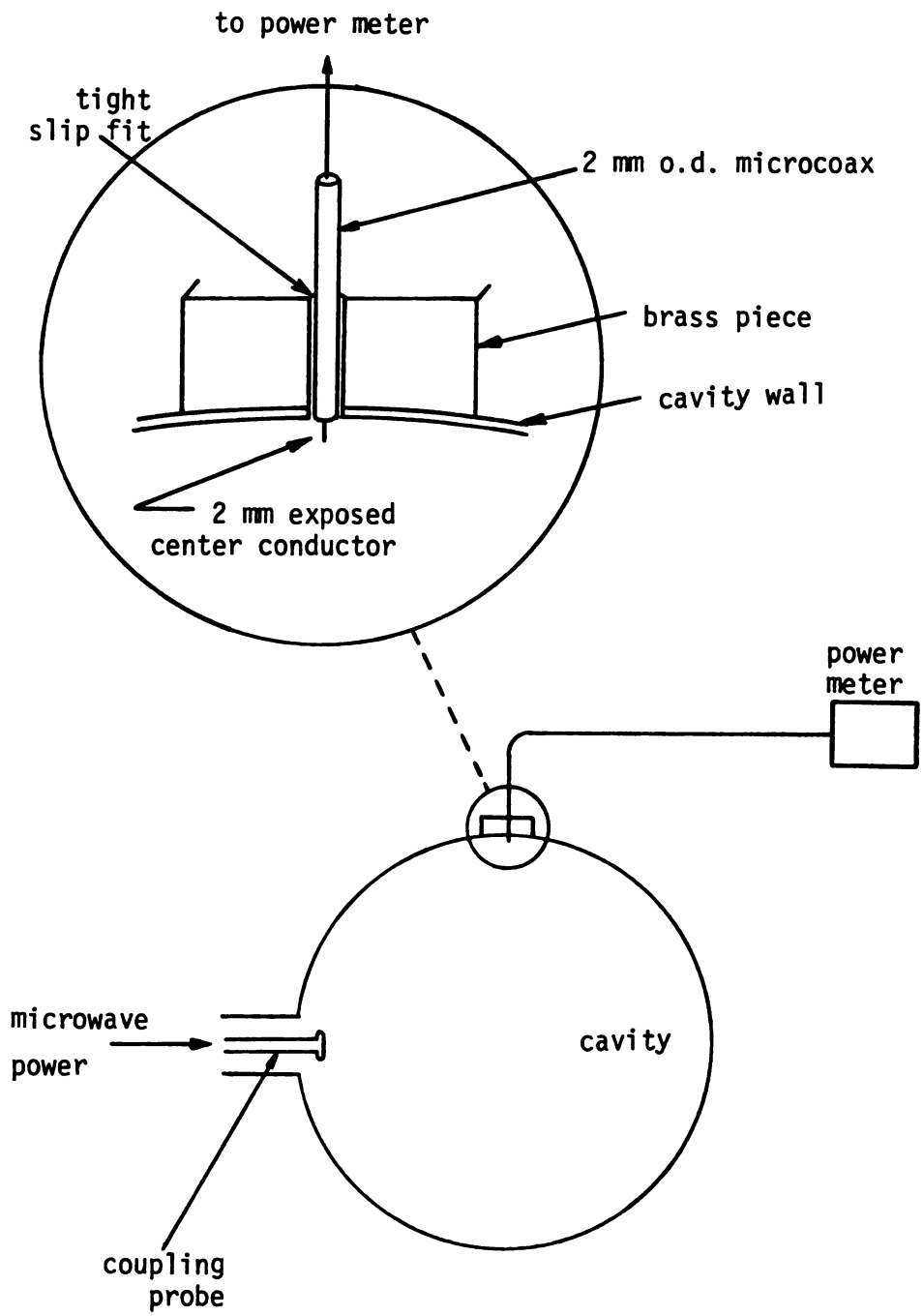

Figure 3.8 E-field probe and probe circuit

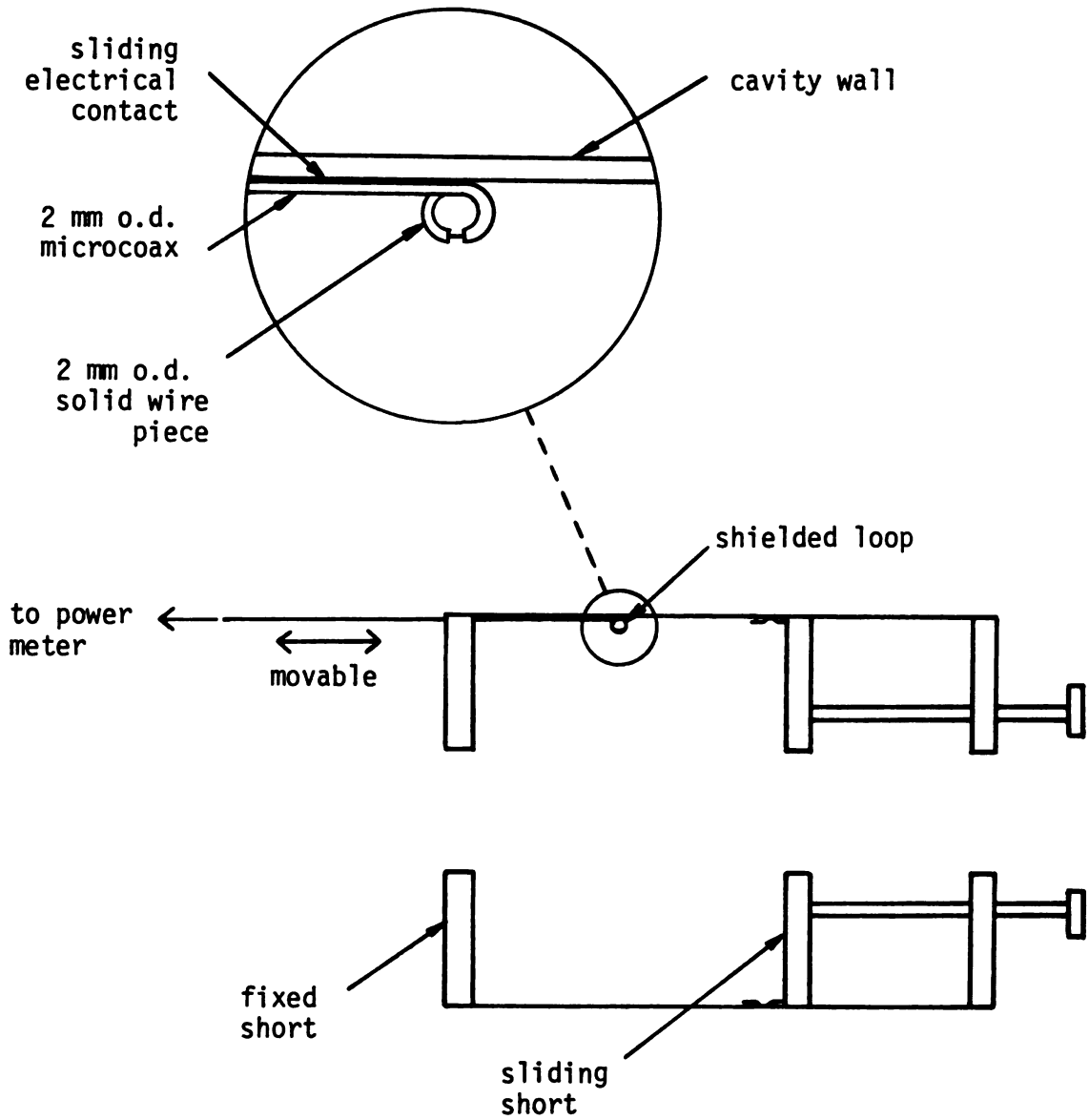

Figure 3.9 Location and description of shielded loop.

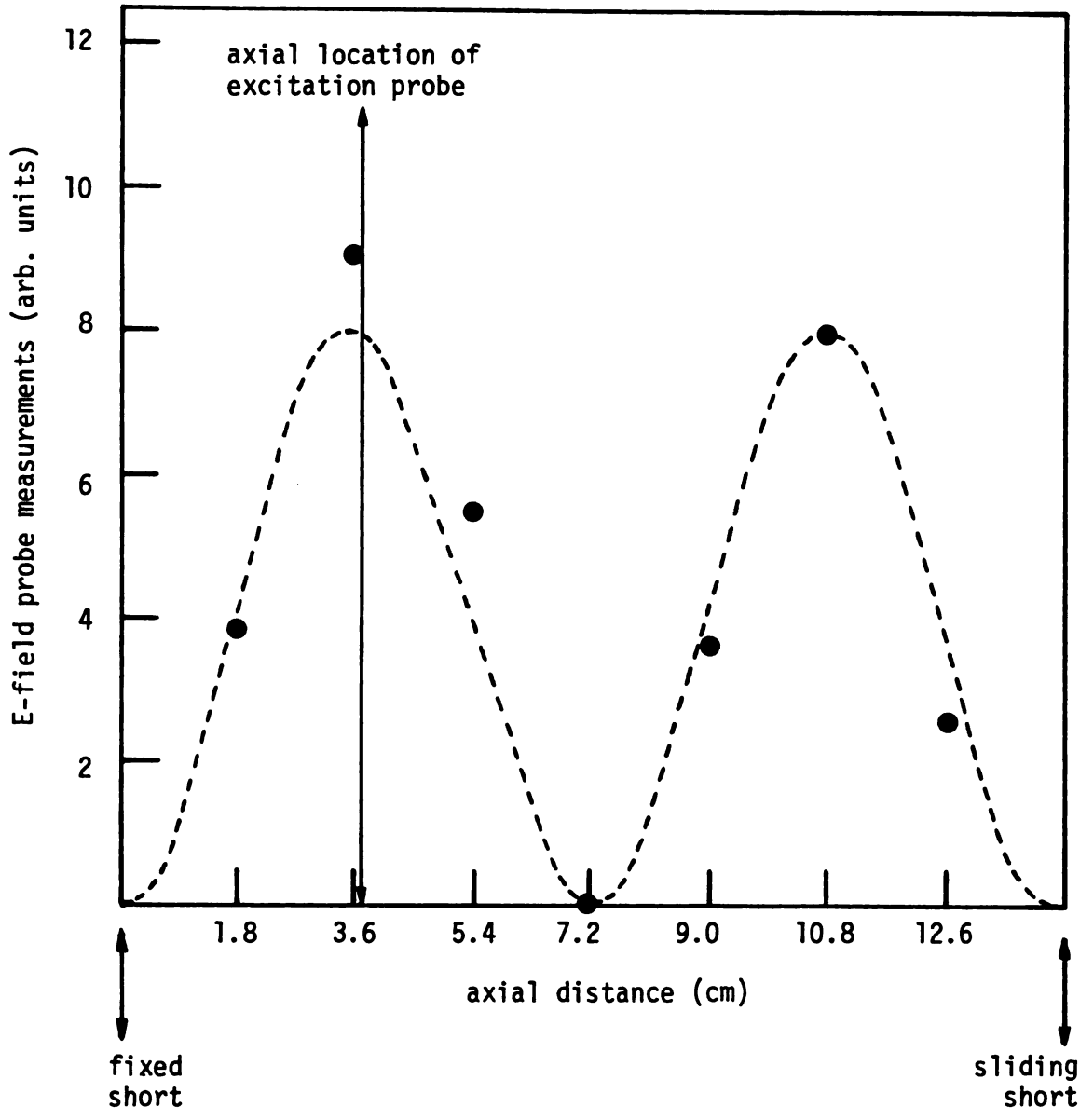

Figure 3.10 Axial distribution of the measurements of the E-field probe in the TM_{012} mode. The solid circles are measurements and the dashed line represents a theoretical axial distribution of $|E_r|^2$.

minimums reversed as expected from theory. Because the loop tended to disrupt the field pattern when it was physically moved (and hence disrupted the discharges) it was removed from the cavity prior to taking actual data. The E-field probe could be inserted or removed during actual experiments with no detectable perturbation to the plasma or cavity fields.

The E-field probe was calibrated to measure absolute field strengths using the following steps: (1) a measured level of power at 2.459 GHz was introduced into the cavity in the TM_{012} mode when critically coupled; (2) using the experimental cavity Q_{uo} and the theoretical field patterns, the absolute field strength was determined at the location of all the diagnostic holes due to this reference power; (3) the straight probe was inserted into the diagnostic holes and the relative field strengths were measured on a separate power meter; and (4) assuming that the straight probe was only sensitive to $|E_r|^2$, the calculated field intensities were used to calibrate the power meter readings in each diagnostic hole.

Because of the sensitivity of Q_{uo} to cavity cleanliness and configuration changes, the experimental Q_{uo} was measured just prior to a probe calibration. Also, the basic components of the probe circuit (connectors, thermister, power meter, etc.) were not changed following a probe calibration. To simplify the use of the field measurement in the analysis, an average value of $|E_r|$ for the axial standing wave was defined. Since holes 1, 3, 5 and 7 were drilled at the theoretical half power points in the TM_{012} mode standing wave (at 2.45 GHz) and because the values of ΔL were small, E_{rw}^2 was defined as the average value of $|E_r|^2$ measured in each of those four holes. Defined in this way, the cavity reference

point for E_{rw} was then always at a half power point of the standing wave.

3.4.5 Average Discharge Diameter (d_{ave})

In general, high pressure argon discharges contract into thin filamentary discharges with diameters smaller than the quartz tube diameter. In the experiments, discharge diameters were measured by taking close-up photographs through the screen window of the cavity. The field of vision of the camera included only the left half of the cavity (as viewed in Figure 3.3). Diameters for the other half were assumed to be the same due to the axial symmetry of both the TM_{012} mode and the visual appearance of the discharges about the midplane of the cavity. This symmetry will be described in more detail in the next chapter. The photographic technique was tested on small rods of known diameter and was accurate to within .05 mm. The photographs were taken with ASA 200 speed film and with a shutter speed of 1/8 second (the discharges were motionless). Exposures ranged from f5.6 to f11 for good quality pictures as the pressure was increased from 40 torr to 1300 torr.

Although the discharge boundaries were quite visually distinct, they were not as sharply defined as the metal rods used to test the accuracy of the technique. The filament cross section consisted of a visually bright central core of 1-2 mm in diameter surrounded by a very diffuse glow which diminished with increasing pressure. (Figure 4.2 of the next chapter shows a typical photograph of the discharge). The plasma diameter at any axial point was defined to include only the bright central core. Axial variations in the diameter were averaged

by sectioning off the discharge into 1 cm sections and neglecting the last .5 cm of the tapered ends of the filaments. The means by which d_{ave} was determined implies that there probably exists an additional small subjective error in this measurement, but would be a consistent one throughout all of the data.

CHAPTER IV

GENERAL EXPERIMENTAL OBSERVATIONS

4.1 Introduction

This chapter contains general observations about the formation of the high pressure argon microwave discharges in the TM_{012} mode. Also included are experimental measurements of discharge diameter and average absorbed power density. The main experimental variables were pressure (40-1300 torr) and the "discharge/tube geometry" (i.e. the approximate cross sectional position of the discharge inside the quartz tube). These geometries will be described in more detail later in this chapter. Changes in the formation of the discharges with large changes in absorbed power are described qualitatively. Some quantitative results on discharge properties were also made with small variations in absorbed power. Gas flow rate was not a variable since all experiments were accomplished on non-flowing discharges. An important experimental note associated with the different discharge/tube geometries is that the quartz tubes were always maintained at near room temperature by external air cooling (using the inlet port shown in Figure 3.3).

For purposes of definition, the average absorbed power density was defined as P_p/V where P_p was absorbed power in the discharge and V was the discharge volume (measured by carefully sectioning off the discharges in the photographs). The analysis in Chapter V explains how P_p was determined from the total power absorbed (P_t). Practically speaking, however, the

results in this chapter can be interpreted as if $P_p = P_t$ since losses in the coupling structure amounted to no more than 1% of P_t for these high pressure experiments (results given in Chapter VI).

4.2 General Formation of Contracted Discharges in a Microwave Cavity

In general, the orientation of a filamentary microwave discharge depends upon the strength and orientation of the mode electric field in the vicinity of the containment tube (if present in the cavity) [5,9]. Figure 4.1 illustrates some typical contracted discharge geometries in different cylindrical cavity modes. Figure 4.1a was observed in the argon experiments described in this dissertation and is also similar to the geometry observed by Kapitza in hydrogen gas (using a TM_{01n} mode) [9]. Figures 4.1b and 4.1c were observed previously by Asmussen in argon gas [25]. As can be seen in the figure, the orientation of the filaments appears to follow the mode E-field lines, as if the longitudinal conduction currents in the discharge (longitudinal with respect to the discharge) replace the displacement currents of the empty cavity mode. The orientation of the H-field appears to generally be tangential and circumferential to the filaments.

In reality, the presence of the plasma alters the EM fields from those of the empty cavity in a complex manner depending on the plasma/cavity geometry. However, the three cases shown in Figure 4.1 all had in common a very small discharge volume compared to the cavity volume. This fact and the close correlation between the discharge orientation to the empty cavity mode fields imply that when a filamentary discharge forms in a large microwave cavity the mode field distributions throughout the cavity are probably not greatly perturbed from the empty cavity

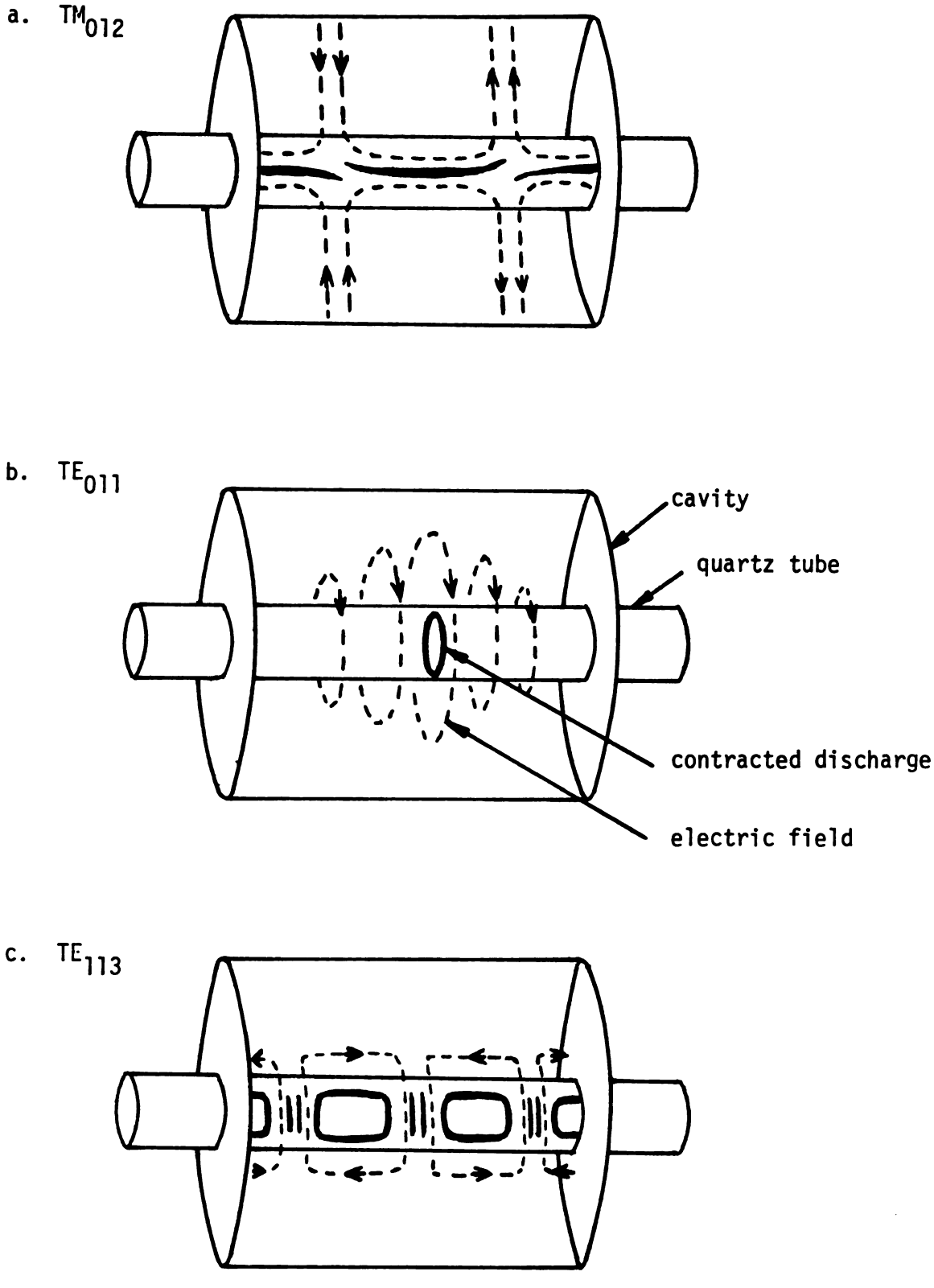

Figure 4.1 Orientation of contracted argon microwave discharges in different cylindrical cavity modes.

mode except near the plasma. The description of the TM_{012} mode argon discharges in this dissertation will support this assertion.

4.3 Discharge Characteristics and Appearance in the TM_{012} Mode

As implied in Figure 4.1a, the presence of the quartz tube restricted the formation of the discharges to near the center of the cavity in the TM_{012} mode - where the axial component of electric field (E_z) is the dominant component in the empty cavity field distribution. At all pressures, the axial pattern of the discharges generally formed along the lines of E_z. The axial pattern of filaments in Figure 4.1a was a typical example and was the specific geometry used in all quantitative experiments. Depending on absorbed power and discharge/tube orientation, other patterns of filaments also formed in relation to the standing wave of E_z. Some of these other patterns are described in the next section.

The contraction of the experimental argon discharges began in the pressure range of 10-100 torr depending on quartz tube size. At low pressures ($\leq$ 1.0 torr) in all tubes, the discharges appeared to fill the tube cross sections. As pressure was increased, the discharges gradually began to have diameters visibly smaller than the quartz tube diameter due to the formation of a bright central core of plasma surrounded by a diffuse plasma. Initially, there was no distinct boundary between these regions but as pressure was increased a distinct boundary gradually appeared. This process began first in the largest tube size (25 mm i.d.) at about 10 torr and began last in the smallest tube size (1.5 mm i.d.) at about 80 torr. As pressure was increased further, discharge diameters continued to gradually become smaller and the appearance of the discharges more intense. The diffuse glow surrounding the

filaments generally diminished with increasing pressure.

Figure 4.2 shows the appearance of a typical argon discharge at 267 torr generated in the geometry of Figure 4.1a. In the photograph, only half of the cavity was visible through the screen window with the midplane of the cavity at the top of the picture. The cavity and the quartz tube (12 mm i.d.) were oriented vertically and the discharge was generally centered in the tube cross section. The tapered ends of the filaments curled off axis toward the quartz wall (appearing to follow the E-field as in Figure 4.1a). Although the emission intensity of the discharges was not high enough to hurt the eyes, plexiglass filters were used when viewing the discharges for long periods of time as a safety precaution. At gas pressures lower than 267 torr, the color of the discharges was more red and the emission intensity less. At higher pressures, the color was more white and the emission intensity higher.

The axial variation of discharge diameter was observed to be related to the strength of the standing wave of E_z. Considering only the central portion of the experimental cavity, the cross sectional area of the discharge appeared to be proportional to the theoretical strength of E_z at any axial point. This relationship is plotted in Figure 4.3 for the discharge shown in Figure 4.2. This same relationship between cross sectional area and the axial distribution of E_z was found in the standing surface wave experiments in argon gas (Appendix A).

As can also be inferred from Figure 4.3, the open holes on the two shorts caused a decrease in the actual strength of E_z relative to the strength in the central portion of the cavity. The fringing fields in the open holes caused the discharges to extend past the inside wall of either short approximately 1 cm. However, the total discharge volume

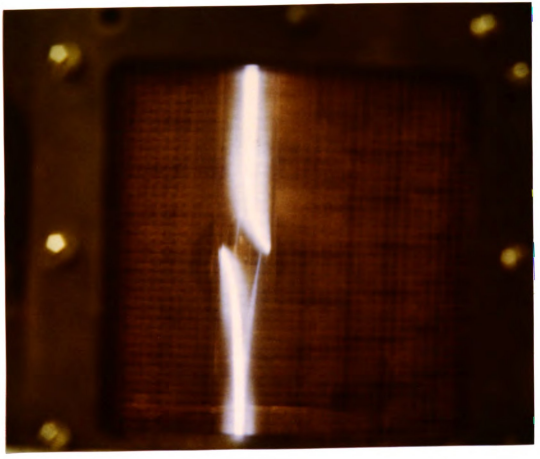

Figure 4.2 Contracted argon microwave discharges in the TM_{012} cavity mode at 267 torr.

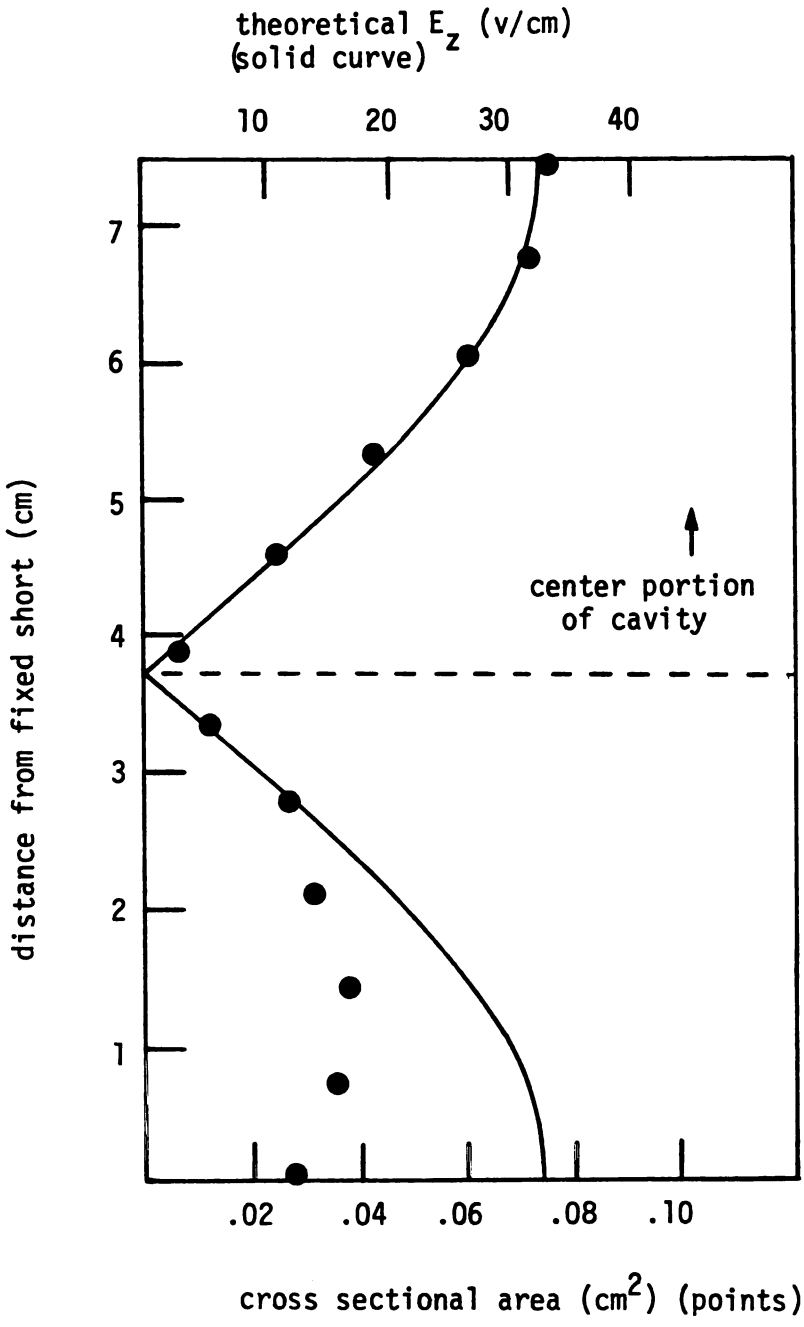

Figure 4.3 Cross sectional area of filament compared to theoretical axial $|E_z|$ for the discharge in Figure 4.2.

of the section of plasma near either short remained approximately 1/2 of the discharge volume of the central filament (true only when the axial pattern of the discharges was similar to Figure 4.1a).

The diffuse plasma surrounding the filament appeared to be related to the presence of E_r, which is at a maximum at the axial position of minimum E_z. This can be seen in Figure 4.2 near the ends of the filaments (in the center of the photograph) and in the region of the open hole (where the fringing fields produced an E_r not present in an ideal cavity). Observations on the same correlation between diffuse plasma around the filament and the presence of E_r were also made on the standing surface wave filaments described in Appendix A.

4.4 Effect of Adding Power at a Constant Pressure

As power was added to the discharges, discharge volume increased due to three effects: (1) increases in plasma diameter and length; (2) the formation of additional filamentary sections of plasma; and/or (3) increases in length outside the cavity (further than would be expected from the fringing fields in the open holes) or increases in plasma length into the region of a null of E_z. The processes described in (3) are indications of coupling to a surface mode and were in general less important effects than (1) and (2). An important note implicit in the discussion is that when absorbed power by the discharge was increased, this usually meant that incident power to the cavity was increased and the cavity subsequently tuned (by adjusting L_s and L_p as described in Section 3.3).

Figure 4.4 describes the effect of adding power in the 25 mm i.d. tube oriented horizontally at a pressure of 90 torr. At P_p = 8.5 watts

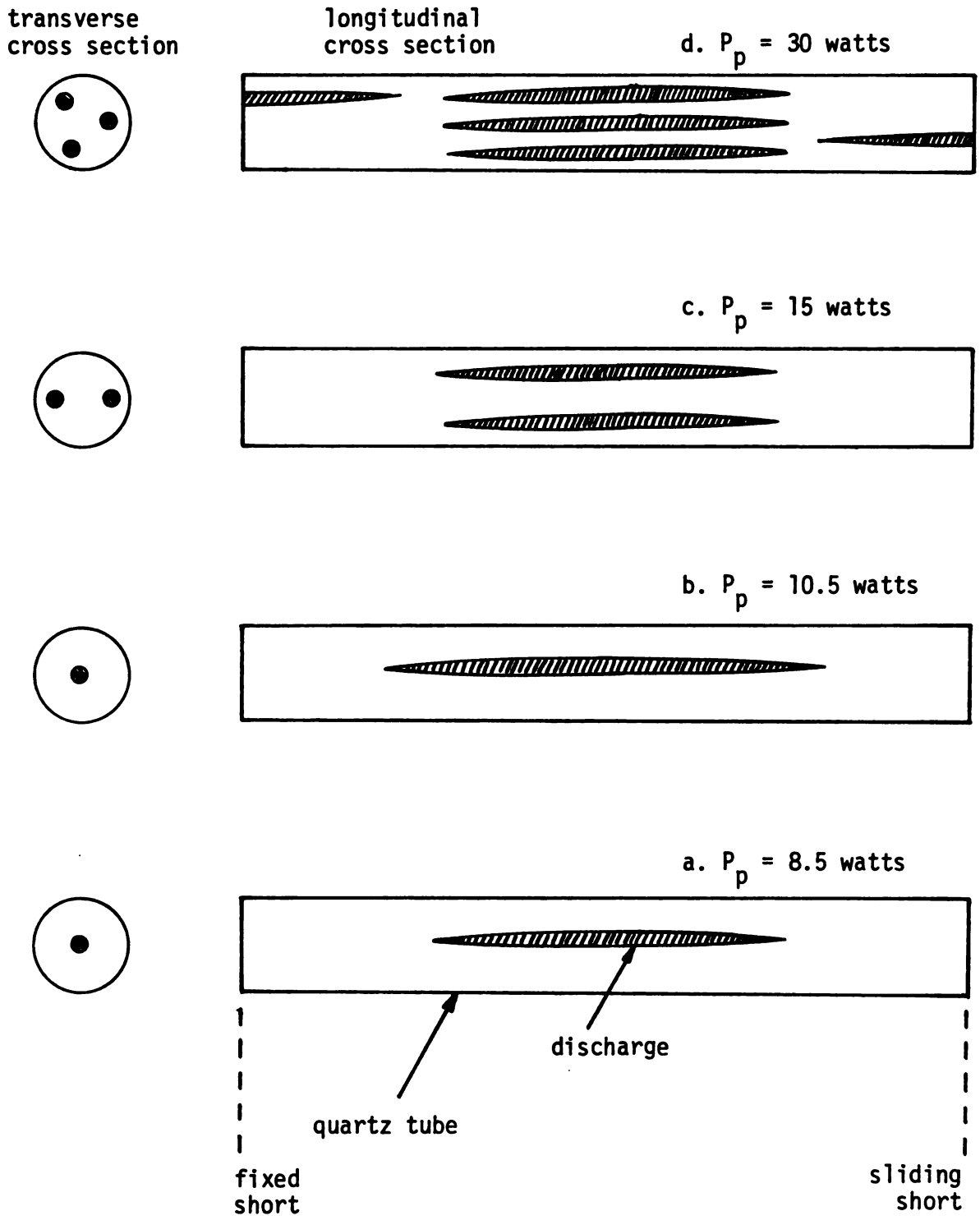

Figure 4.4 Effect of adding power at a constant pressure. The circles to the left of each illustration indicates the cross sectional appearance of the center (axially) of the cavity. (90 torr, 25 mm tube, horizontal orientation).

(Figure 4.4a), a single contracted discharge occupied the central region of the cavity having a length of approximately 7 cm and a diameter of approximately 2 mm. When raising P_p to 10.5 watts (Figure 4.4b), the diameter and length of the discharge increased keeping <P> approximately constant. The extension of the filament in Figure 4.4b into the regions of a null of E_z indicated some coupling to a surface mode. However, this process was limited because further power additions caused the filament to abruptly split into two shorter and thinner filaments as shown in Figure 4.4c. These filaments appeared to repel each other by occupying opposite sides of the tube as indicated in the cross sectional view of 4.4c. The transition between 1 filament and 2 filaments exhibited hysteresis since the reverse process (when decreasing power) consistantly took place at a lower power level than the forward process. When adding more power (Figure 4.4d) more sections of plasma were produced in the manner described above.

Adding power to the discharges at other pressures and in other tube sizes had similar effects. There was, however, little tendency for two or more filaments to form side by side in the smaller tube sizes (4.0 mm and 1.5 mm i.d.). Instead, there was more of a tendency for filament length to extend outside the cavity further than would be expected from the fringing fields (indicating coupling to a surface mode). Above 100 torr, the ability to increase plasma volume in this manner was limited by the ability to match impedance (i.e. as incident power was increased, increases in reflected power could not be avoided by retuning the cavity).

The phenomenon of a single filament splitting into two filaments was usually very abrupt. In one case, however, the splitting appeared gradually and is shown in Figure 4.5. In this particular case, the 12

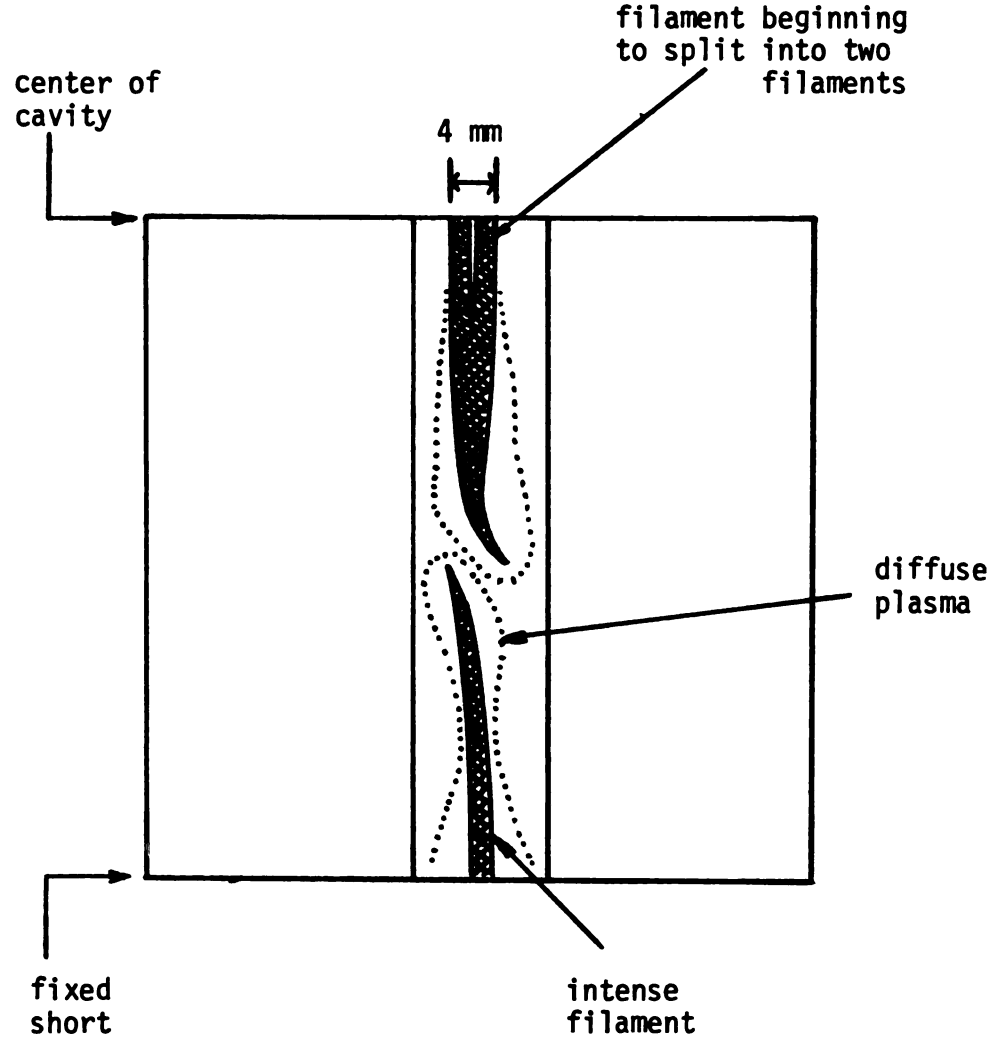

Figure 4.5 Filamentary argon discharge beginning to split into 2 filaments (1 ATM, P_p = 100 watts, 12 mm tube, vertical orientation).

mm tube was oriented vertically and the main portion of the filament was nearly centered in the tube when the splitting began. The spliting occurred near the axial center of the filament (the top of the figure) where the discharge radius was a maximum. Using approximate electron densities from Chapter VI, the skin depth of this discharge (a quantity defined in terms of the penetration of a plane wave into a conductor) was about equal to the maximum radius. Another experimental observation on the splitting phenomenon was that when discharges were oriented horizontally (where there were strong asymmetric bouyant forces) filament splitting occurred more frequently than the vertical orientation and the transitions were always abrupt. The above observations suggest that mechanisms important to the splitting phenomenon are: (1) the relationship between the filament radius and the radial intensity distribution of the microwave E-field across the filament (i.e., the depth of penetration of the E-field), and (2) asymmetric forces due to thermal conduction and/or convection, or asymmetric EM forces.

4.5 Discharge/Tube Geometries and Their General Effects on the Discharges

Most of the experiments were accomplished with the specific geometry of Figure 4.1a (i.e. filamentary discharges extending across the length of the cavity with only a single filament in the tube cross section). Given that geometry, varying the location of the discharge in relation to the quartz tube wall produced noticeable changes in discharge properties. The location was varied in two different ways: (1) by orienting the quartz tube and cavity horizontally or vertically, and/or (2) by changing the size of the quartz tube.

Figure 4.6 describes the two orientations of the experimental cavity

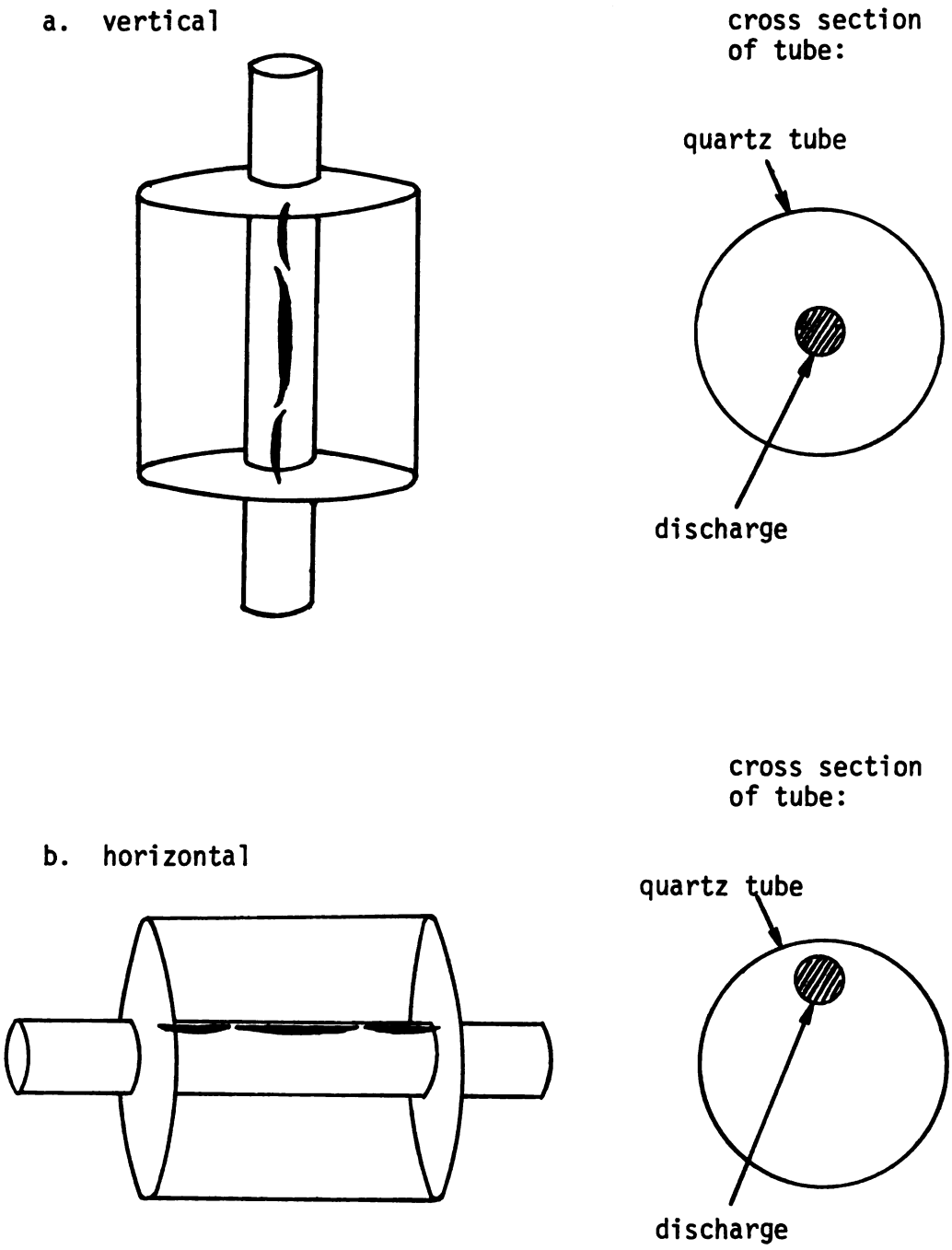

Figure 4.6 General effect of a change in discharge tube orientation. a. Vertical orientation. b. Horizontal orientation.

and the approximate location of the discharges. When in a horizontal orientation, the bouyancy force tended to cause the filaments to float up to the top of the tube. This was most noticeable above 100 torr in the 25 mm and 12 mm tubes but was also observed in the 4 mm tube. Below approximately 100 torr there was little noticeable effect of the bouyancy force. In a vertical orientation, the discharges tended to remain centered except for the ends of the filaments which curled toward the quartz wall. In the 25 mm tube oriented vertically, upward convection currents were visually apparent at pressures above 350 torr by a candle-like "flickering" of the filament at the top. These currents made it difficult to keep the discharges stable (i.e. motionless). Above 1 ATM, the discharges in this tube shifted toward the quartz wall (asymmetric in the tube) and were stablized by the wall.

In the horizontal orientation when discharges floated up next to the quartz wall, two effects were noted: (1) discharge diameters were smaller than those of vertically oriented discharges at the same absorbed power level and in the same tube size, and (2) visual light intensity of the discharges appeared to increase. Figure 4.7 displays the changes in power density, <P>, that occurred between the two orientations for similar length discharges in the 12 mm tube. Above 100 torr, there was a distinct difference in <P>, with those of the horizontal discharges being higher than those of the vertical orientation.

Similarly, changes in tube size with the discharges centered in the tube also produced changes in discharge diameter and power density. Figure 4.8 shows the four different tubes (vertical orientation, lengths of discharges as in Figure 4.1a) and the approximate size and location of the discharges. Figures 4.9 and 4.10 describe the resulting effects

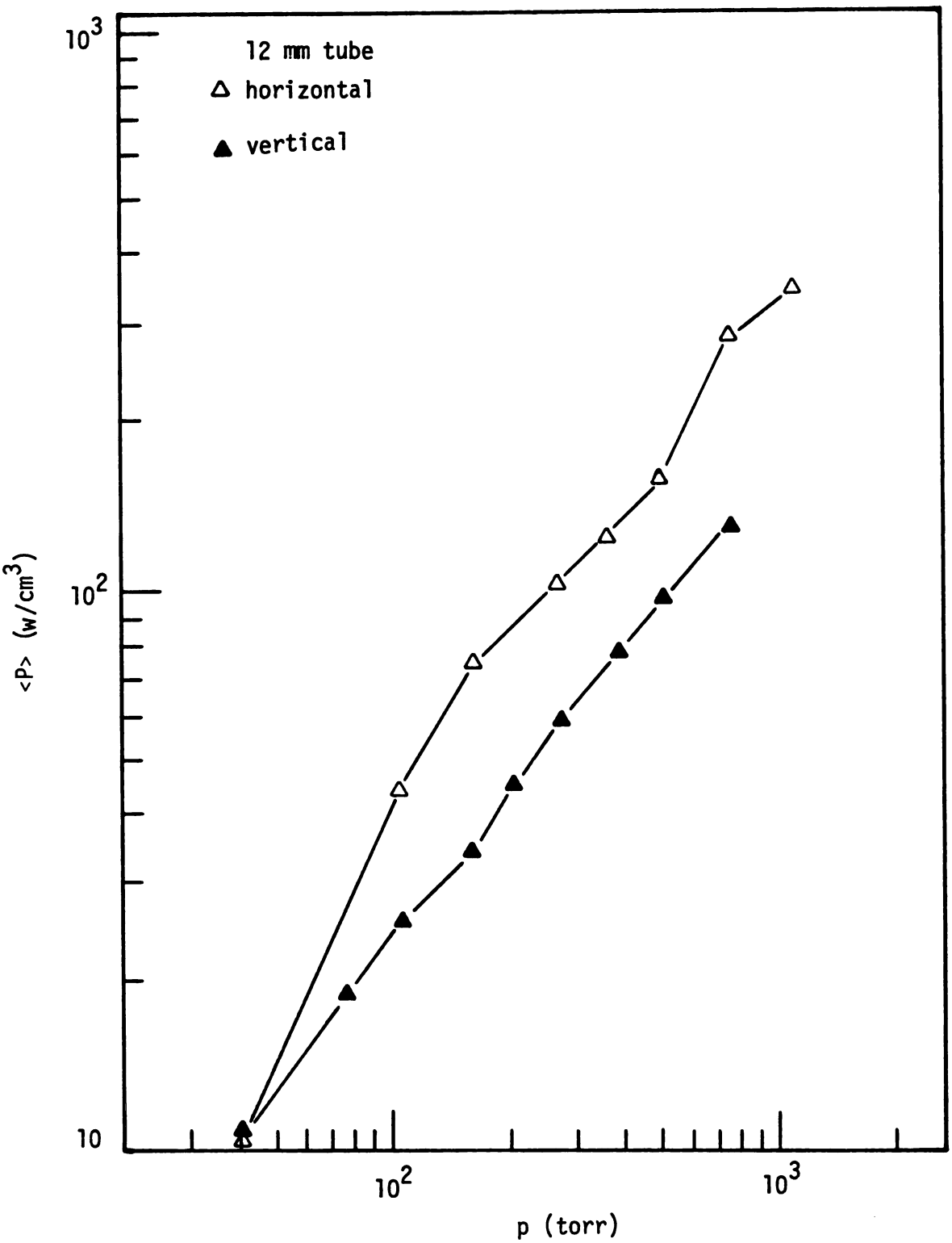

Figure 4.7 Absorbed power density, <P>, for similar length discharges in the different tube orientations.

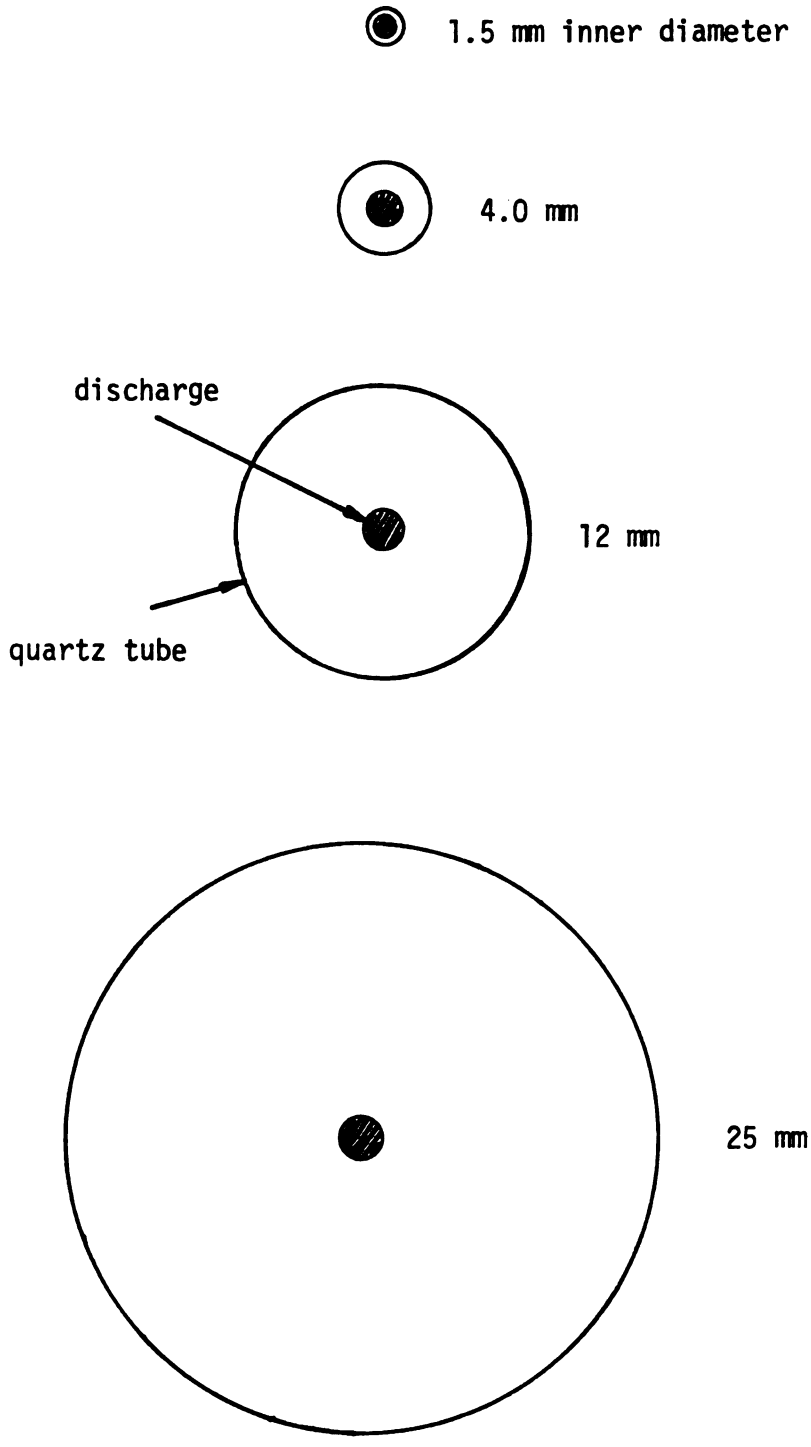

Figure 4.8 Discharge tube cross sections and the approximate size and location of the discharges in the vertical orientation.

on d_{ave} and <P>. In the 25 mm tube, the pattern of Figure 4.1a could only be maintained in a limited pressure range and is thus the reason for the small number of data points in the figures. At any given pressure, P_p was approximately the same in all tubes to produce the common discharge length of Figure 4.1a (approximately 16 cm, which included the ends of the filaments which curled into the region of the open holes). Thus, the differences in <P> resulted primarily from the changes in diameter which occurred in the four different discharge/tube geometries.

Figure 4.11 shows changes in <P> with small changes in P_p for three of the vertically oriented tubes at a pressure of approximately 265 torr. For the 4 mm and 12 mm tubes, increases in P_p caused increases in volume keeping <P> approximately constant. In the 1.5 mm tube, however, <P> increased with P_p since volume increases were restricted.

The changes in other discharge properties for the four discharge tubes oriented vertically are described in detail in Chapter VI. The analysis by which those properties were determined (given in the next chapter) depended upon the approximate rotational symmetry present in the vertical orientation. Thus, discharges in a horizontal orientation were not analyzed beyond the discussion in this chapter.

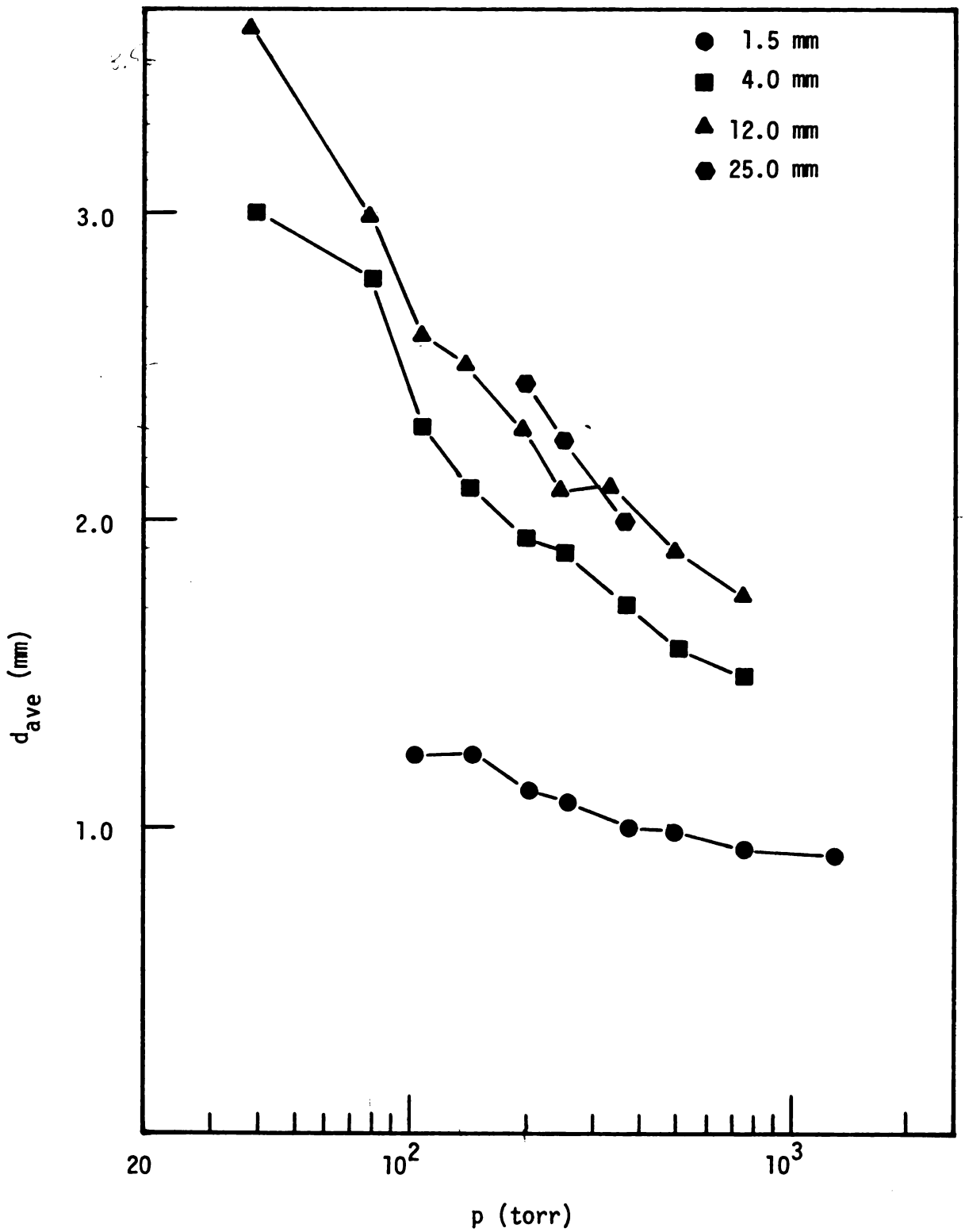

Figure 4.9 Average discharge diameter, d_{ave}, for similar length discharges in the four tubes oriented vertically.

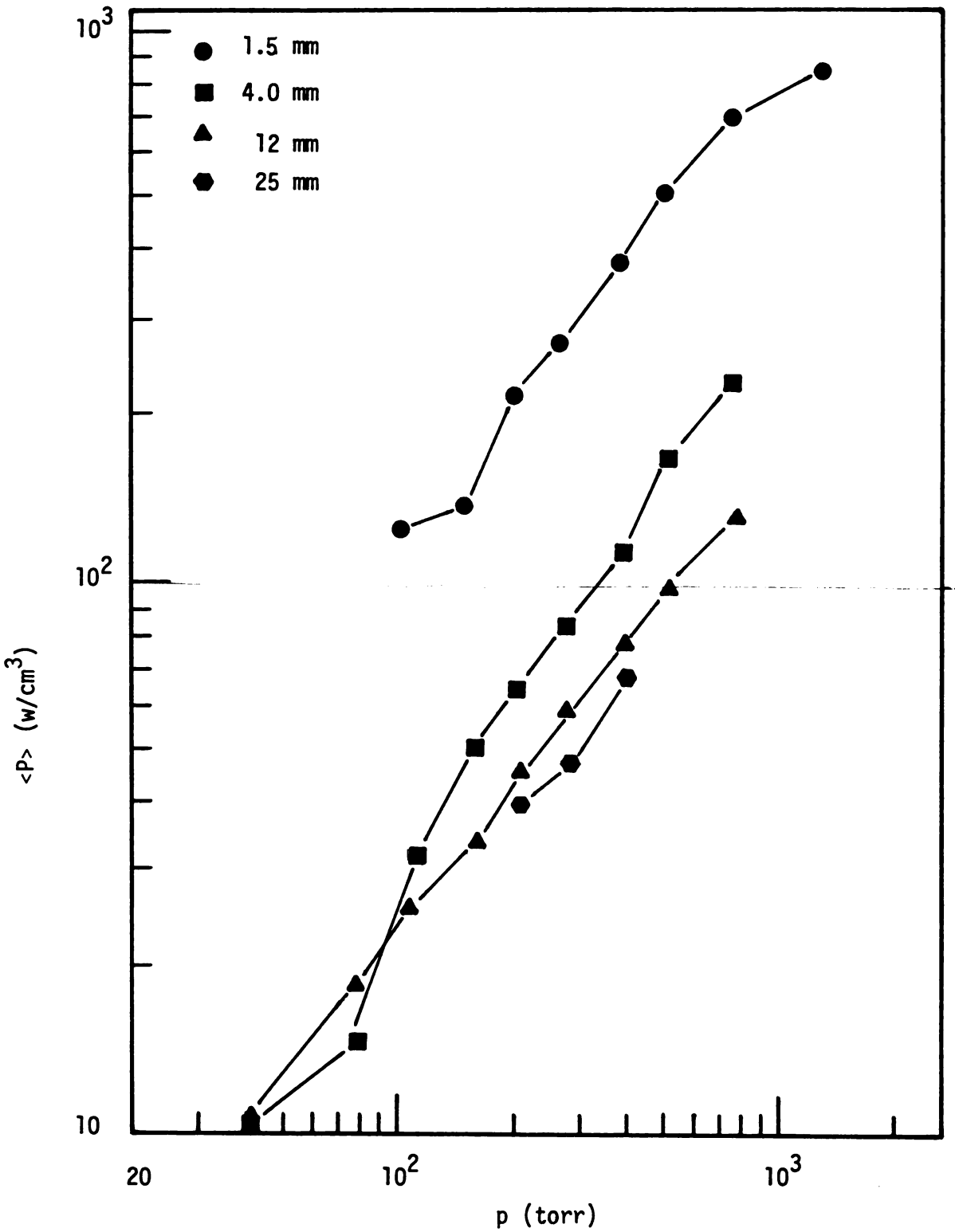

Figure 4.10 Absorbed power density, <P>, for similar length discharges in the four tubes oriented vertically.

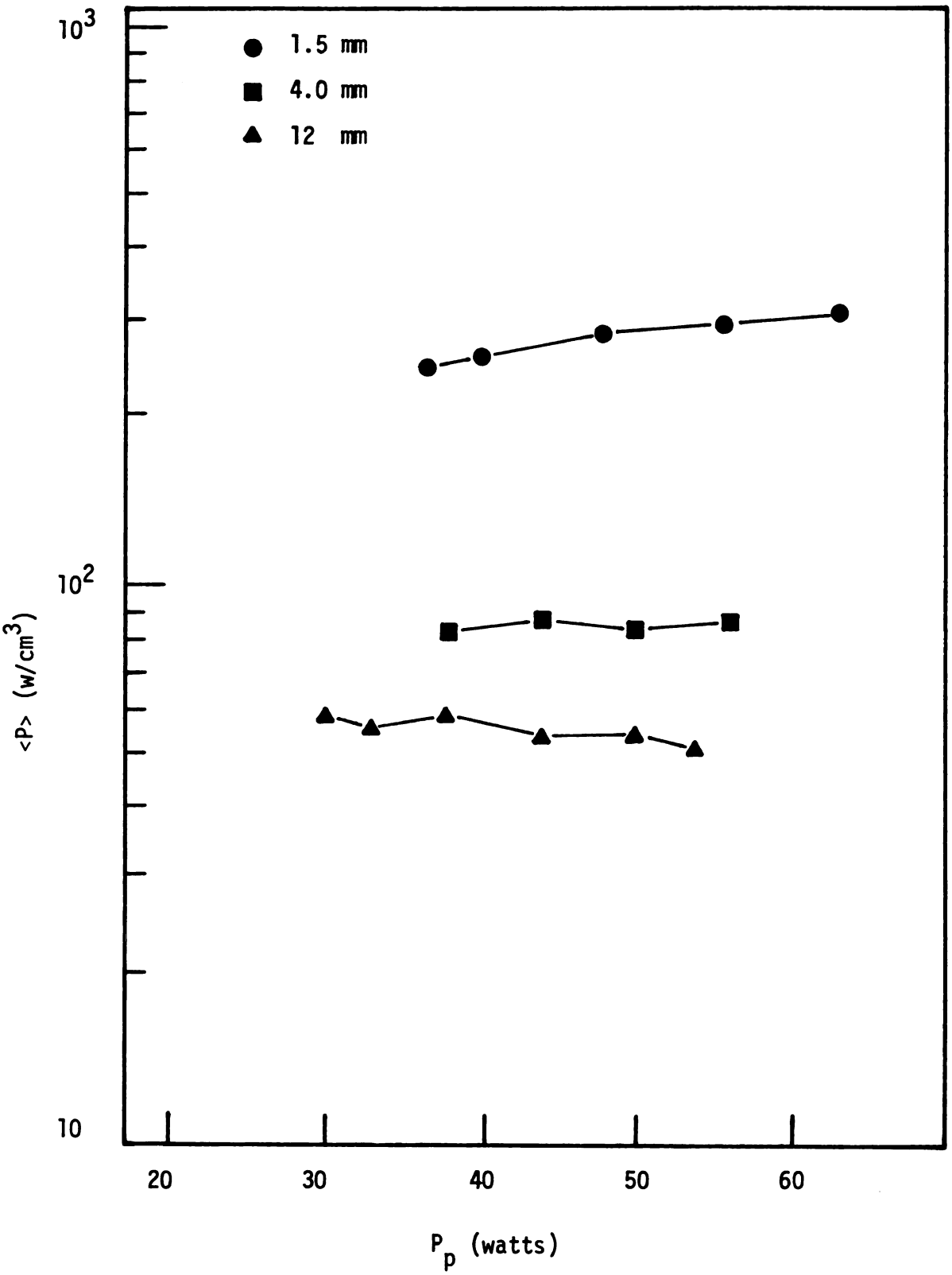

Figure 4.11 Absorbed power density, <P>, versus absorbed power, P_p, at a constant pressure of 265 torr.

CHAPTER V

ANALYSIS OF THE EXPERIMENTAL DISCHARGES

5.1 Overall Analysis Scheme and Reasons for Using the TM_{012} Cavity Mode

To diagnose discharge properties such as electron density and temperature, the experimental measurements were combined with an analysis of a plasma/cavity geometry which approximated the actual experiment. Due to the type of analysis, all discharge properties are average quantities, representing spatial averages of both radial and longitudinal variations in the plasma. Figure 5.1 describes the overall analysis and what information was gained in each step. The general flow of the analysis was from the top of the figure to the bottom, with the four experimental measurements that were defined in Section 3.4 being located at the top. The number in each box refers to the section in this chapter which describes that particular part of the analysis.

The power absorbed in the plasma (P_p), the power lost in the coupling structure (P_c) and the coupling efficiency (Eff) were determined from P_t and E_{rw} using an EM perturbation solution on the TM_{012} mode fields. Average complex conductivity of the discharges (σ) and the electromagnetic fields ($\vec{E}(\vec{r})$ and $\vec{H}(\vec{r})$) were determined by an EM plasma/cavity analysis for a lossy plasma/ideal cavity geometry which approximated the experimental geometry. The required inputs for this determination were P_p, E_{rw}, ΔL, d_{ave}, and the cavity and quartz tube dimensions. Using the cold plasma conductivity model for a weakly ionized gas discharge, average electron density (N_e) and effective

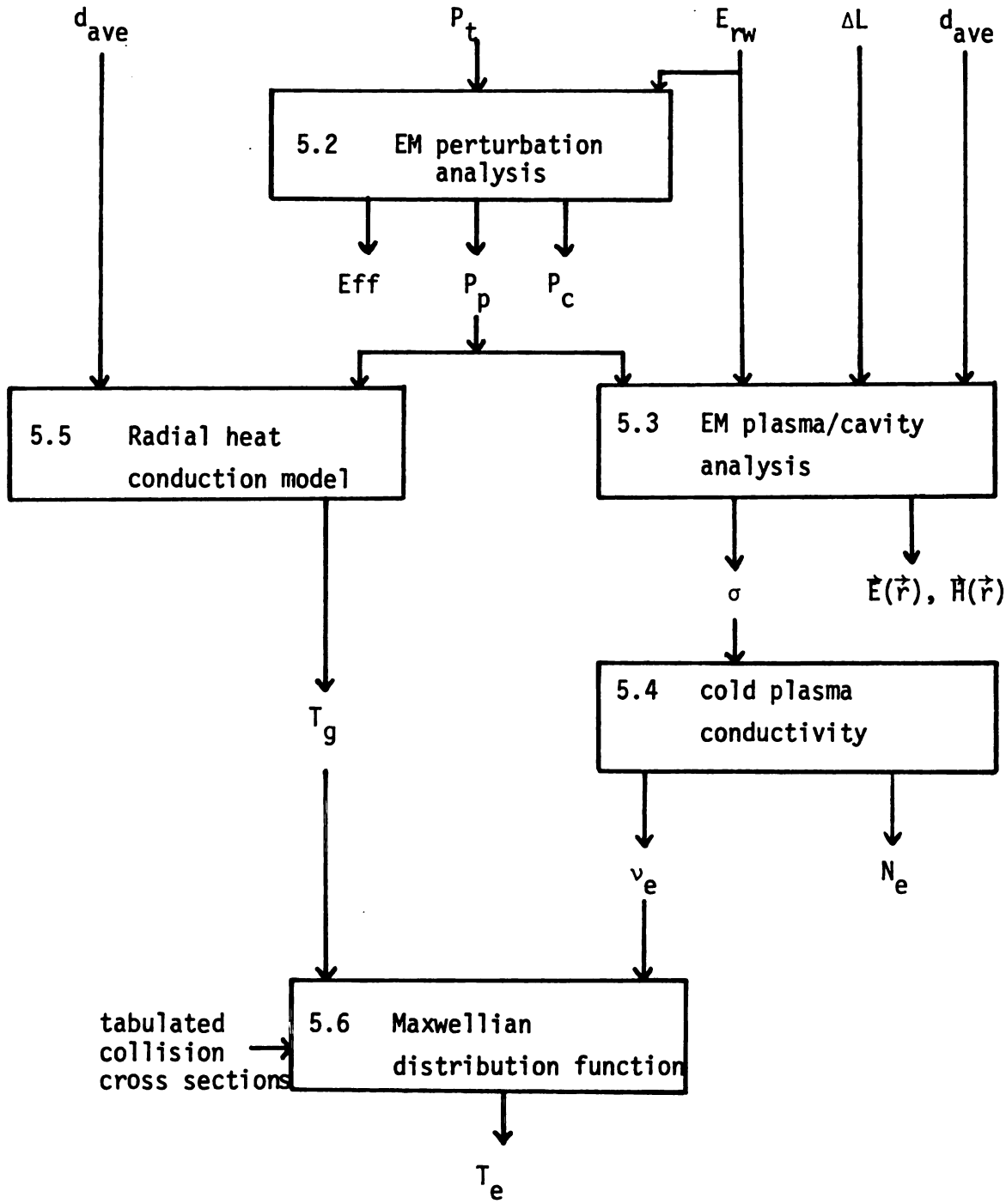

Figure 5.1 Overall diagnostic scheme. Symbols are defined in the text and the number in each box refers to the section in this chapter which describes that part of the analysis.

collision frequency (ν_e) were determined from σ. An approximate average gas temperature of the discharge (T_g) was determined from P_p, d_{ave} and the quartz tube dimensions using a radial heat conduction model. Finally, an average electron temperature (T_e) was determined from ν_e, T_g, and gas pressure using tabulated electron-neutral collision cross sectional data for argon gas and assuming a Maxwellian velocity distribution function for the electrons.

The principal reason for using the TM_{012} mode in the experiments was the relatively simple geometry in which the long, thin filaments could be generated. As can be seen in Figure 4.1a, the discharges were basically coaxial in the cavity. In the vertical orientation (of Figure 4.8),this rotational symmetry was maintained inside each quartz tube. By approximating the non-uniform filaments with a homogeneous, lossy dielectric rod, this approximate plasma/cavity problem can be mathematically described. The other geometries of Figure 4.1 cannot be so easily analyzed. Additionally, the TM_{01n} cavity modes have traditionally been used to diagnose accurate average discharge properties in plasma columns on the axis of the cavity because of the rotational symmetry of the fields and the strong component of E_z on the axis [24,26].

5.2 Coupling Structure Losses and Coupling Efficiency

The power lost in the coupling structure (P_c) was determined with an EM perturbational analysis. The basic assumption was that the presence of the plasma did not greatly alter the spatial distribution of the fields from those of the empty experimental cavity in the TM_{012} mode. Evidence supporting this assumption was: (1) the very small discharge volumes caused only small shifts in the eigenlengths, and (2)

direct measurements of the axial distribution of $|E_r|^2$ at the cavity wall always showed the presence of a similar standing wave with or without the discharge present. Additionally, the numerical solutions for the cross sectional field distributions in the modeled plasma/cavity only deviated from those of the ideal empty cavity near the plasma in the center of the cavity (i.e. the results were consistent with this assumption). Examples of these numerically obtained field distributions are given in Chapter VI.

Under the above assumption, P_c with a plasma present in the cavity was determined by using the field distributions of the empty experimental cavity (the precise distributions of which were unknown and not needed in the determination of P_c). Since coupling structure losses at any point are proportional to the square of the field strength, P_c was determined by a measure of $|E_r|^2$ at a reference point relative to similar measurements on the empty cavity. With E_{rw} and P_t being the measurements described in Section 3.4, P_c was determined by:

$$P_c = \frac{E_{rw}^2}{E_{rwo}^2} P_{to} \tag{5.1}$$

where E_{rwo}^2 and P_{to} were the measurements made on the empty cavity critically coupled in the TM_{012} mode. As can be seen from equation 5.1, E_{rw} did not have to be calibrated for this determination.

In a similar manner, the cavity Q_u (with plasma present) was determined by:

$$Q_u = \frac{Q_{uo} P_{to}}{E_{rwo}^2} \times \frac{E_{rw}^2}{P_t} \tag{5.2}$$

where Q_{uo} was the experimental empty cavity Q_u measured at the same time as E_{rwo} and P_{to} were measured. It should be noted that the resonance curve method of determining Q_u (perhaps with a separate, low power diagnostic circuit in a different cavity mode) was not practical for the experiments. The reasons for this were: (1) the plasmas brought Q_u down to between 50 and 100, at which values the resonance curve would have been completely washed out among the system resonances; and (2) the high power excitation fields inside the cavity would have interfered with the low power diagnostic circuit causing filtering problems.

A coupling efficiency, Eff, to the discharges was defined as:

$$\text{Eff} = 100\% \times \frac{P_p}{P_t} \tag{5.3}$$

where P_p and P_t are defined in Section 3.4 and $P_p = P_t - P_c$. Eff expresses the ratio of power absorbed by the plasma to the total power absorbed by the cavity. For a practical application, this ratio should be high. A further discussion of the efficiency of coupling microwave power to a weakly ionized plasma is given in reference [2].

5.3 Determination of Complex Conductivity and Plasma Electric Field

Discharge conductivity and the EM fields in the cavity were determined for an ideal plasma/cavity geometry which closely approximated the experimental geometry of Figure 4.1a. This approximation is pictorially described in Figure 5.2. For the approximate problem, the non-uniform filaments were replaced by an axially uniform, homogeneous, lossy dielectric rod with diameter equal to d_{ave} of the filaments.

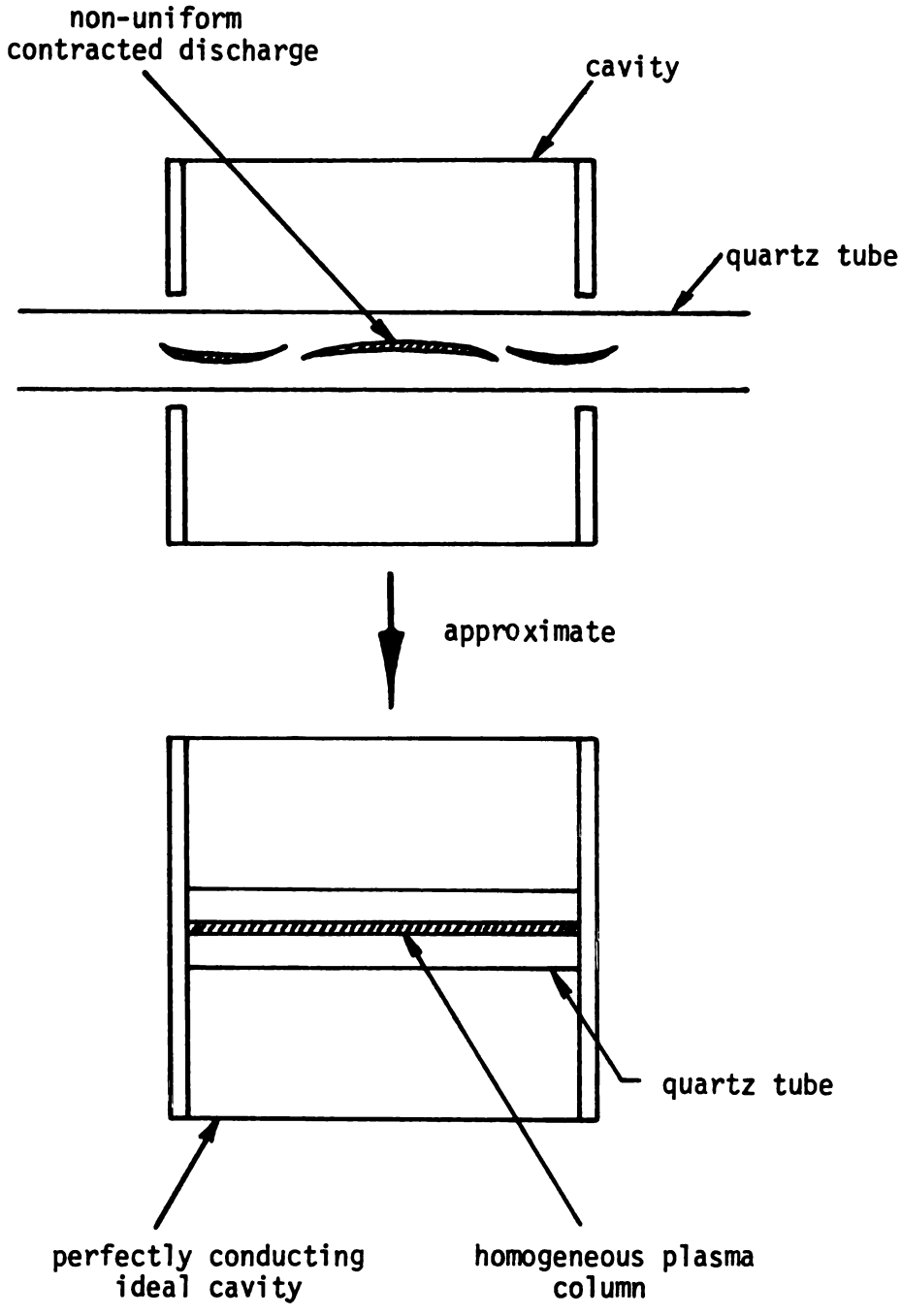

Figure 5.2 Approximation of the experimental plasma/cavity geometry with an idealized plasma/cavity geometry.

Essentially, the axial uniformity of the dielectric rod and cavity (with ideal cavity shorts) allowed the standing wave plasma/cavity problem to be equivalent to an axially uniform plasma/waveguide problem for the purposes of the analysis. The amplitude of the plasma/waveguide problem was determined by the average amplitude of the standing wave in the cavity problem. This type of rotationally symmetric boundary value problem, with an unmagnetized, homogeneous plasma on the waveguide axis, has been analyzed in detail [11,24,27,28] and the method of solution is well established [29].

Figure 5.3 describes the specific cross sectional geometry of the plasma/waveguide problem used in the analysis. Region 2 was included because the discharges were contracted in varying degrees away from the quartz boundary. The quartz was assumed lossless with a relative permittivity of $\varepsilon_r = 3.78$. The outer metal cylinder was considered a perfect conductor.

The solution to this boundary value problem was simplified by a priori looking for the rotationally symmetric TM modes. Maxwell's equations in cylindrical coordinates ($e^{j\omega t}$ implied) for the ith region reduce to:

$$
\begin{aligned}
E_{zi}(r,z) &= \Psi_i(r)\, e^{-j\beta z} \\
E_{ri}(r,z) &= \frac{j\beta}{k_{ci}^2} \frac{d\Psi_i(r)}{dr}\, e^{-j\beta z} \\
H_{\phi i}(r,z) &= \frac{j\omega\varepsilon_i}{k_{ci}^2} \frac{d\Psi_i(r)}{dr}\, e^{-j\beta z}
\end{aligned}
\tag{5.4}
$$

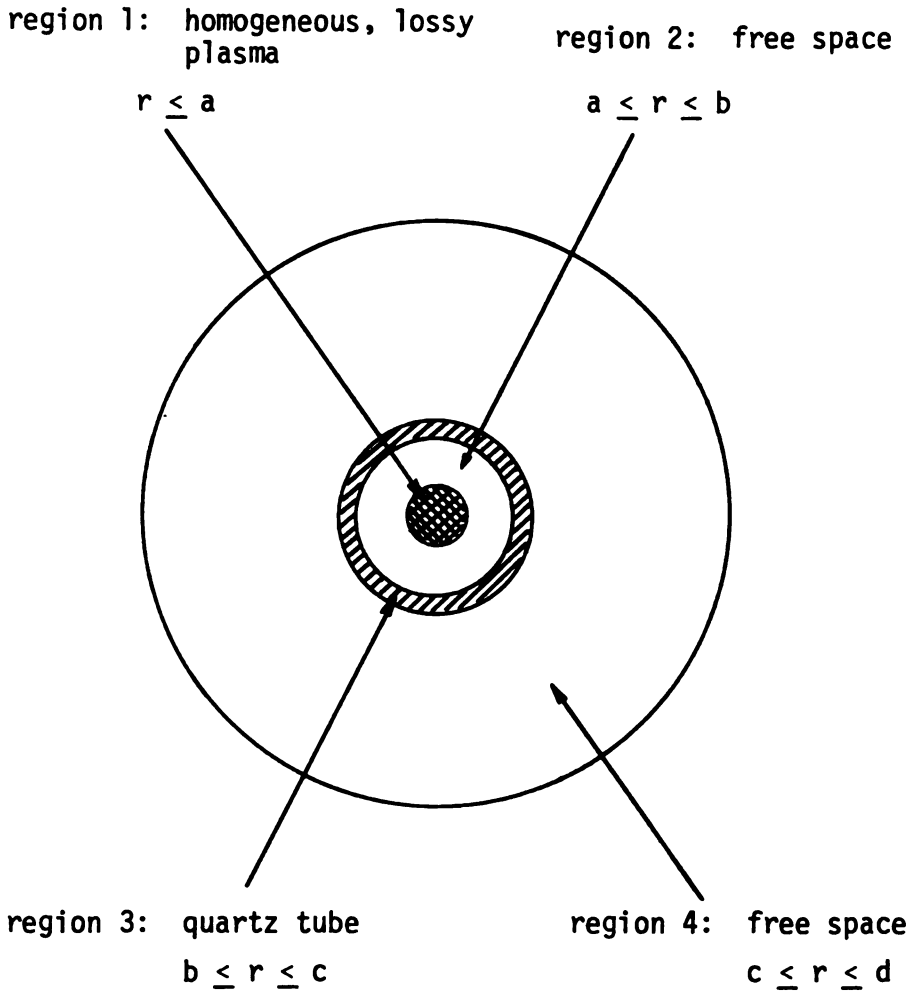

Figure 5.3 Cross sectional geometry of the EM boundary value problem used in the analysis (not to scale).

where r,ϕ,z are the standard cylindrical coordinates and $\Psi_i(r)$ satisfies the modified Bessel equation of order zero:

$$\frac{d^2\Psi_i(r)}{dr^2} + \frac{1}{r}\frac{d\Psi_i(r)}{dr} - k_{ci}^2\,\Psi_i(r) = 0 \qquad (5.5)$$

and where

$$k_{ci}^2 = \beta^2 - k_i^2$$

$$k_i^2 = \omega^2 \mu_o \varepsilon_i$$

ε_i = permittivity in region i (complex in region 1)

β = complex propagation constant (the same in all regions)

ω = radian exitation frequency

The solution to equation 5.5 is given in terms of modified Bessel functions of the first and second kind of order zero:

$$\Psi_i(r) = A_i\, I_o(k_{ci}r) + B_i\, K_o(k_{ci}r) \qquad (5.6)$$

(The choice of using modified Bessel functions or ordinary Bessel functions is arbitrary since the numerics have to be typed complex in either case. Modified Bessel functions were used due to convenience.)

When boundary conditions on tangential $\vec{E}$ and $\vec{H}$ are applied at the interfaces, all coefficients A_i and B_i can be eliminated except one

arbitrary coefficient. The resulting equation for a non-trivial solution is of the form:

$$f(\beta,\varepsilon_1) = 0 \tag{5.7}$$

The exact form of $f(\beta,\varepsilon_1)$ is given as reference material in Appendix C. The method of solving equation 5.7 is via graphical techniques or by treating one of the parameters as known and then numerically searching for the eigenvalues (the unknown parameter) using a complex root finding routine. Note that the complex conductivity of the plasma, σ_1, is contained in ε_1 via:

$$\varepsilon_1 = \varepsilon_0 \left(1 + \frac{\sigma_1}{j\omega\varepsilon_0}\right) \tag{5.8}$$

In solving equation 5.7 for the analysis of the experiments, β was treated as known (i.e. measurable) and ε_1 was the eigenvalue. Equations like 5.7 can have more than one eigenvalue ε_1 for a given β [28]. However, for the analysis of these experiments, ε_1 was unique for physically realistic values of discharge properties. The values of effective collision frequency, ν_e, were expected to satisfy $\nu_e/\omega < 10$. The eigenvalue ε_1 was verified to be unique up to $\nu_e/\omega = 100$ whereupon the question of the existence of another eigenvalue was not pursued further.

For the analysis, the real part of β was determined from ΔL and the theoretical empty cavity eigenlength at 2.459 GHz (L_{th}):

$$\beta_r = \frac{2\pi}{L_{th} + \Delta L} \tag{5.9}$$

The imaginary part of β was not measured directly, but the additional experimental measurements of P_p and E_{rw} were equivalent to a measure of β_i. This was accomplished by an iterative process: (1) a value for β_i was assumed and ε_1 was computed; (2) when ε_1 became known, $\vec{E}(\vec{r})$ was determined everywhere to within an arbitrary amplitude coefficient which in turn was determined by the measure of E_{rw}; and (3) the total power absorbed in the plasma per unit length was calculated and compared to P_p/L where L was the experimental plasma length (described in the previous chapter). The above steps were iterated numerically until the calculated absorbed power per unit length matched P_p/L.

Thus, the average plasma conductivity (σ_1), the $\vec{E}(\vec{r})$ and $\vec{H}(\vec{r})$ fields in the plasma/waveguide cross section and β_i were all determined from the experimental measurements within the geometrical approximation already described. A representative electric field in the plasma, E_p, was defined for ease of presentation of the results since the computed E-field cross sectional distributions were all similar. E_p was defined as the value of $|\vec{E}(\vec{r})|$ in the cross section at the radial point where the computed power density matched the experimental average power density (P_p/V, where V was the measured plasma volume). E_p is the same as would be calculated from a uniform E-field in a uniform plasma.

5.4 Determination of Average Electron Density and Effective Collision Frequency

The simplest form of the electrical conductivity of a gas discharge can be derived from the Langevin equation or from moments of the Boltzman equation [30,31]. This form is called the cold plasma conductivity and is regarded as an adequate description of the macroscopic conductivity of a collisional, weakly ionized discharge:

$$\sigma = \frac{N_e e^2}{m_e} \left(\frac{\nu - j\omega}{\nu^2 + \omega^2}\right) \tag{5.10}$$

where

N_e = electron density

ν = electron-neutral collision frequency

The $\vec{r}$ dependence was dropped from N_e, ν, and σ since only average quantities were of interest in the analysis. If ν is dependent upon the electron velocity, v, (as is the case for argon) equation 5.10 is no longer valid. However, by defining an effective collision frequency, ν_e, as [31,32]:

$$\nu_e = \frac{\int_o^\infty v^3 \frac{\nu(v)}{\nu(v)^2+\omega^2} \frac{\partial f_o}{\partial v} dv}{\int_o^\infty v^3 \frac{1}{\nu(v)^2+\omega^2} \frac{\partial f_o}{\partial v} dv} \tag{5.11}$$

where f_o is the first term of the expansion of the velocity distribution function of the electrons, the form of equation 5.10 remains valid with ν_e replacing ν.

Rewriting equation 5.10 using $\sigma = \sigma_r + j\sigma_i$:

$$\sigma_r + j\sigma_i = \frac{N_e e^2}{m_e} \frac{\nu_e}{\nu_e^2+\omega^2} - j \frac{N_e e^2}{m_e} \frac{\omega}{\nu_e^2+\omega^2} \tag{5.12}$$

By separating equation 5.12 into real and imaginary parts, N_e and ν_e were algebraically determined from σ.

5.5 Determination of Gas Temperature

Approximate gas temperatures in the discharges were calculated using a simple 2-dimensional radial heat conduction model. The geometry of this problem was the same as that of Figure 5.3 with only regions 1 and 2 needed for the analysis. The basic assumptions for this analysis were (1) axial uniformity; (2) power per unit length was dissipated uniformly inside r = a through joule heating in the plasma, (3) power was lost from the plasma only through heat conduction (convective losses and radiative losses were neglected), and (4) the quartz boundary at r = b was assumed to be at 300^{o} K (in the experiments, the quartz tubes were cooled using forced air and did not heat up significantly). Because of the rotational symmetry, all variables were only a function of the radial coordinate r.

The basic equation governing heat flow due to dissipated power in a plasma is [31]:

$$\nabla \cdot (k(\vec{r}) \nabla T(\vec{r})) = -\frac{1}{2} \mathrm{Re}[\vec{J}(\vec{r}) \cdot \vec{E}(\vec{r})^{*}] \qquad (5.13)$$

For the geometry and assumptions of the experiment, equation 5.13 can be integrated to obtain a first order differential equation in r:

$$k(r) \frac{dT(r)}{dr} = -\frac{1}{2\pi rL} P(r) \qquad (5.14)$$

where:

$P(r)$ = total power dissipated within r for a plasma of length L

$k(r)$ = thermal conductivity

$T(r)$ = neutral gas temperature

$2\pi rL$ = surface area (neglecting the ends of the plasma column)

The form for $k(r)$ was taken to be [33,34]:

$$k(r) = k_o T(r)^{\frac{1}{2}} \tag{5.15}$$

Using parameters in reference [33], k_o for argon gas was calculated to be 1.56×10^{-3} Joule/(meter-sec-$^oK^{3/2}$). A value of k_o used by Eden for similar calculations on argon gas was 1.77×10^{-3} (same units)[34]. The latter value for k_o was used in all calculations although it did not make a significant difference which value was used.

The primary region of interest was $r \leq a$, where:

$$P(r) = \frac{r^2}{a^2} P_p \tag{5.16}$$

Solving equation 5.14 using this form for $P(r)$ resulted in:

$$T(r) = [T(a)^{3/2} + \frac{3}{8\pi k_o} \frac{P_p}{L} (1 - \frac{r^2}{a^2})]^{2/3} \tag{5.17}$$

where

$$T(a) = [300^{3/2} + \frac{3}{4\pi k_o} \frac{P_p}{L} \ln(\frac{b}{a})]^{2/3}$$

An average gas temperature was defined to be the average of the maximum temperature at the center of the plasma and the temperature at the plasma edge:

$$T_g = \frac{1}{2} [T(o) + T(a)] \tag{5.18}$$

5.6 Determination of Electron Temperature

The EM analysis described in Section 5.3 and the cold plasma theory stated in Section 5.4 allowed the calculation of ν_e from experimental measurements. By assuming a form for the distribution function, equation 5.11 can be solved numerically to obtain T_e from ν_e.

Defining:

p = pressure (measured)

$p_o = \frac{273}{T_g} p$ = reduced pressure

$c(v)$ = collision cross section of argon (tabulated)

k = Boltzman's constant

Assuming a Maxwellian velocity distribution function [33], equation 5.11 can be simplified to:

$$\frac{\nu_e}{p_o} = \frac{\int_o^\infty \frac{c(v)v}{273k} g(v)\, dv}{\int_o^\infty g(v)\, dv} \tag{5.19}$$

where

$$g(v) = \frac{v^4}{\left(\frac{c(v)v}{273k}\right)^2 + \left(\frac{\omega}{p_o}\right)^2} e^{-\frac{m_e v^2}{2kT_e}}$$

Using tabulated data for c(v) for argon gas [35,36], equation 5.19 was solved numerically to obtain T_e for each data point. Similar calculations have been done by Glaude et al., on argon surface wave discharges at low pressures [37].

5.7 Discussion of Potential Accuracy of the Results

5.7.1 Accuracy of the Measurements and the Experimental Technique

The four measurements used in the EM portion of the analysis were described in Section 3.4. The accuracy in each measurement was estimated to be: $\pm$ 1% in P_p and ΔL; and $\pm$ 10% in d_{ave} and E_{rw}. Potential errors due to the cavity imperfections were approximately accounted for in the measurement of ΔL. Frequency drifts of the source were small enough to not present a significant source of error.

As a test on the overall accuracy of the experimental technique (including the various cavity imperfections), the complex dielectric constant of a homogeneous, lossy material was diagnosed. A quartz tube filled with distilled water was placed in the cavity in the same location as the discharges. To keep from heating the water above room temperature, the power level of about 50 watts from the source was scaled down by a factor of 100 prior to entering the waveguide system and the measurements were taken rapidly. A computed value of ε_r = 67-j10.5 of the water compared reasonably well to an interpolated value from Harrington [20] of ε_r = 77-j9.7. This result was well within the expected accuracy of the technique and indicates that the experimental measurements and analysis were adequate for diagnosing properties of a homogeneous material.

5.7.2 Effect of Plasma Inhomogeneities

The analysis in Section 5.3 assumed a homogeneous plasma column and, in effect, averaged out radial and axial variations in the discharges. The effect of radial inhomogeneities in plasma columns diagnosed with a TM_{01n} cavity mode has been investigated analytically [24]. For high density plasmas ($\omega_p > \omega$), the average electron density determined by a homogeneous plasma model was found to be a good estimate of the actual average electron density as long as the plasma radius was less than or equal to the skin depth. Since all the discharges analyzed in this dissertation met this requirement, radial variations were thus not expected to introduce large errors into the computed averages.

For the high pressure surface wave discharges (Appendix A), the effect of radial variations on dispersion characteristics and electric field distributions was investigated analytically. This comparison (on plasma filaments of the same size and electron density as the ones generated in the TM_{012} mode) demonstrated that there was little change between a radially inhomogeneous plasma and a homogeneous plasma with an electron density equal to the average density of the radially inhomogeneous one. Because of the similarities in the field patterns inside the plasma between the TM_1 surface wave mode and the TM_{01} plasma/wavequide mode, similar results would be expected.

Thus, the major uncertainty in the effect of plasma variations is to what extent the axial averaging process was a good approximation. This is difficult to ascertain since solving the analytic problem for even a simple case would be very complex.

5.7.3 Accuracies of the Plasma Models

As described in Section 5.4, the cold plasma conductivity model is considered a very good description of this type of discharge and would not be expected to introduce any significant additional error into the results for electron density and effective collision frequency. The models used for the calculation of gas temperature and electron temperature, however, contained more assumptions. If any of those assumptions were not good ones, then the results would be more open to error. For example, in the radial heat conduction model if the quartz wall temperature was significantly higher than $300^{o}K$, T_g would be underestimated. Also, the visible upward convection currents in the larger tubes might play a significant role in cooling the discharges. In this case, the gas temperatures might be overestimated. The power leaving the discharge due to light emission might also introduce some error into the calculations. An advantage of the radial heat conduction model, however, is that T_g was calculated directly from P_p and d_{ave} which were both of good accuracy.

The calculation of electron temperature had all the errors from ν_e, T_g and the measurement of gas pressure as inputs. Thus, the combination of those errors would tend to make T_e less certain. Also, the degree that the distribution function was non-Maxwellian in the vicinity of the Ramsaur minimum (of argon collision cross sections [31]) could also introduce a significant error into the computed average energies of the electrons.

5.7.4 Conclusions on the Overall Accuracy of the Results

A detailed analysis of the accuracy of the results was not part of

the defined work in this dissertation and is left for future research. The results are expected to at least be within the correct order of magnitude, and probably the accuracy is much better than that. The check on the dielectric constant of distilled water indicates that as far as plasma diagnostic methods go, this technique could be very accurate.

The desire to assess the accuracy of the results was one of the main motivations for extending the experiment down to lower pressures, where there is more experimental data on argon microwave discharges from other diagnostic methods. Also, there is a theory for certain discharge properties that is often used to describe microwave discharges. These low pressure results are presented in Appendix B and generally support the estimates of accuracy given in this section.

CHAPTER VI

ELECTRON DENSITY, ELECTRIC FIELD AND OTHER DISCHARGE PROPERTIES

6.1 Introduction

This chapter contains results on discharge properties of the high pressure argon filaments determined by the analysis described in Chapter V. The order of presentation of the results basically follows the flow of the analysis. All discharge properties represent spatial averages over radial and longitudinal variations in the discharges. The frequency of excitation was 2.46 GHz. All results pertain to the specific experimental geometry in Figure 4.6a (i.e. vertical orientation, discharges approximately centered in the tube cross section and a common total discharge length of about 16 cm). The four discharge tubes were those described in Figure 4.8. At the conclusion of the chapter is a summary of discharge properties at 1 ATM for comparison with the literature reviewed in Chapter II.

A common thread exists among all of the figures in this chapter where pressure is on the horizontal axis, and Figures 4.9 and 4.10 of Chapter IV. That common thread is that a single experiment at a particular pressure resulted in a data point on each of the figures at that particular pressure. Since each discharge/tube geometry has its own symbol which is the same in all figures, the discharge properties of a single experiment (i.e. N_e, ν_e, E_p, T_g, T_e, etc.) can be extracted from the figuresif desired.

6.2 Coupling Efficiency, Electron Density and Effective Collision Frequency

With a plasma present in the cavity, the power lost into the coupling structure was usually no more than 1% of the total power absorbed by the cavity (i.e, Eff $\geq$ 99% for all experiments). This was due to the plasma lowering Q_u in the TM_{012} mode to values less than 100 as can be seen in Figure 6.1. Q_u generally decreased with increasing pressure - indicating that as the plasmas became more lossy, the coupling efficiency (Eff) increased. For a common discharge length, there was little difference in Q_u at a constant pressure between the different discharge/tube geometries. Coupling efficiencies to microwave discharges are not always as high as these efficiencies. In the low pressure experiments (Appendix B), values of Eff were as low as 60% at .02 torr.

Figure 6.2 displays average electron densities (N_e) versus pressure for the different discharge/tube geometries. In each tube, N_e increased as pressure was increased. At a constant pressure, there were distinct differences in N_e depending upon the discharge/tube geometry (similar to the differences in average power density described in Section 4.5). For example, at 1 ATM N_e increased from $3.2 \times 10^{13}/cm^3$ for a discharge in the 12 mm tube to $2.7 \times 10^{14}/cm^3$ for a discharge in the 1.5 mm tube. Adding power also resulted in changes in N_e similar to those of <P> described in Section 4.5. As can be seen in Figure 6.3, power increases produced primarily increases in discharge volume for the 4.0 mm tube and and larger tubes (resulting in N_e remaining approximately constant). In the 1.5 mm tube, however, volume increases were restricted by the small tube diameter and N_e increased with increases in P_p.

Changes in average effective collision frequency (ν_e) with pressure and discharge/tube geometry are shown in Figure 6.4. In all tubes, there

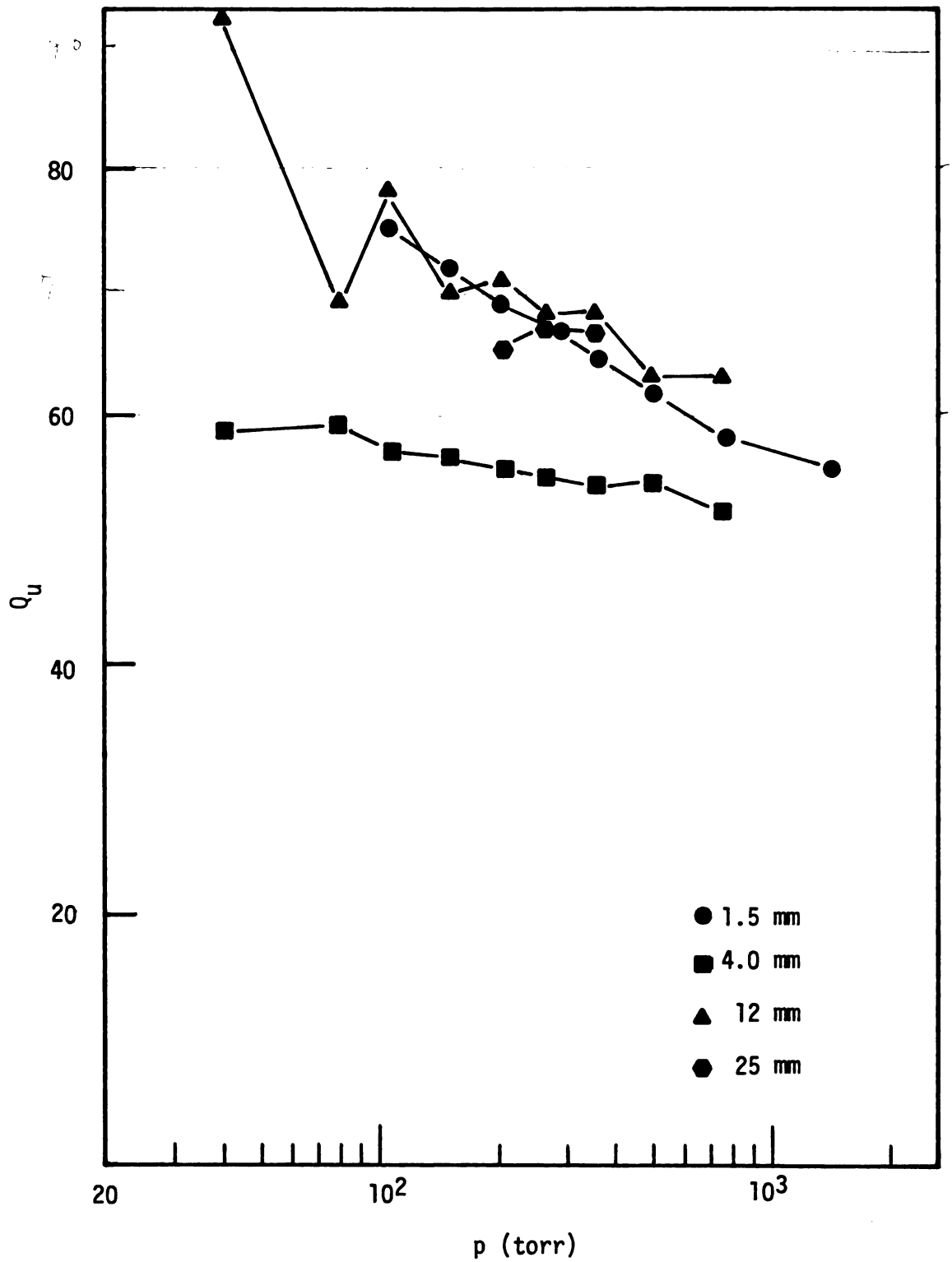

Figure 6.1 Unloaded cavity Q, Q_u, for discharges in the four tubes oriented vertically.

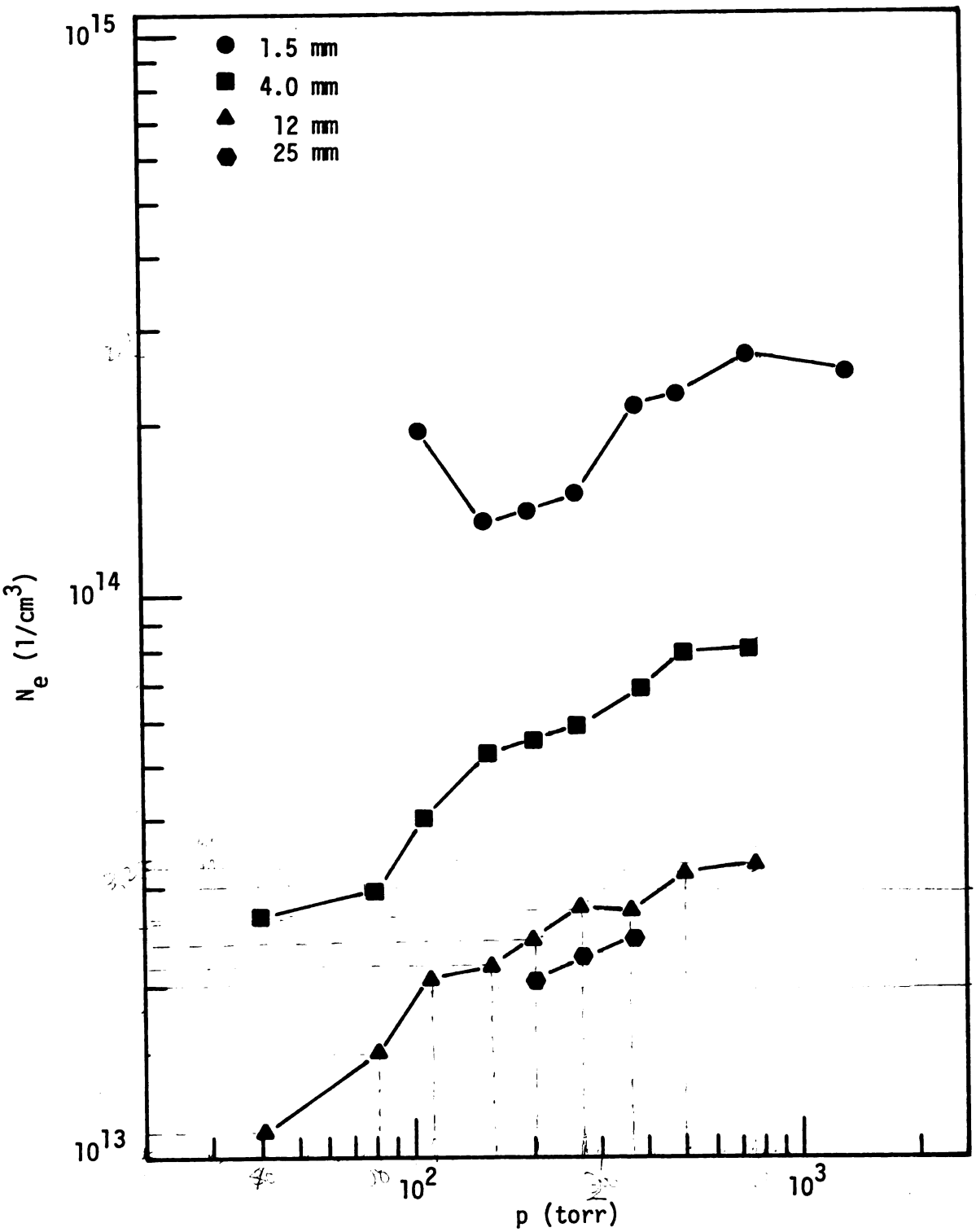

Figure 6.2 Electron density, N_e, for discharges in the four tubes oriented vertically.

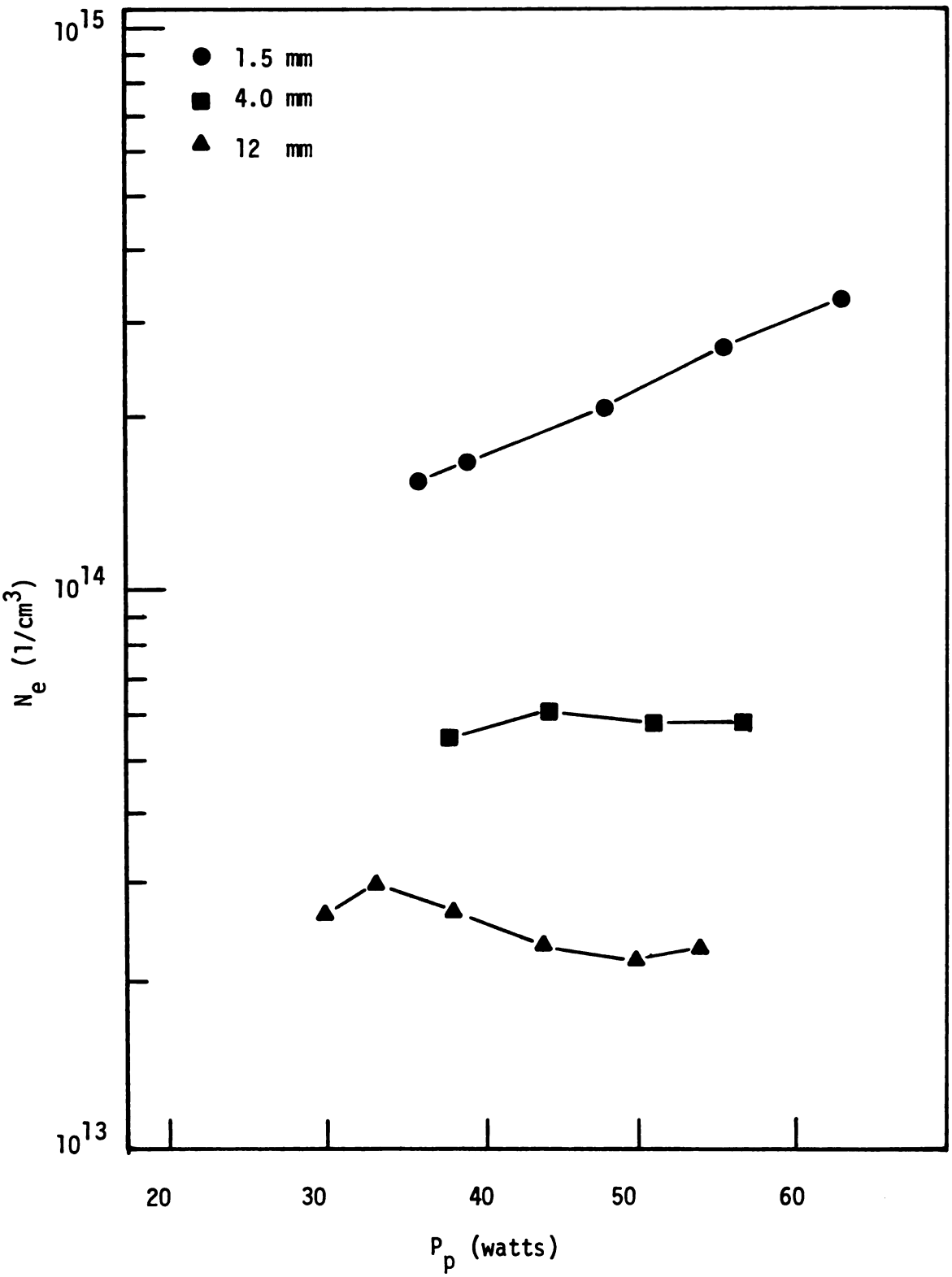

Figure 6.3 Effect of adding power on electron density at a constant pressure of 265 torr.

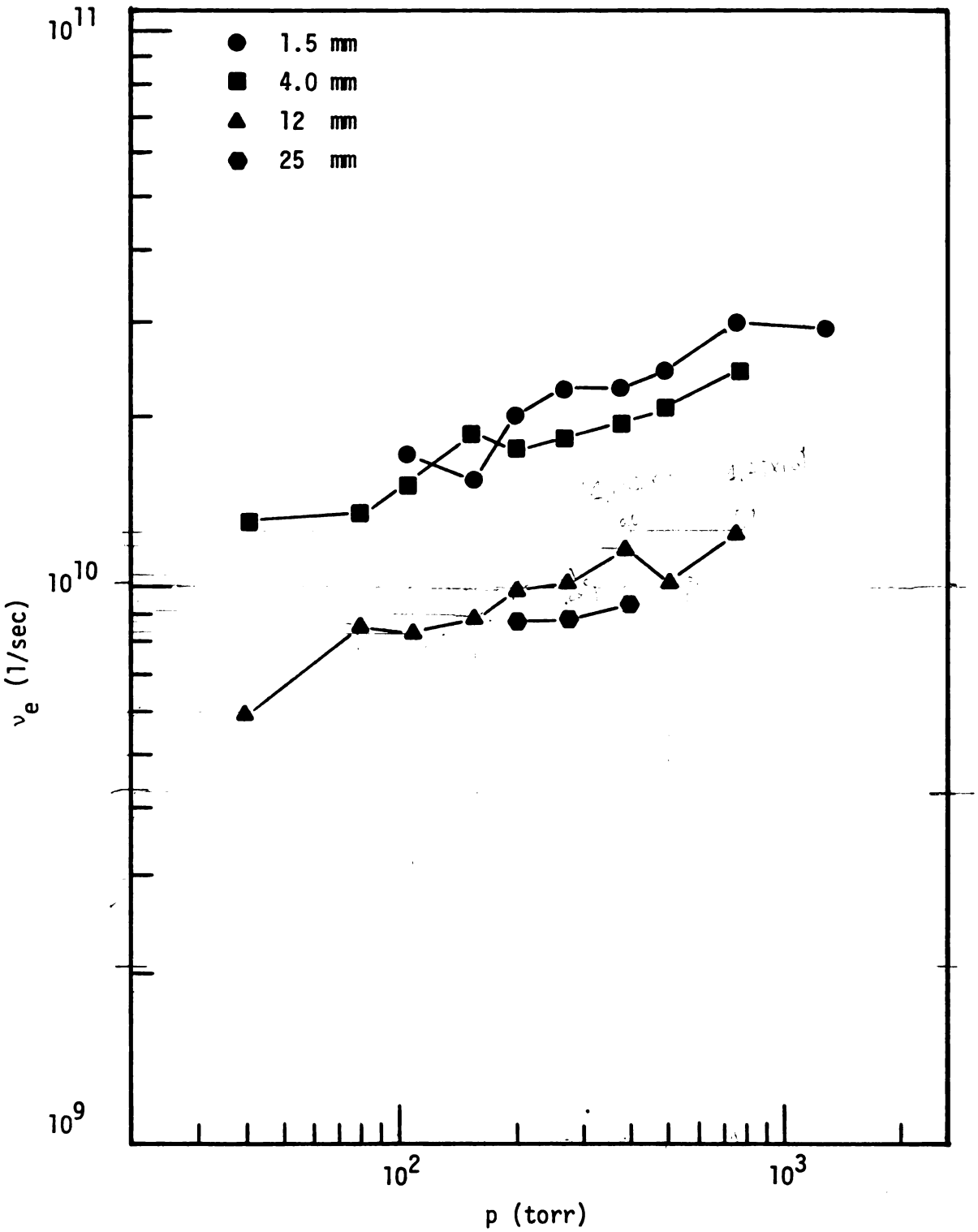

Figure 6.4 Effective collision frequency, ν_e, for discharges in the four tubes oriented vertically.

was only a gradual increase in ν_e with pressure - much less of an increase than would be expected from assuming that the neutral particle density in the discharges increased directly with pressure. This gradual increase in ν_e indicates that the neutral gas temperature increased with pressure, causing the neutral particle density in the discharges to increase more slowly than directly with pressure. The different discharge/tube geometries produced changes in ν_e, but not to as great an extent as the changes in N_e. For example, at 1 ATM ν_e increased from 1.2×10^{10}/sec for a discharge in the 12 mm tube to 3.0×10^{10}/sec for a discharge in the 1.5 mm tube. At a constant pressure, ν_e was approximately constant with changes in absorbed power in all discharge/tube geometries.

6.3 Electric Field Distributions, Plasma Electric Field and Effective Electric Field

Due to the type of analysis in Chapter V, cross sectional field distributions in and around the discharges were calculated for an axial average point in the standing wave of the TM_{012} plasma/cavity mode. Figure 6.5 displays calculated distributions of $|E_r(r)|$ and $|E_z(r)|$ for this average cross section for a 265 torr discharge in the 4.0 mm tube. The distributions of $|E_r(r)|$ and $|E_z(r)|$ were relatively unchanged from the ideal empty cavity distributions (described in Appendix C) for r greater than about 1 cm.

Figure 6.6 displays the same distributions as in Figure 6.5 for the region of the cavity (near the plasma) where the E-field distributions were significantly changed from those of the empty cavity. $|E_r(r)|$ was relatively high outside the plasma near the plasma boundary but was relatively small inside the plasma as compared to $|E_z(r)|$. Thus, the longitudinal component of electric field (which is not discontinuous at the plasma boundary) was

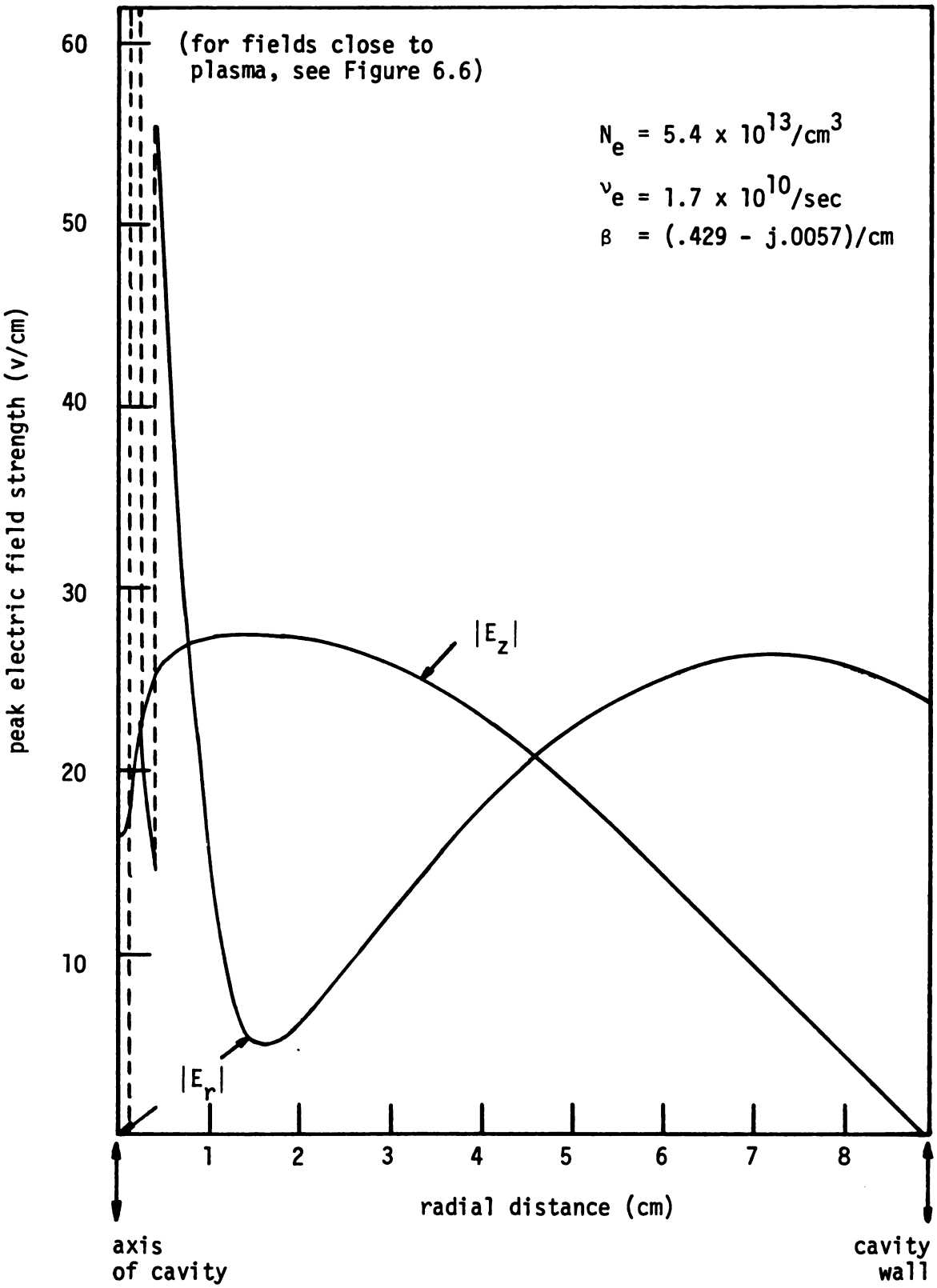

Figure 6.5 Radial dependence of $|E_r(r)|$ and $|E_z(r)|$ for the average axial point in the standing wave (265 torr, 4.0 mm tube).

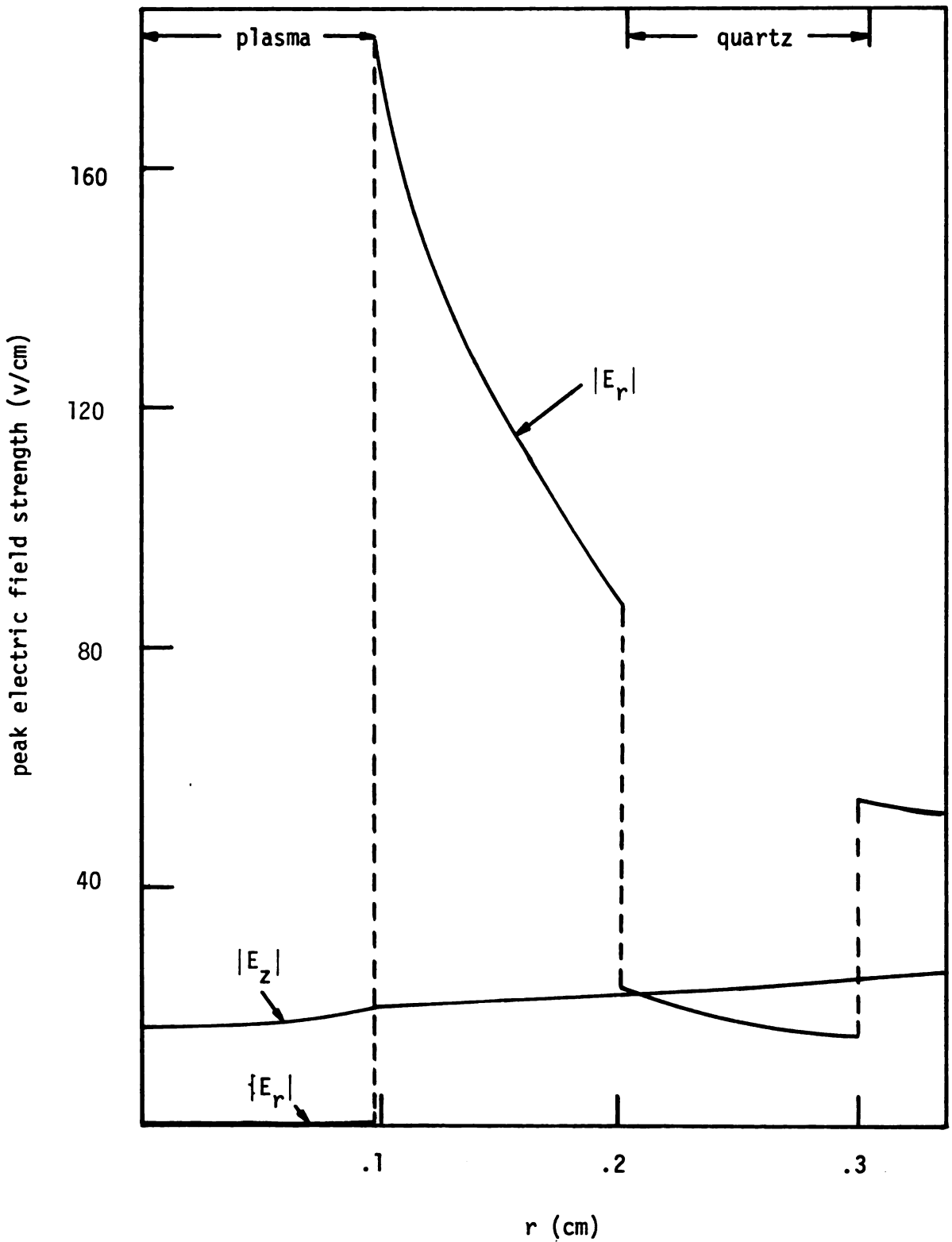

Figure 6.6 Radial dependence of $|E_z(r)|$ and $|E_r(r)|$ near the plasma for the same discharge parameters of Figure 6.5

the most important component in heating and maintaining the plasma. These results are consistent with the observations and assumptions about the TM_{012} mode made in Chapter IV. Also, Figure 6.6 shows that the radial distribution of $|E_z(r)|$ was reasonably uniform in the plasma, the intensity at the plasma boundary being only about 25% higher than the intensity at the center of the plasma.

Figure 6.7 describes the computed changes in $|E_z(r)|$ in the cavity with changes in power absorbed by a discharge in the 4.0 mm tube. Adding power raised the intensity level of the fields in the cavity, as determined by the measurement of E_{rw}. This increase in intensity level, however, was not in proportion to the amount of power added, i.e. doubling the absorbed power only caused a slight increase in the field strengths inside the cavity. Since increases in absorbed power also caused increases in plasma diameter, the net result was that there was little change in the E-field intensity in the discharges with increases in absorbed power. Similar effects were noted for discharges in larger tube sizes and for other pressures. For discharges in the 1.5 mm tube, computed strengths of $|E_z(r)|$ actually decreased in the plasma with increasing absorbed power, presumeably due to the increases in N_e. This result is shown in Figure 6.8.

Since all computed E-field distributions (but not intensities) at all pressures were similar to those shown in Figures 6.5 and 6.6, an average electric field in the plasma (E_p) was defined in Chapter V to compare how the intensity levels changed with pressure and discharge/tube geometry. Figure 6.9 displays these changes, showing that in general E_p increased with pressure. At a constant pressure, values of E_p were generally lower in discharges having higher electron densities.

An effective electric field (E_e) is often defined for microwave

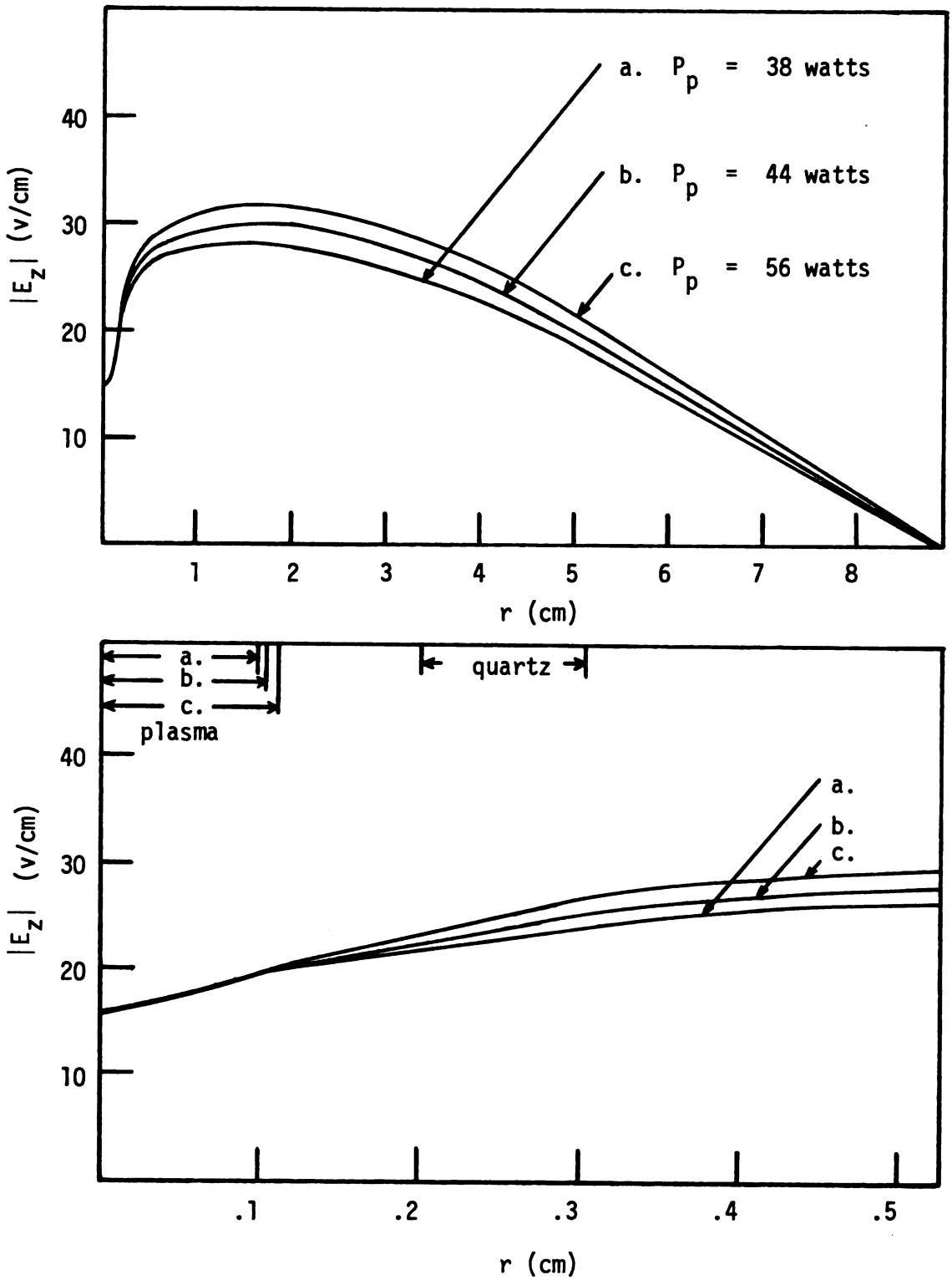

Figure 6.7 Effect of adding power to the distribution of $|E_z(r)|$ (265 torr, 4.0 mm tube).

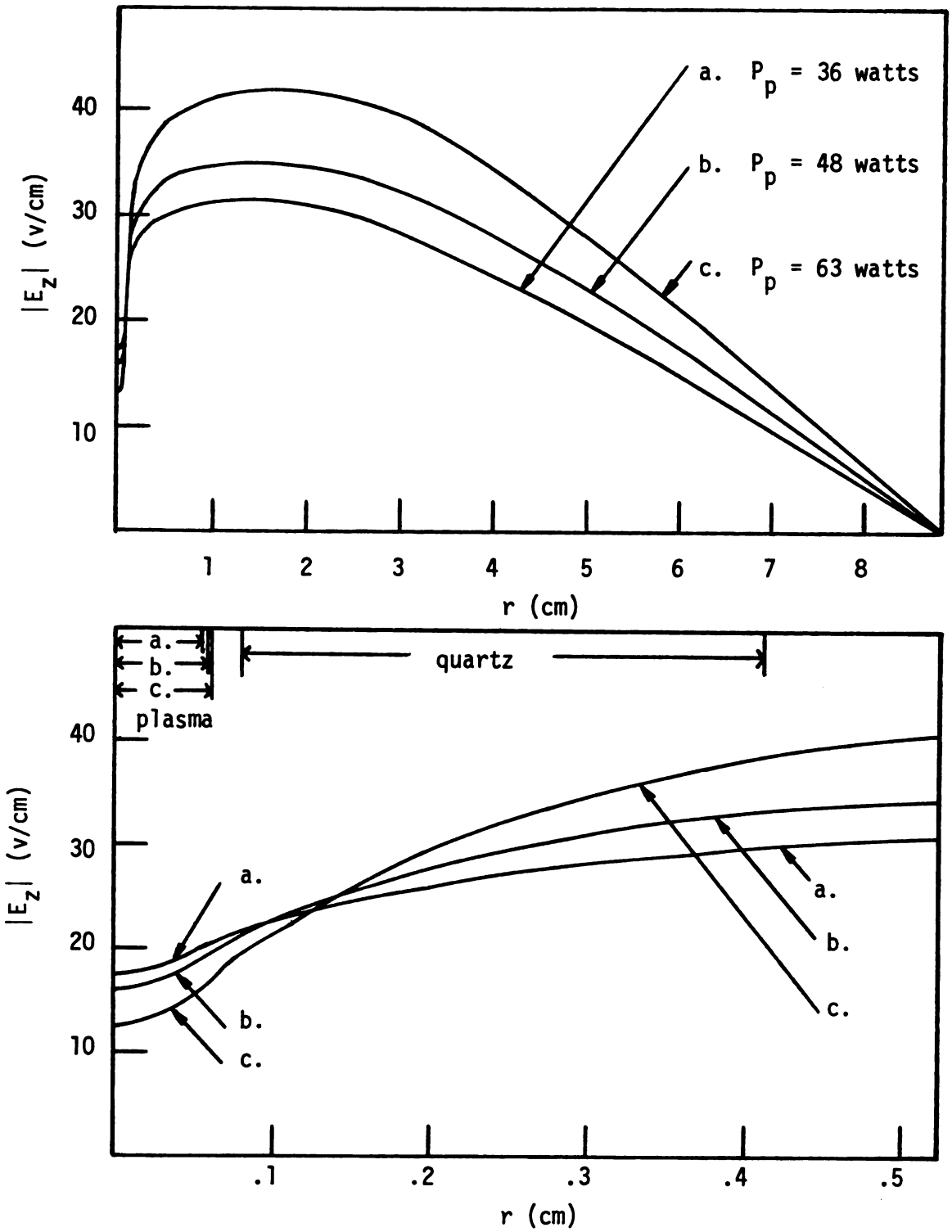

Figure 6.8 Changes in $|E_z(r)|$ with absorbed power for the 1.5 mm tube at 265 torr.

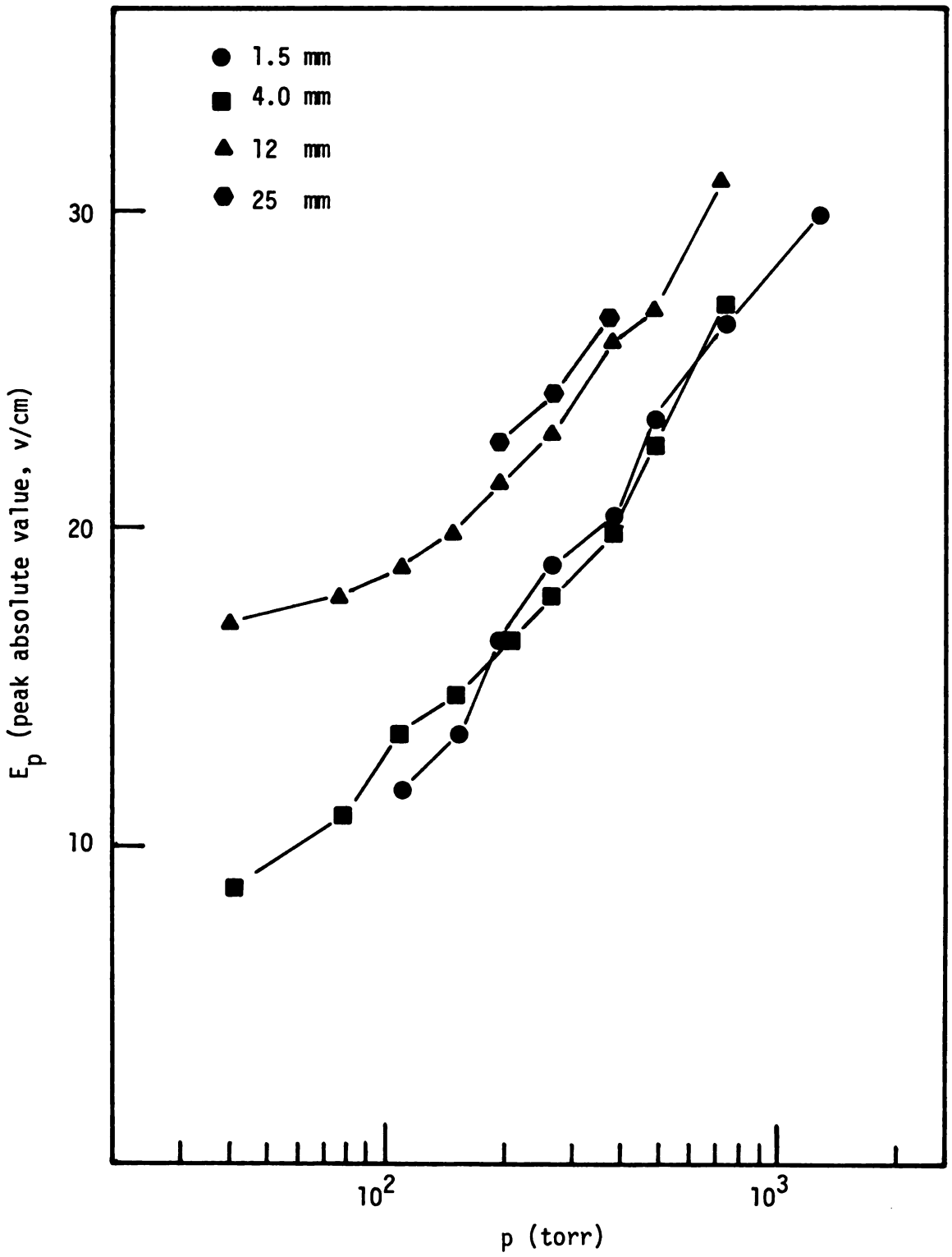

Figure 6.9 Plasma electric field strength, E_p, for discharges in the four tubes oriented vertically.

discharges to compare with the E-field strength in a d.c. discharge [38]. For these discharges, E_e was defined in terms of E_p:

$$E_e^2 = \frac{E_p^2}{2} \frac{\nu_e^2}{\nu_e^2+\omega^2} \tag{6.1}$$

Figure 6.10 plots E_e versus p_o, where p_o was reduced pressure defined in Section 5.6. Calculated gas temperatures to be described in the next section were used to determine p_o. As can be seen in Figure 6.10, E_e was relatively constant at a given p_o. The values of E_e at the low end of the pressure regime appear to be approaching typical E-field values of 2-4 v/cm at 10 torr in contracted argon positive columns (i.e. d.c. discharges) [39]. Also, the values of E_e at 1 ATM (i.e., p_o between 150 and 200 torr) agree well with the effective electric field strength of 15 v/cm in a 34 MHz argon discharge at atmospheric pressure [7]. Figure 6.11 displays the same results of E_e in a different way, plotting E_e/p_o versus p_o.

6.4 Gas Temperature and Electron Temperature

Figure 6.12 displays T_g versus gas pressure for the four discharge/tube geometries. In general, T_g increased with pressure, consistent with the observations made on the dependence of ν_e with pressure. Also, T_g increased at a constant pressure as the discharges were formed further from the quartz wall (in a larger tube). Using the radial heat conduction model, this is a result of discharges in a large tube being more insulated from the quartz wall than discharges in a smaller tube.

Figure 6.13 displays T_e versus pressure and discharge/tube geometry. A distinct difference was calculated between the two smaller tubes and the two larger tubes which was a result of the differences observed in ν_e (from

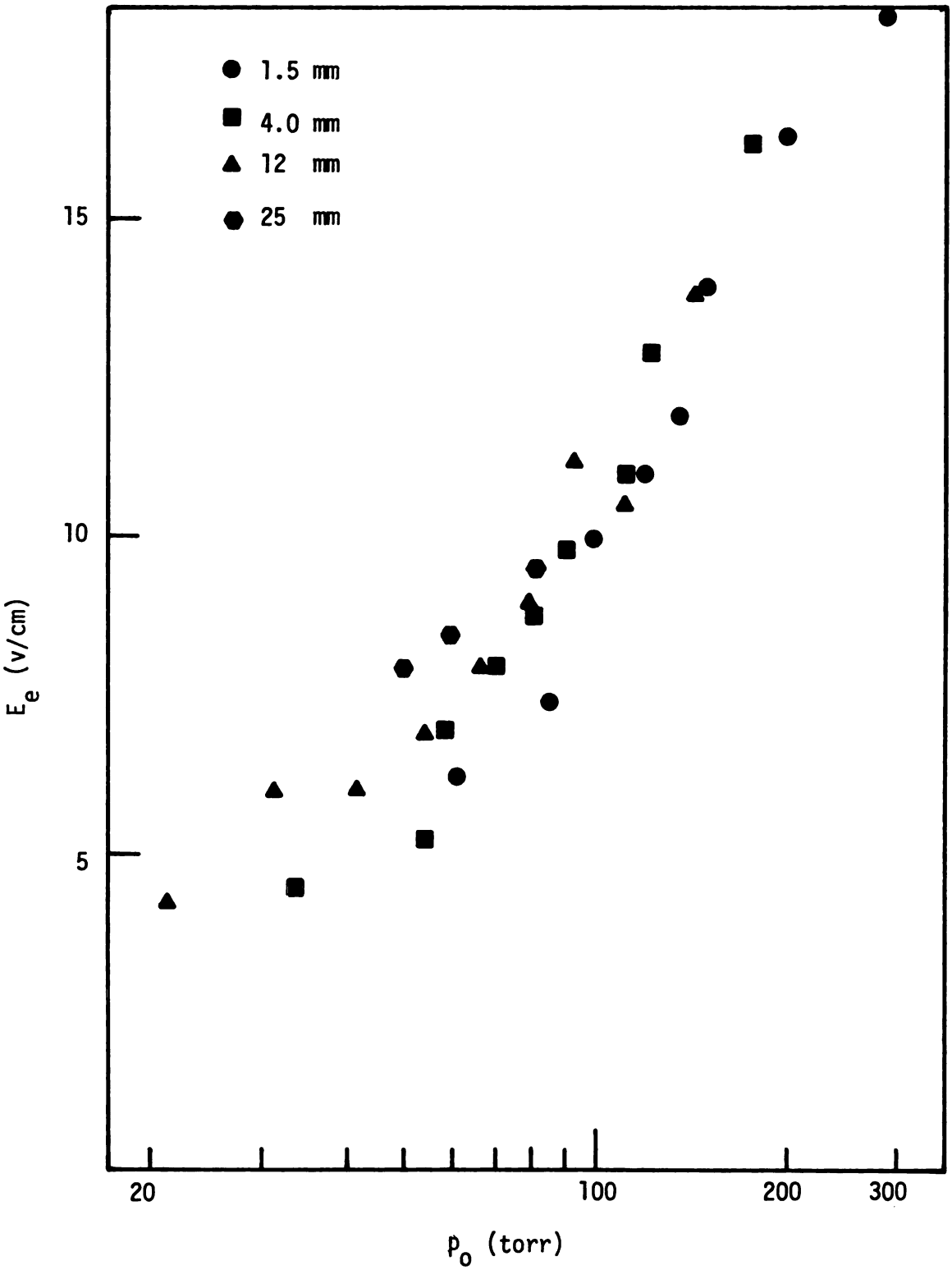

Figure 6.10 Effective electric field, E_e, for discharges in the four tubes oriented vertically.

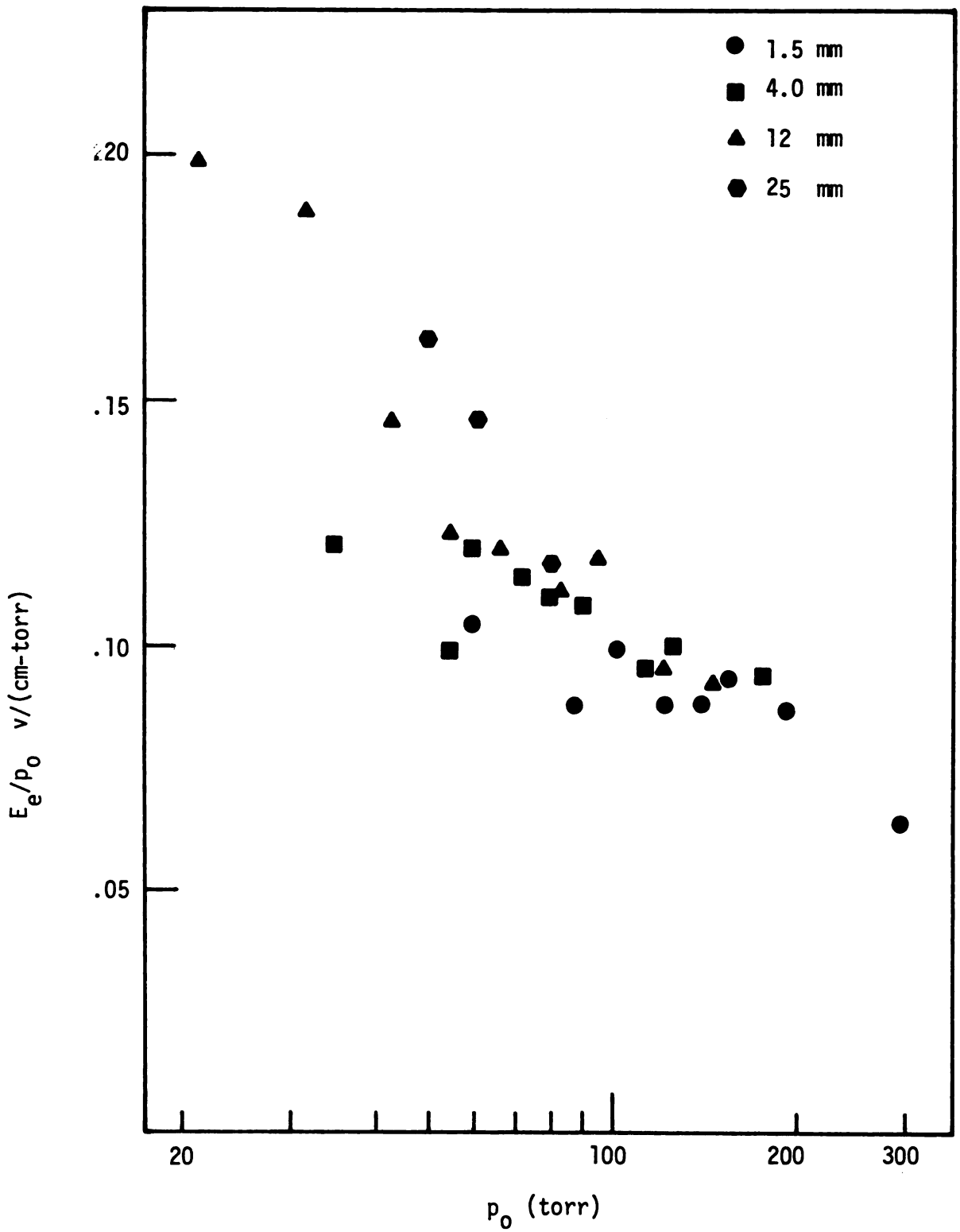

Figure 6.11 E_e/p_o versus p_o for discharges in the four tubes oriented vertically.

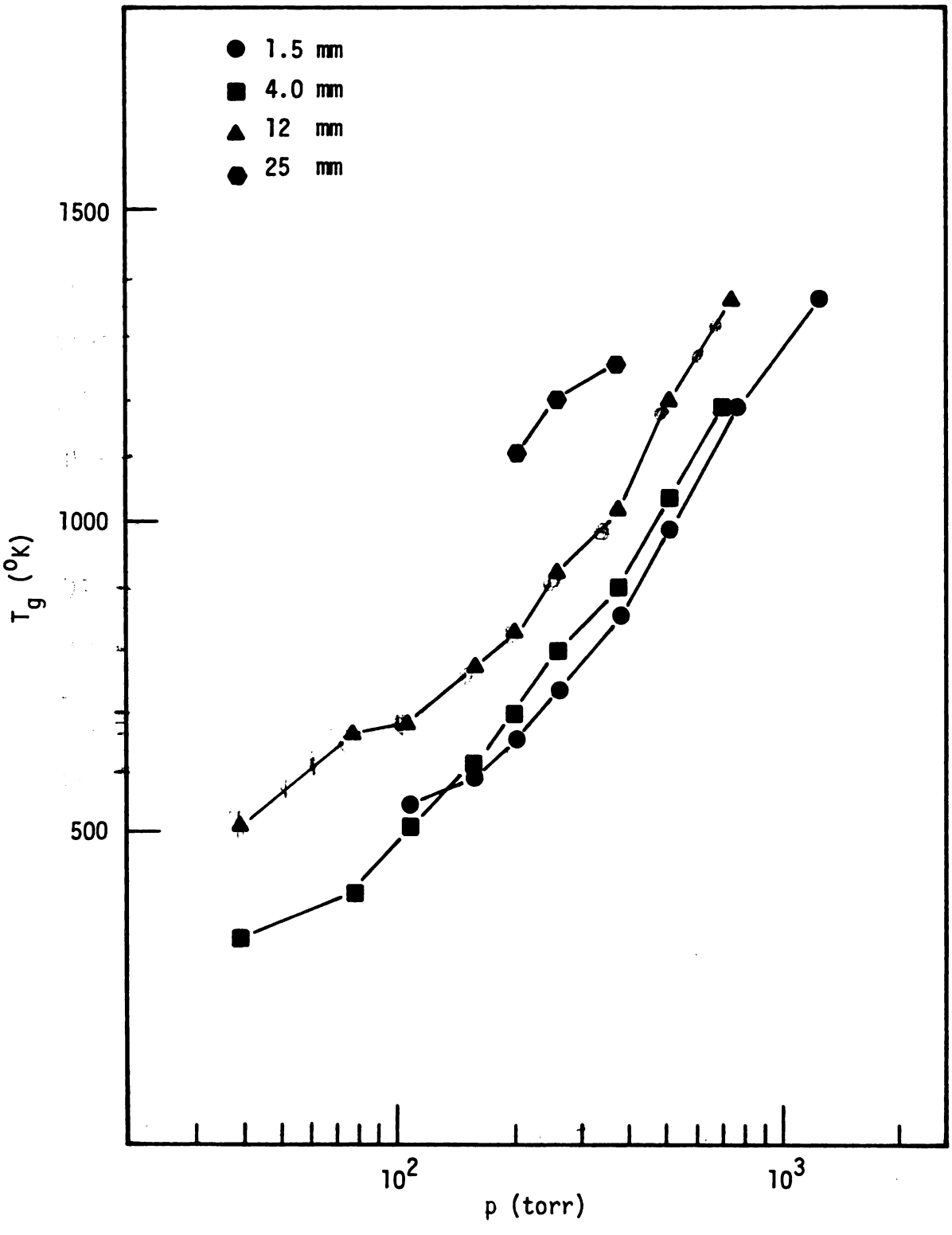

Figure 6.12 Gas temperature, T_g, for discharges in the four tubes oriented vertically.

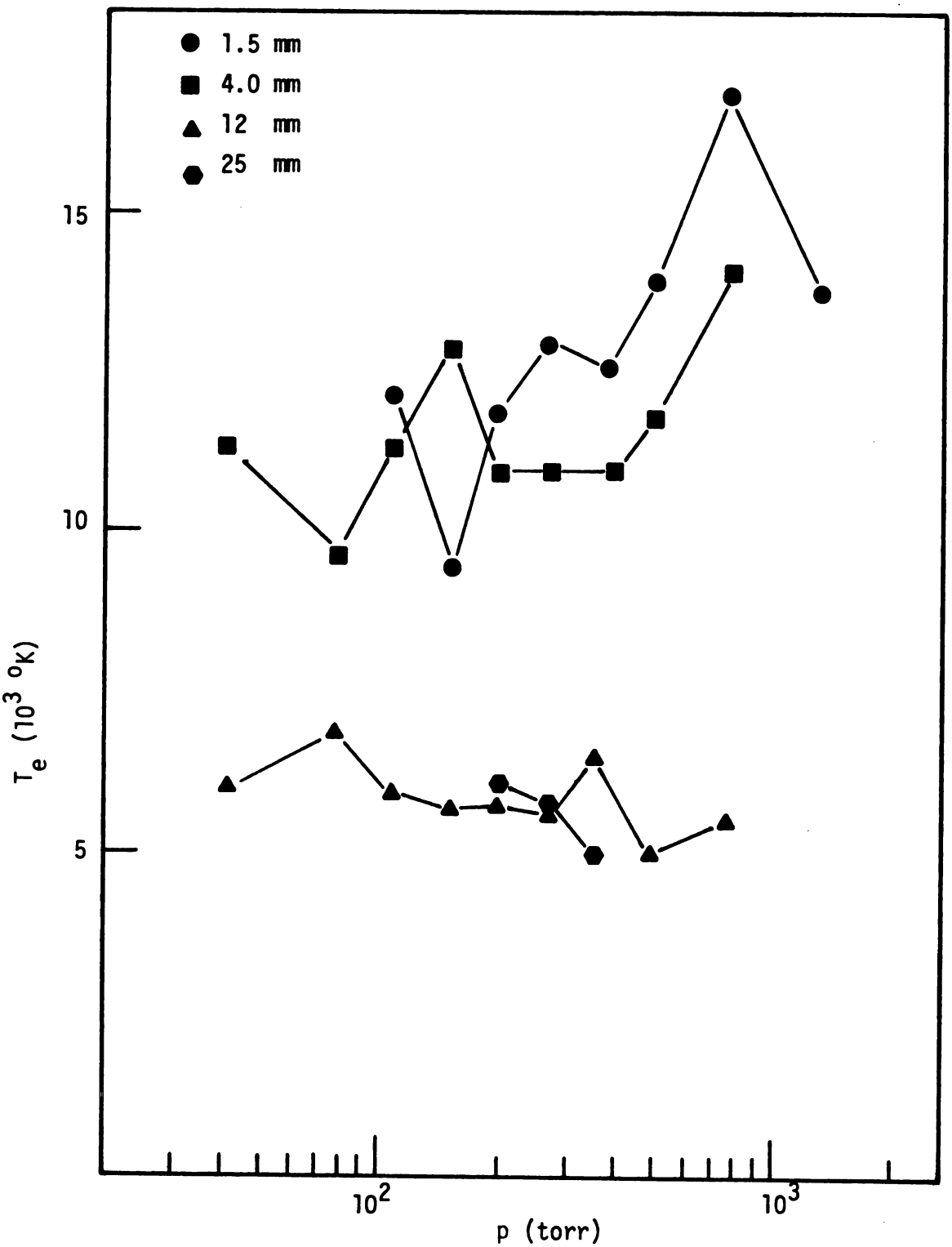

Figure 6.13 Electron temperature, T_e, for discharges in the four tubes oriented vertically.

which T_e was calculated). Conceivably, the distribution function could have changed with the change in discharge/tube geometry and thus might be contributing to the calculated differences in T_e. In any event, the order of magnitude of these values of T_e appears to be reasonable. In a 34 MHz argon discharge at 1 ATM (with the discharge not bounded by a quartz tube), T_e was spectroscopically determined to be about $6700^{o}K$ [7], which agrees reasonably well with the values of T_e determined for discharges in the 12 mm tube.

6.5 Summary of Discharge Properties

Table 6.1 presents a summary of discharge properties at 1 ATM for the 12 mm tube (representative of the two larger tubes) and the 1.5 mm tube (representative of the two smaller tubes). The differences in discharge properties which resulted from only a difference in tube size appear to be caused by the different rates of energy flow out of a unit volume of the discharges (indicated directly by the absorbed power densities). These different rates of energy flow are most probably different rates of cooling the discharge. The presence or absence of forced flow rate of gas is another cooling mechanism that would be expected to cause changes in discharge properties.

The reviewed papers in Chapter II which permit the closest comparison with the results in this section are the argon surface wave discharges of Hubert [17] and Moisan [15]. Both papers concerned atmospheric pressure microwave discharges generated in small diameter quartz tubes (but both, however, had varying degrees of flow rate of gas). Values of N_e obtained in the 1.5 mm tube ($2.7 \times 10^{14}/cm^3$) compared well to values obtained by Hubert and Moisan of $3\text{-}6 \times 10^{14}/cm^3$ for flowing argon discharges in a 5 mm

		12 mm i.d. vertical orientation	1.5 mm i.d. vertical orientation
average diameter	cm	.185	.094
power density	w/cm^3	130	700
electron density	$1/cm^3$	3.2×10^{13}	2.7×10^{14}
effective collision frequency	1/sec	1.2×10^{10}	3.0×10^{10}
plasma E-field (peak absolute value)	v/cm	31	26
effective electric field	v/cm	14	16.5
gas temperature	^oK	1400	1100
electron temperature	^oK	5500	17,000

Table 6.1 Summary of the experimental results on non-flowing, steady-state, argon microwave discharges for a pressure of 1 ATM. All properties (except diameter) are spatial averages over radial and axial discharge variations.

i.e. tube (presumeably oriented horizontally) [17] and a 2 mm i.d. tube [15]. Calculated values of T_g in the 1.5 mm tube (~ 1200 ^oK) were lower than those given by Hubert of ~ 2300 ^oK in argon + .5% N_2. The presence of nitrogen in Hubert's discharge (which greatly affected the macroscopic appearance of the discharge and approximately doubled the absorbed power density) may have contributed to this difference in T_g.

CHAPTER VII

CONCLUSIONS AND RECOMMENDATIONS

7.1 Introduction

The experiments described in this dissertation have extended the knowledge of high pressure microwave discharges in three ways: (1) these detailed results on argon discharges provide results from a different diagnostic approach than previous investigations, (2) the relationship between the EM fields to the orientation, size and shape of filamentary microwave discharges is studied to a much greater extent than previously, and (3) the overall method of generating and diagnosing the discharges (i.e. in well defined EM fields) is viewed as a superior approach to the study of microwave discharges than previous investigations. The remainder of this chapter will amplify the above general conclusions. A result of this investigation is a better understanding of how different rates of energy transfer out of the discharge affect its size and properties. This understanding gained in argon discharges provides insight into the behavior of high pressure microwave discharges in other gases.

7.2 High Pressure Argon Microwave Discharge Properties

Typical values of electron density and other discharge properties at 1 ATM determined by this investigation are listed in Table 6.1 in the last chapter. The observations in Chapter IV and the results of

Chapter VI allow the following conclusions about properties of steady-state argon microwave discharges in the pressure range of 40-1300 torr and for absorbed power levels up to 150 watts:

(1) The efficiency of coupling microwave power into the discharge is high. Coupling efficiencies greater than 99% can be expected when the discharges are generated in a high Q cavity (i.e., $Q_{uo} \geq 10{,}000$).

(2) For a given discharge/tube geometry and power absorbed, when gas pressure is raised: (a) discharge dimensions decrease; (b) electric field strength, absorbed power density and gas temperature all exhibit strong increases; and (c) electron density and effective collision frequency exhibit small increases.

(3) At any given reduced pressure, the effective electric field strength in the discharge is approximately constant - independent of changes in discharge/tube geometry or electron density. The values of effective electric field appear to be comparable to the values of E-field strength in argon d.c. discharges.

(4) Plasma properties are greatly affected by the rate of removal of energy from the discharge. For example, at a constant pressure and with no gas flow, changes in the relative distance from the discharge to the quartz wall produced changes in the rate of cooling of the discharges. Thus, changes of tube orientation from horizontal to vertical (in a gravity environment) and/or changes in tube size greatly affect discharge properties. Significant flow rates of gas would also be expected to produce changes in discharge properties.

(5) Adding power to the discharge at a constant pressure and in a given discharge/tube geometry results primarily in increased plasma volume with discharge properties remaining roughly constant. When volume increases are restricted (such as by a small diameter quartz tube) absorbed power density and electron density increase with increases in absorbed power and the microwave electric field strength decreases.

(6) The filament diameter at any axial point is related to the strength of the longitudinal electric field at that axial point (i.e., longitudinal with respect to the discharge). This relationship appears to be that the cross sectional area of the filament is proportional to the E-field strength. Increases in filament diameter are limited by a maximum diameter which is probably determined by the depth of penetration of the E-field (i.e. skin depth). When this maximum is exceeded, the filament splits into two shorter and thinner filaments. This phenomenon should be investigated in more detail.

7.3 Relationship of the Orientation of the Discharge to the EM fields

Contracted microwave discharges take an orientation such that the electric field sustaining the discharge is a longitudinal electric field with respect to the discharge. This is a consequence of the relative inability of a normal component of electric field to penetrate into the discharge (due to surface polarization). The basic arrangement of electromagnetic fields is: (1) a longitudinal field inside the discharge, (2) a radial component predominantly just outside the discharge, and

(3) a circumferential magnetic field around the filament. The microwave fields are tied to the orientation of the filament. When bouyancy or other forces cause a filamentary discharge to move around, it can be inferred that the microwave fields are also moving - maintaining the basic field structure in and around the discharge. Direct evidence supporting this contention is that whenever filaments were moving inside the microwave cavity, fluctuations in the cavity fields were observed (by the measure of E_{rw} and the impedance match) which were related to the motion of the discharges.

The field strengths and orientation around the surface wave discharges (Appendix A) support the above conclusion. Also, the close similarity of the surface wave fields with those of the TM_{01} plasma/waveguide mode (near the plasma) provides insight into the efficient coupling that often occurs between fast waves and surface waves. The problem of excitation of electromagnetic waves on a plasma column, including the phenomenon of one type of wave coupling to another type, should be investigated further.

7.4 Experimental and Diagnostic Methods

Using the microwave fields to both generate and diagnose the discharge is a useful, non-perturbing approach to the study of microwave discharges. Numerical solutions to Maxwell's equations may be required but do not represent a barrier due to the speed and availability of modern computers. The general diagnostic method is independent of the gas type, pressure or electron density regime of the discharges and thus makes it a versatile diagnostic technique for simple plasma geometries. However, the ultimate accuracy and limitations of this

technique should be investigated further. Specifically, the sensitivity of the characteristic equation to changes in ΔL, d_{ave}, E_{rw}, etc. should by investigated. Also, the effect of axial variations in a plasma/waveguide of the type encountered in this dissertation should be analyzed. Experimental results using this type of diagnostic technique should be compared with other diagnostic methods (such as a spectroscopic measure of electron density).

The study of microwave discharges from an EM point of view would eliminate some misunderstanding that currently exists in the literature on the type of traveling waves that are capable of sustaining a discharge. Specifically, the notion that a high frequency TEM wave can sustain a moderate density discharge on the axis of a hollow metal pipe [6,40] is clearly fallacious. Analytically, if the problem of a plasma on the axis of a metal pipe is set up as an EM boundary value problem, no roots of the transcendental equation would be found that correspond to a TEM wave unless the plasma were a perfect conductor. For the size of the metal pipes, frequency of excitation and expected electron density of the discharges in [6,40], only roots corresponding to surface waves are possible.

Thus, the overall approach to the study of microwave discharges described in this dissertation (both analytically and experimentally) is a necessary starting point in understanding the mechanisms of energy transfer to steady-state microwave discharges. Once an understanding is attained in simple plasma/EM field geometries, it then becomes easier to predict the behavior of similar discharges in other types of microwave excitation.

APPENDIX A

APPENDIX A

HIGH PRESSURE, MICROWAVE GENERATED STANDING SURFACE WAVE FILAMENTS

A-1 Introduction and Experimental Objectives

This appendix presents results of high pressure standing surface wave experiments in the heavy inert gases. The experiments were an extension of a low pressure standing surface wave investigation in argon gas [16]. A detailed description of the experimental system and general properties of microwave standing surface wave discharges is contained in reference [16] and will not be repeated here.

The main objectives of these high pressure experiments were to: (1) determine properties of high pressure inert gas filaments sustained by surface waves and (2) compare these discharges with the high pressure argon microwave discharges described previously in this dissertation. In this appendix, all references to sections, chapters or figures refer to those of this dissertation.

A-2 Experimental Description, Measurements and Analysis

The experiment consisted of two contracted surface wave plasmas generated in a common quartz tube using two surface wave launchers identical to the one pictured in Figure 2.3 and the one used in [16]. The operation of this launcher is described briefly in Section 2.4. Microwave power was generated by a filtered, 2.45 GHz, variable power source. The microwave power was split by a coaxial "Tee" and equal

amounts of power were delivered to each cavity. When sufficient power was added, the plasma columns became long enough to join together -- allowing the propagating surface waves from each cavity to interact forming standing surface waves.

Gas pressure ranged from 40-760 torr for these experiments. A 4.0 mm i.d. quartz tube oriented horizontally contained all discharges and gas flow rate was kept to near zero flow. Pressure was measured with a mercury manometer and the gases used were argon, krypton and xenon. Power absorbed to the discharge, P_p, was measured as the sum of the power absorbed by each cavity (coupling structure losses were neglected). Discharge diameters were measured photographically in the manner described in Section 3.4. A straight E-field probe and a shielded loop described in reference [16], were used to measure relative magnitudes of $|E_r|^2$ and $|H_\phi|^2$ axially along the plasma just outside the discharge tube.

Electron density was diagnosed by modeling the surface wave propagation along the filament in an analogous fashion as the method described in Section 5.3 for the plasma/cavity filaments. The axially and radially non-uniform plasma was approximated with an axially uniform, homogeneous, lossy dielectric rod with a diameter equal to the average diameter of the filament. Cold plasma theory was used to describe the electrical conductivity of the discharge. Figure 5.3 describes the cross section of the boundary value problem used for these surface wave discharges except that no metal waveguide was included. Because the discharge tube was oriented horizontally, the discharge in general floated up in the tube (off axis). This asymmetry was neglected in the electromagnetic analysis.

Equations 5.4, 5.5 and 5.6 remained valid for this analysis since

the desired solution was again a rotationally symmetric TM mode. Applying boundary conditions at the interfaces resulted in a transcendental equation relating the complex propagation constant β to the plasma dielectric constant -- and hence to electron density, N_e, and effective collision frequency, ν_e.

The formation of the standing surface wave allowed the determination of β_r in a similar way as in the cylindrical cavity experiments:

$$\beta_r = \frac{2\pi}{\lambda_g}$$

where λ_g was the experimental surface wavelength. Since the visible plasma diameter closely corresponded to the standing wave (as will be described in the next section), $\lambda_g/2$ was measured in the photographs as the distance between the two minimums in diameter. β_i was not measured, so that values of ν_e had to be assumed to determine N_e. The value of ν_e at any pressure was assumed to be approximately the value of ν_e determined by the argon cylindrical cavity experiments in the 4.0 mm tube (Figure 6.4). These values of ν_e should be a reasonable approximation for the argon surface wave results but may be less accurate for the results in krypton and xenon. By assuming values for ν_e, the characteristic equation reduced to one involving β_r (measured) and N_e (unknown). For each data point, the transcendental equation was solved numerically for N_e.

As in the analysis of Chapter V, N_e for these surface wave discharges represented a spatial average over radial and longitudinal variations in the plasma. The potential errors involved in determining N_e would be similar to those discussed in Section 5.7. The sensitivity of N_e to

changes in ν_e was investigated to evaluate the additional source of error by assuming values for ν_e. For values of ν_e up to three times those assumed for the analysis, N_e increased at most 30%. For values of ν_e as low as zero, N_e decreased a maximum of 20%. Thus, N_e was not particularly sensitive to changes in ν_e and any additional error introduced into N_e was probably not a large one.

A-3 General Discharge Characteristics, Power Density and Electron Density

The process of contraction in the surface wave discharges was similar to the description in Chapter IV for the argon cylindrical cavity filaments. The top of Figure A-1 displays the typical appearance of a standing surface wave filament. The visual appearance and light emission intensity of the argon discharges were similar to the argon cylindrical cavity filaments. Discharges in krypton were more purple in color and discharges in xenon were more blue. Also, emission intensity was visually less bright in these two gases than discharges in argon. Above 200 torr, discharges in krypton tended to branch out into several thin moving surface wave filaments, making it difficult to obtain a single standing wave filament. This was also observed in argon and xenon, but more infrequently.

Figure A-1 correlates the electromagnetic field patterns around a standing surface wave to the visual appearance of the discharge. These relationships were determined by the relative measure of $|E_r|^2$ and $|H_\phi|^2$ using the E-field probe and shielded loop. The location of maximum $|E_z|$ in the same region as maximum $|H_\phi|$ is characteristic of a standing TM type of wave as can be determined from Maxwell's equations. Thus, the dominant field component in terms of sustaining the plasma appears to be

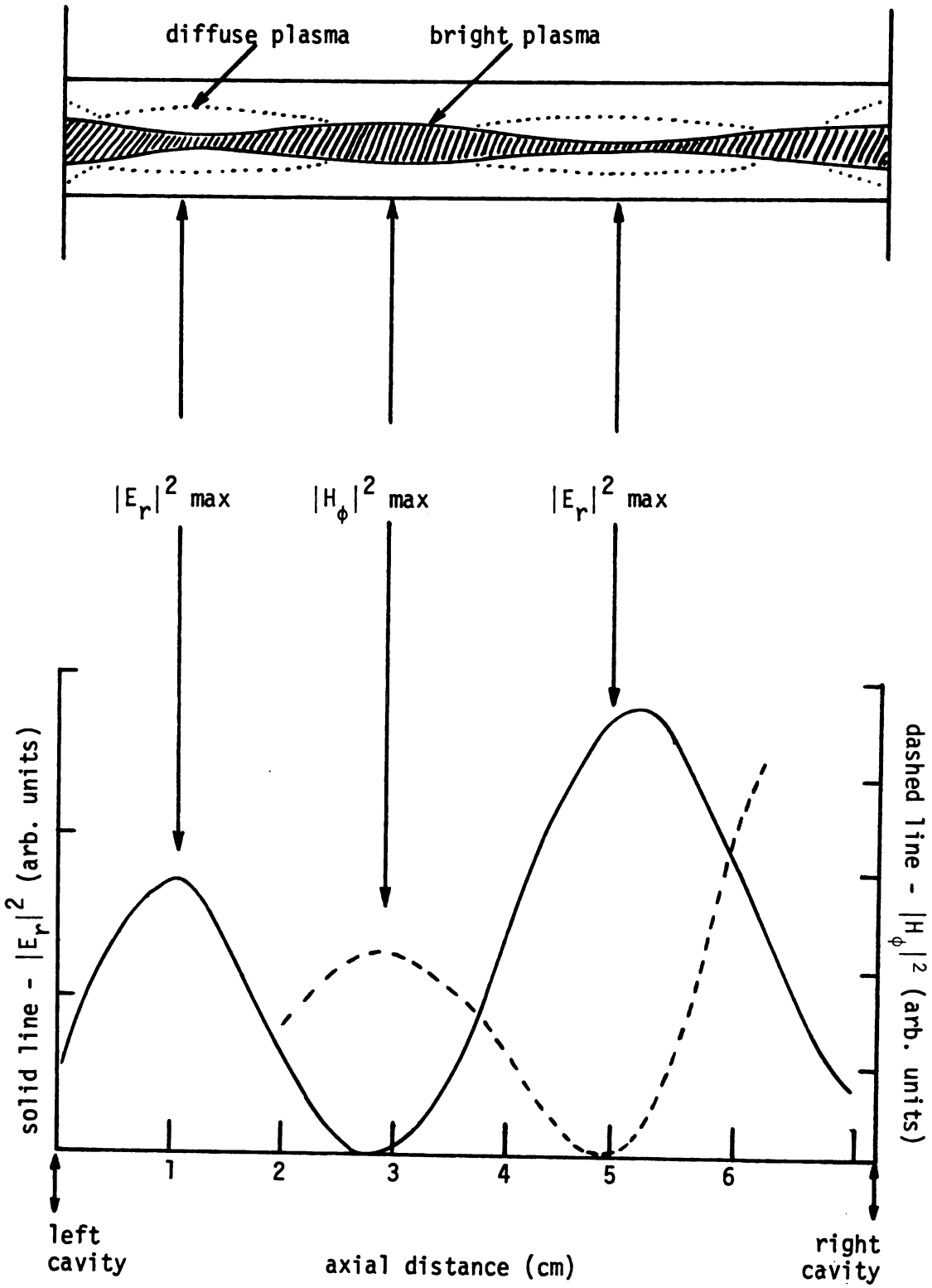

Figure A-1 Relationship of filament shape to measured axial distributions of $|E_r|^2$ and $|H_\phi|^2$ for an argon discharge at 146 torr.

$|E_z|$. Figure A-2 correlates the filament cross sectional area at any axial point with the computed value of $|E_z|$ at that point for an argon discharge at 114 torr. As in the cylindrical cavity filaments described in Chapter IV, the cross sectional area of the filament appeared to be proportional to the strength of $|E_z|$. Another similarity between the two types of microwave filaments is that in these surface wave discharges, regions of diffuse plasma generally appeared in regions of high $|E_r|$ as was observed in the cavity experiments. This effect is illustrated in the top of Figure A-1 by the dotted regions.

Figures A-3 and A-4 display power density, $\langle P \rangle$, and electron density, N_e, for the discharges in argon, krypton and xenon. At a constant pressure, there was little difference in N_e or $\langle P \rangle$ among the three gases. Changes in absorbed power at a constant pressure resulted in plasma volume increases with discharge properties remaining about constant. This behavior (investigated over a limited power range) was similar to the argon filaments generated in the cylindrical cavity. Figure A-5, which displays $\langle P \rangle$ and N_e with changes in absorbed power for argon discharges at 174 torr is representative of this behavior.

Figure A-6 compares $\langle P \rangle$ for these surface wave filaments in argon with $\langle P \rangle$ for the cylindrical cavity argon discharges generated in the 4.0 mm tube (data from Figure 4.10). These results compare well when considering the difference in discharge/tube geometry between the two cases. In the surface wave discharges, the tube was oriented horizontally and the filaments were displaced upwards in the tube (off axis). The degree of this displacement increased with pressure, being not apparant at 54 torr but very evident at 1 ATM. As can be seen from the figure,

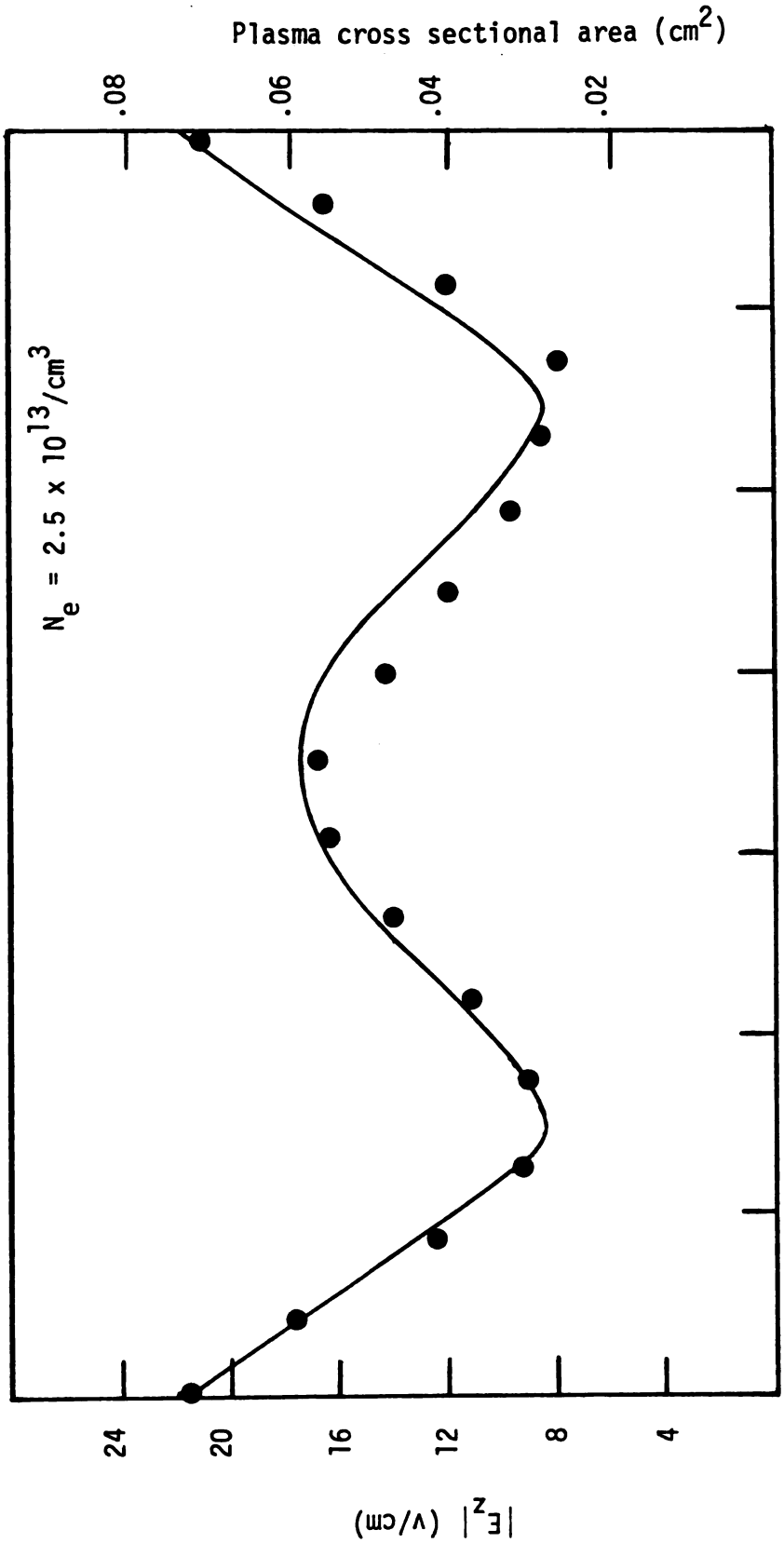

Figure A-2 Cross sectional area of the plasma filament compared to the computed axial distribution of $|E_z|$.

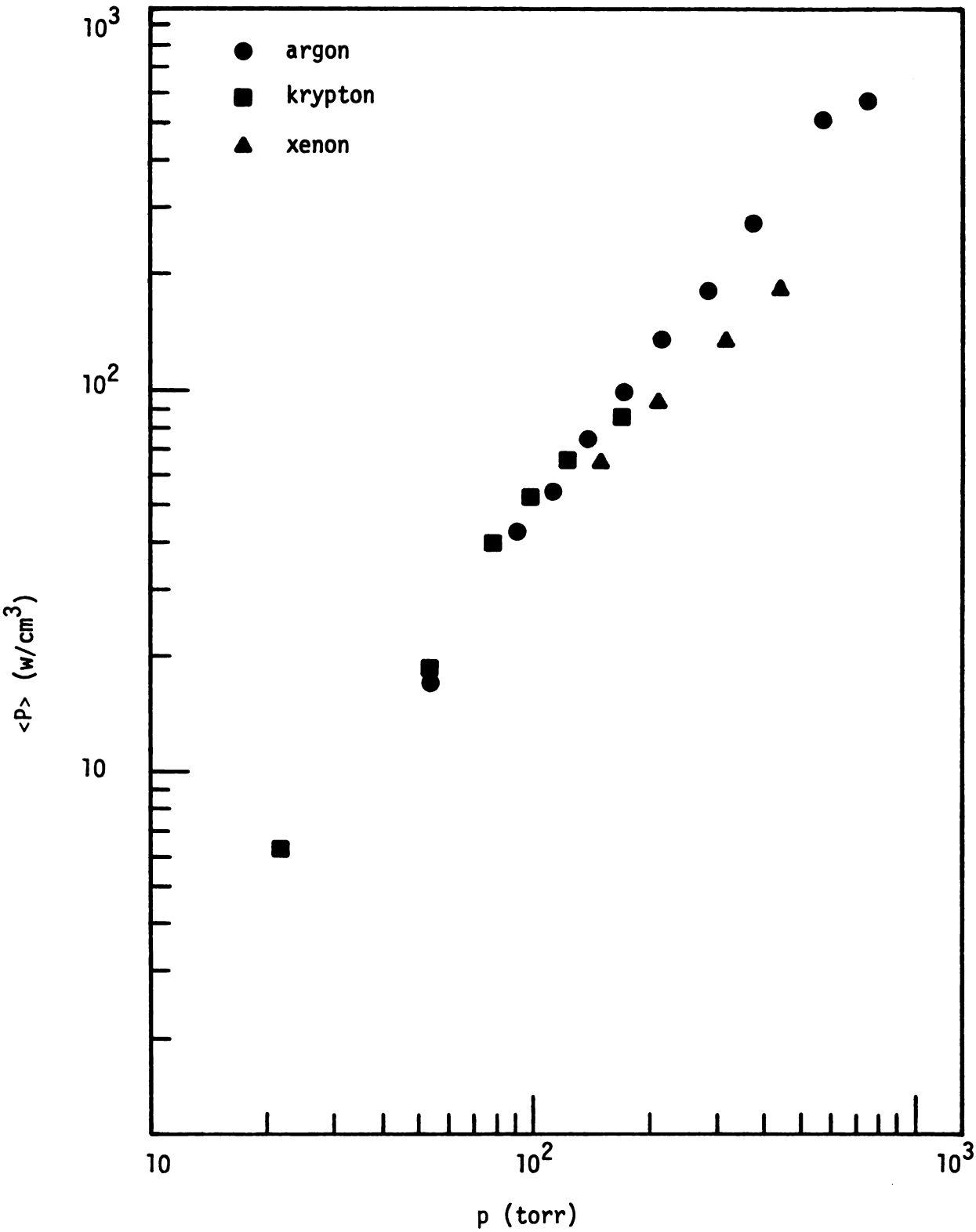

Figure A-3 Absorbed power density, <P>, versus pressure.

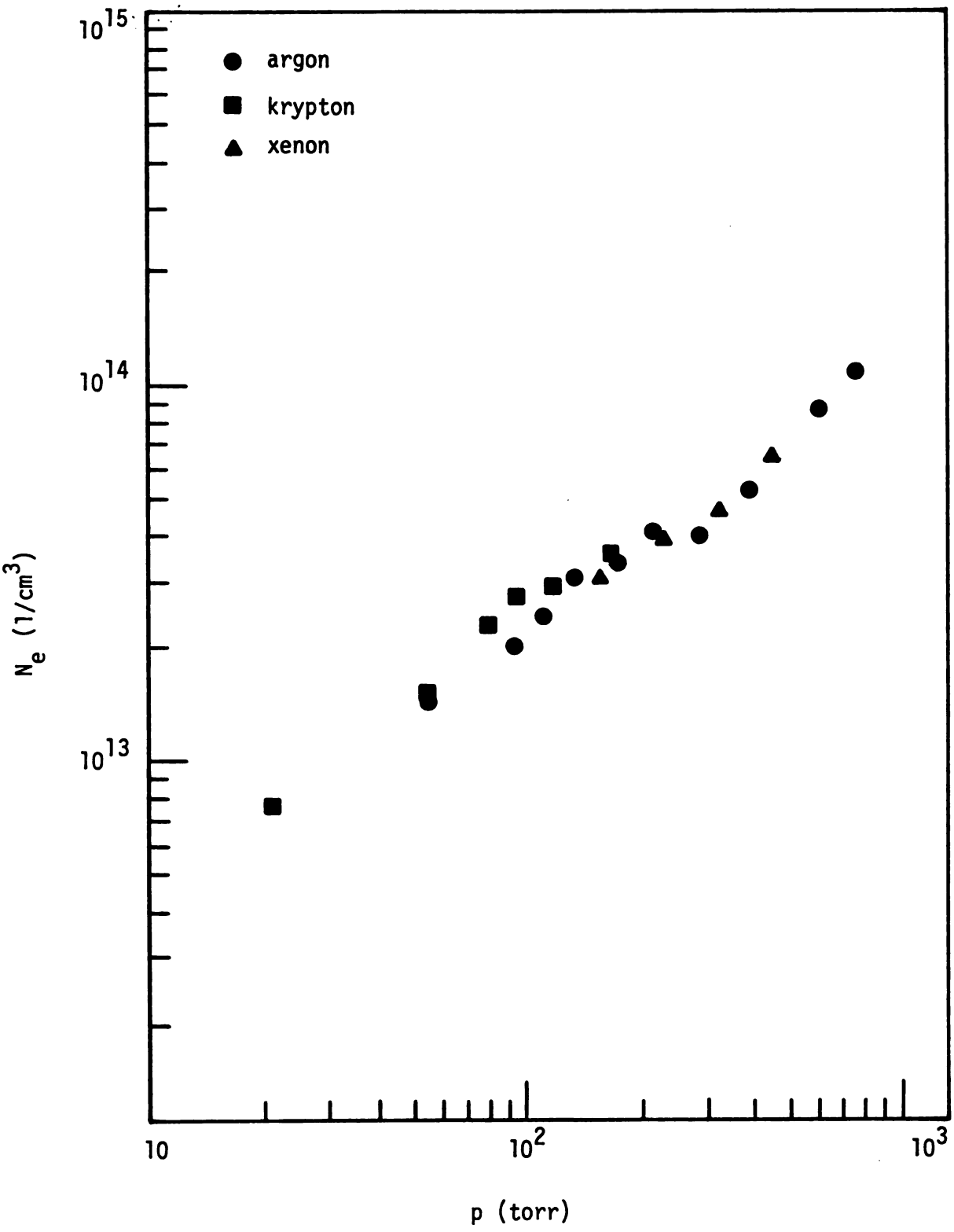

Figure A-4 Electron density, N_e, versus pressure.

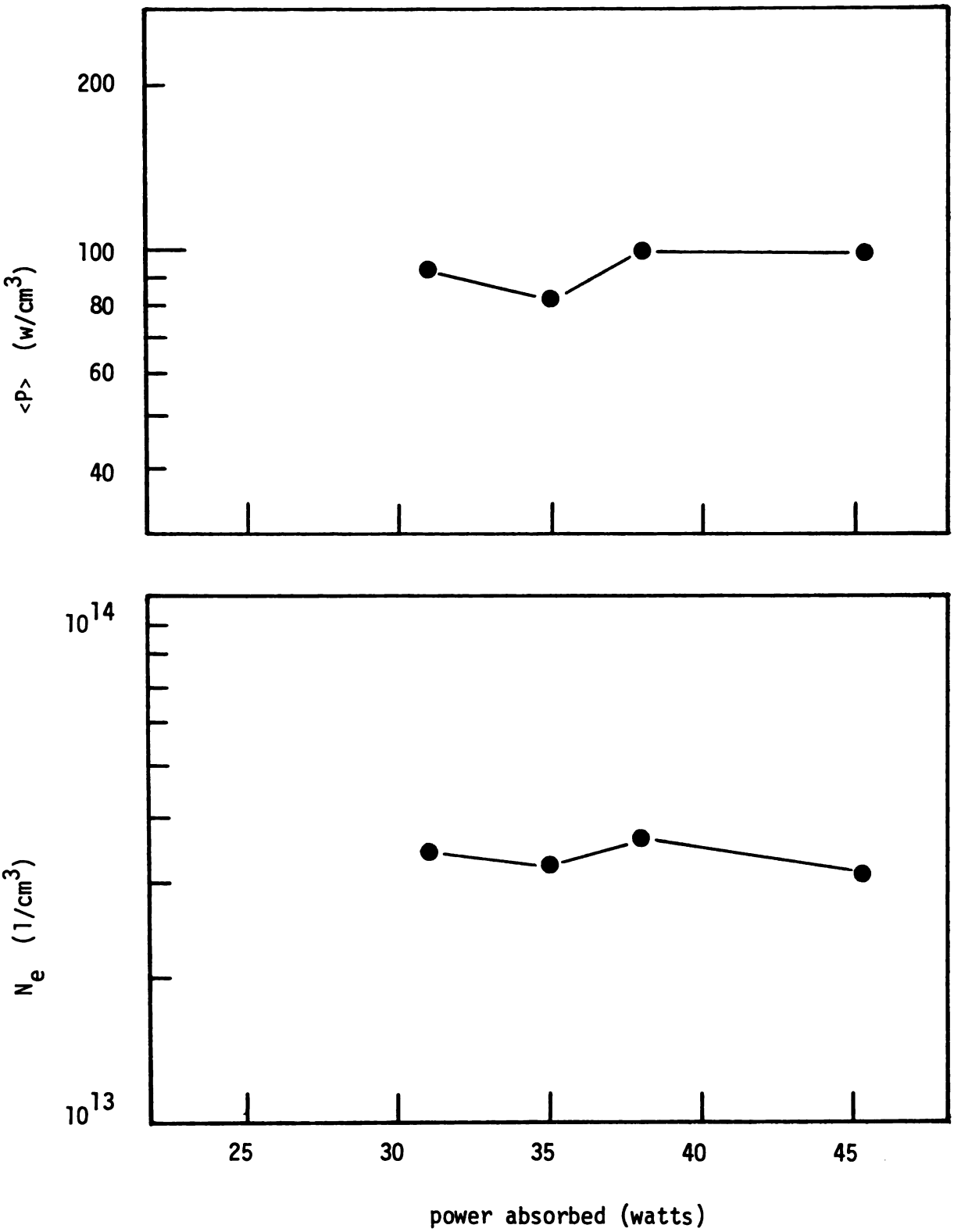

Figure A-5 Changes in <P> and N_e with changes in absorbed power for argon discharges at 174 torr.

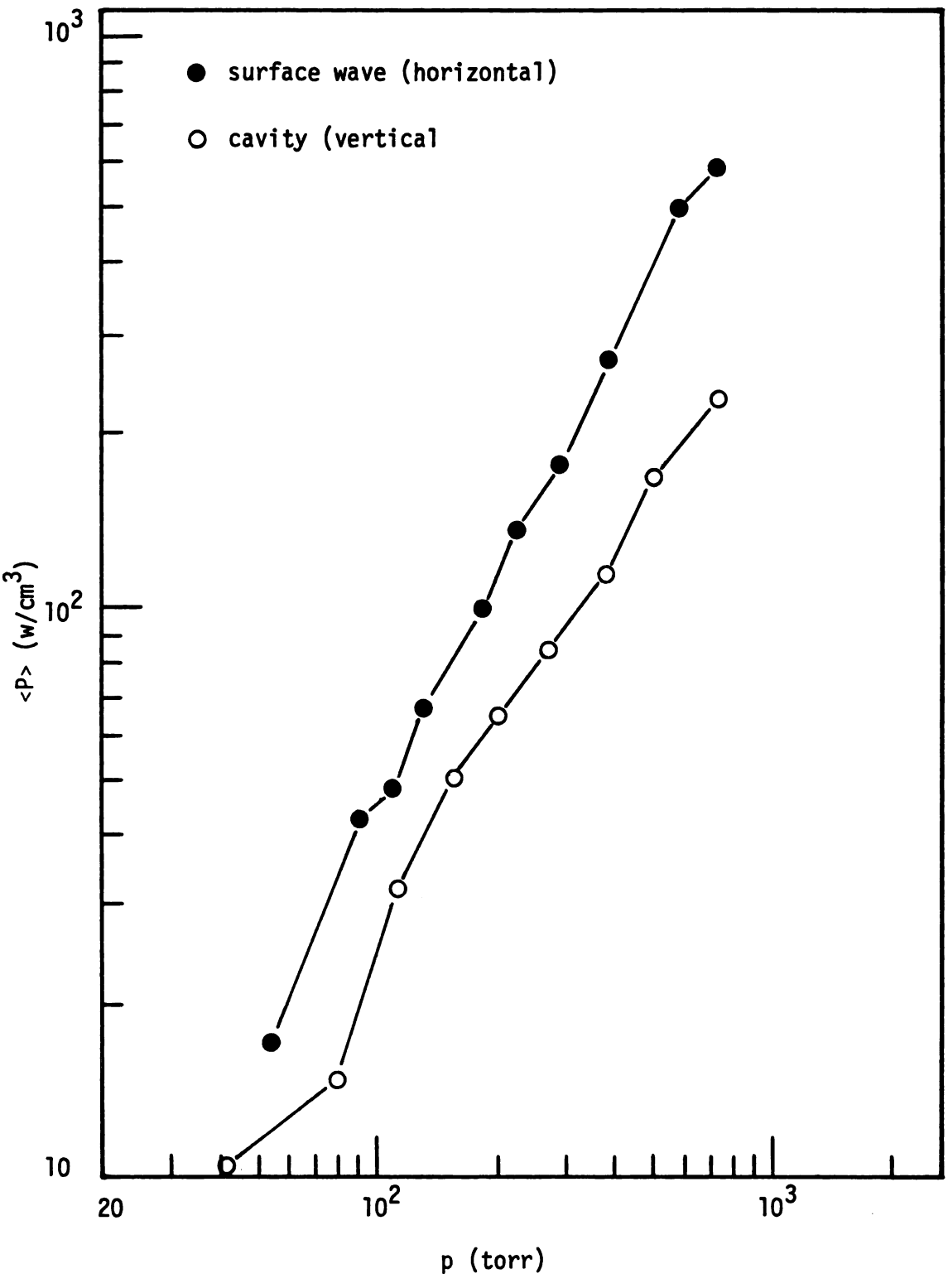

Figure A-6 Comparison of <P> for the argon surface wave discharges in a 4.0 mm tube horizontal to <P> for the argon cylindrical cavity discharges in a 4.0 mm tube vertical.

<P> was larger for the surface wave discharges as expected from the observations made in Chapter IV. N_e did not show such a clear difference - N_e for the surface wave discharges being about 50% lower than expected. This was attributed to the fact that the sampling region for determining N_e in the surface wave discharges did not include the most intense regions of the surface wave filament (near the cavity gaps) whereas the determination of <P> did include those regions.

A-4 Electric Field Distributions

Figure A-7 displays calculated cross sectional distributions of $|E_r(r)|$ and $|E_z(r)|$ for an argon discharge at 287 torr. A point of reminder is that the fields are rotationally symmetric and the particular cross section represents one at an average axial position in the standing wave. The field amplitudes were determined from <P>, N_e and ν_e assuming a uniform E-field across the plasma column. Several similarities exist in these distributions with those of Figure 6.6 (for a cylindrical cavity argon discharge at 265 torr). The relative distributions and field strengths inside the plasma are very similar. This was also true for $|H_\phi(r)|$ which was not displayed in either case. Also the relative strength and dependence of $|E_r(r)|$ just outside the plasma is similar in both cases.

The primary difference between the two types of microwave generated plasma columns is in the differences in field strengths and distributions outside the quartz tube. In the cylindrical cavity excitation (Figure 6.5), the field components increase with radial distance becoming similar to the TM_{01} empty waveguide field distributions. For the surface wave excitation (Figure A-7) the fields decrease with radial distance in an

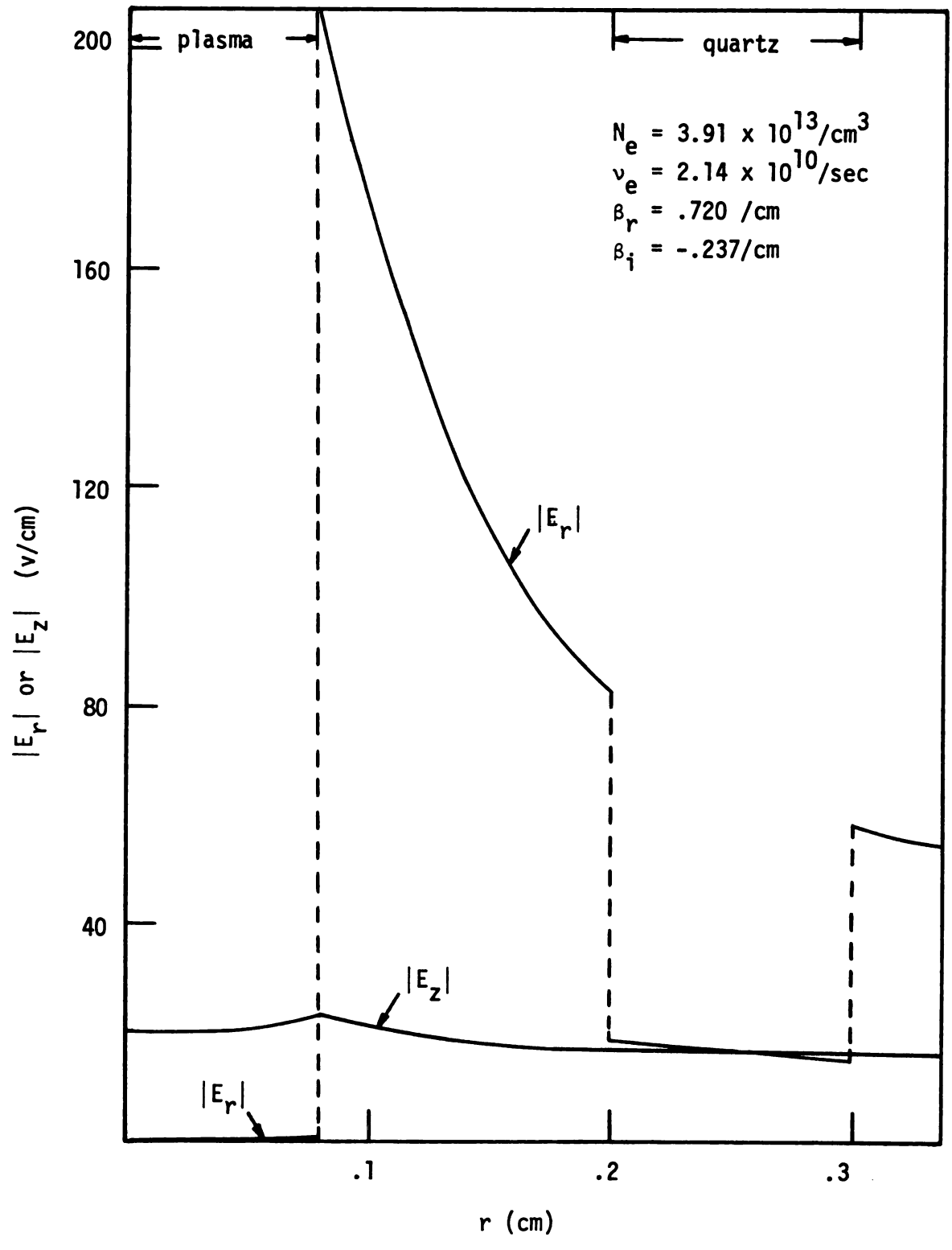

Figure A-7 Radial dependence of $|E_z(r)|$ and $|E_r(r)|$ for an argon discharge at 287 torr.

exponential like fashion. Thus, the amount of wave power carried exterior to the plasma by these types of traveling waves is strikingly different. (In terms of standing waves these differences would be in the stored energy of the fields). Correspondingly, the degree of coupling energy into the plasmas by the two cases also must be different since on a per unit length basis (for similar size and losses of the plasma), the amount of power transferred into each plasma would be the same. For the TM_{01} plasma/waveguide mode, the attenuation of the wave is very small (β_i = -.0057/cm for the case of Figure 6.5). For the TM, surface wave mode, the degree of attenuation is much higher (β_i = - .237/cm for the case of Figure A-7). Thus, a single traveling surface wave can sustain this type of plasma filament whereas in the TM_{01} plasma/waveguide mode, a resonant cavity is required (to essentially bounce the large amount of wave power back and forth in the cavity).

The effect of radial electron density variations on surface wave dispersion characteristics and the EM field distributions was investigated for a typical plasma filament (corresponding to the average diameter and properties of the argon surface wave discharge at 287 torr). Figure A-8 illustrates the two electron density profiles used in the comparison. The homogeneous case (Figure A-8a.) had an electron density equal to the average electron density over the cross section of the inhomogeneous case. An effective collision frequency of 2.14×10^{10}/sec was assumed for both cases. The particular profile in Figure A-8b was used because of its simple analytical formula and because it resembled measured electron density profiles in lower pressure argon contracted positive columns [39]. An integral operator approach developed by Sipe and Nyquist for heterogeneous surface waveguides [41] was used to formulate the radially

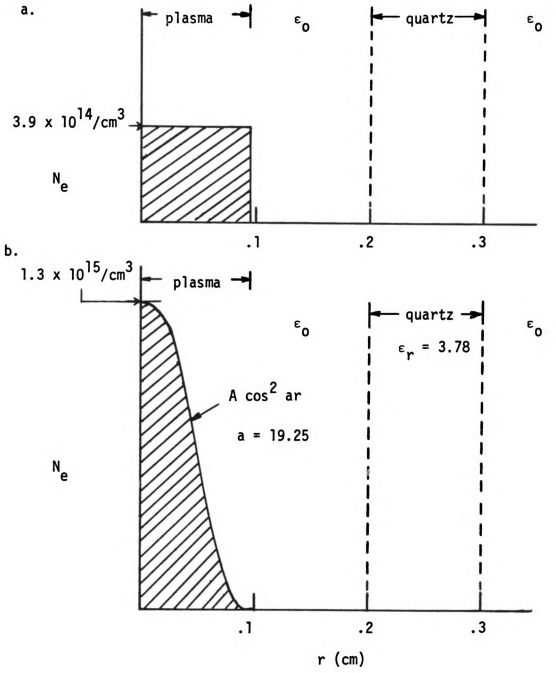

Figure A-8 The two radial density profiles used in the comparison of surface wave propagation along an inhomogeneous plasma filament to a homogeneous plasma.

inhomogeneous problem. This formulation allows for arbitrary variations in the radial profile of the waveguide dielectric constant, including jump discontinuities. A numerical moment method solution was used to solve for the complex propagation constant and the radial electric field distribution, $E_r(r)$. The axial field, $E_z(r)$, was determined from $E_r(r)$ using Maxwell's equations.

Figure A-9 compares $E_z(r)$ for the two cases and Figure A-10 compares $E_r(r)$. The amplitude and phase of $E_r(r)$ for the two cases were set equal to each other at the outside wall of the quartz tube. As can be seen from the figures, both amplitude and phase of the two field components were nearly the same for the two surface waveguides except near the plasma boundary where a large oscillation of the electric field of the inhomogeneous case was observed. The propagation constants for the two cases were also very close: $\beta = (.720 - j.237)$ /cm for the homogeneous case and $\beta = (.728 - j.218)$/cm for the inhomogeneous case. E_z was computed to be reasonably uniform over most of the plasma core in both cases.

A-5 Conclusions and Recommendations

For the same excitation frequency of 2.45 GHz the microwave surface wave discharges exhibited many similarities to the filaments generated in the cylindrical cavity. The conclusions in Chapter VII about properties of the cylindrical cavity filaments are supported by this investigation.

Calculated average electron density in these surface wave discharges appears to be insensitive to the radial electron density profile. Thus,

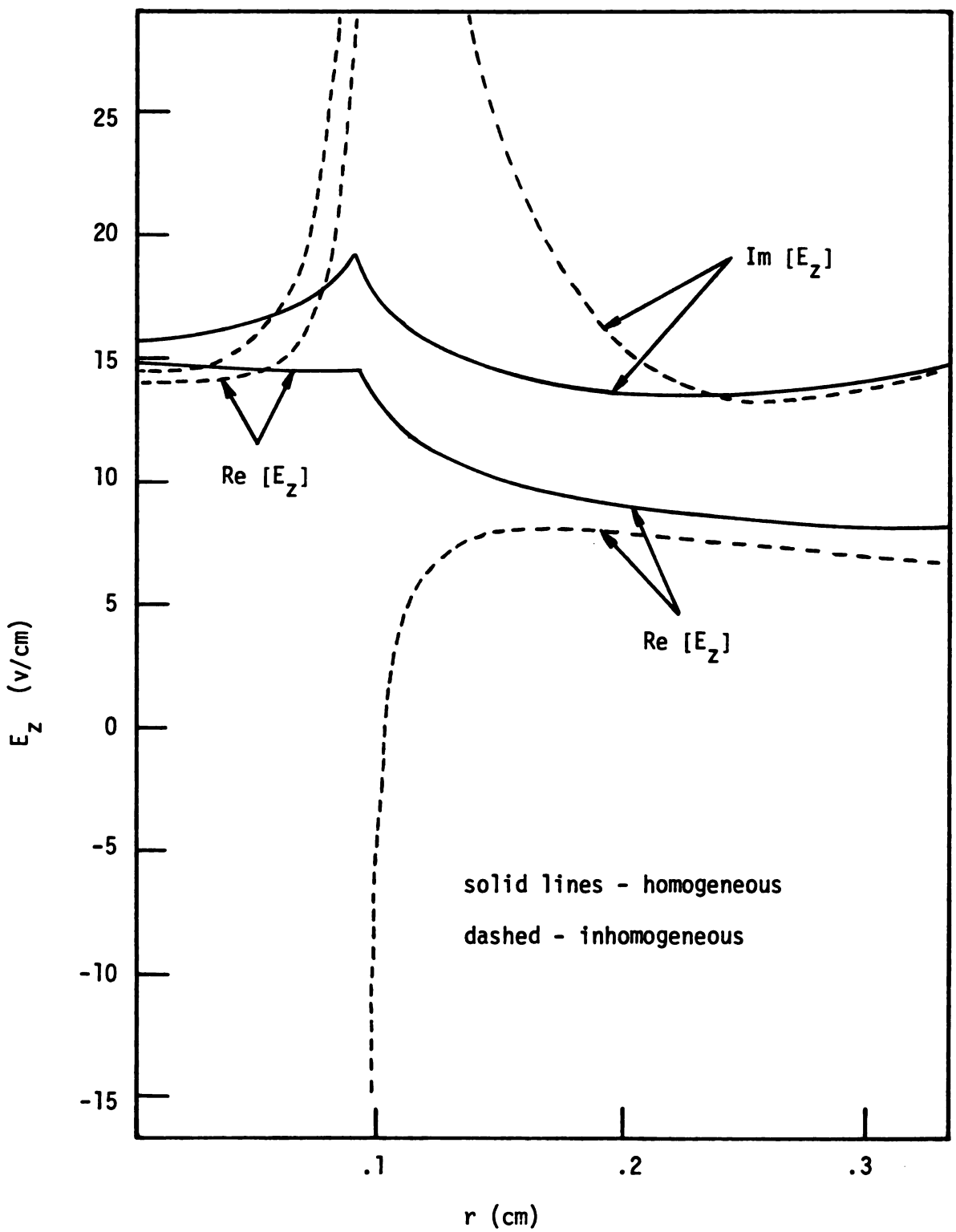

Figure A-9 $E_z(r)$ for the homogeneous and inhomogeneous cases.

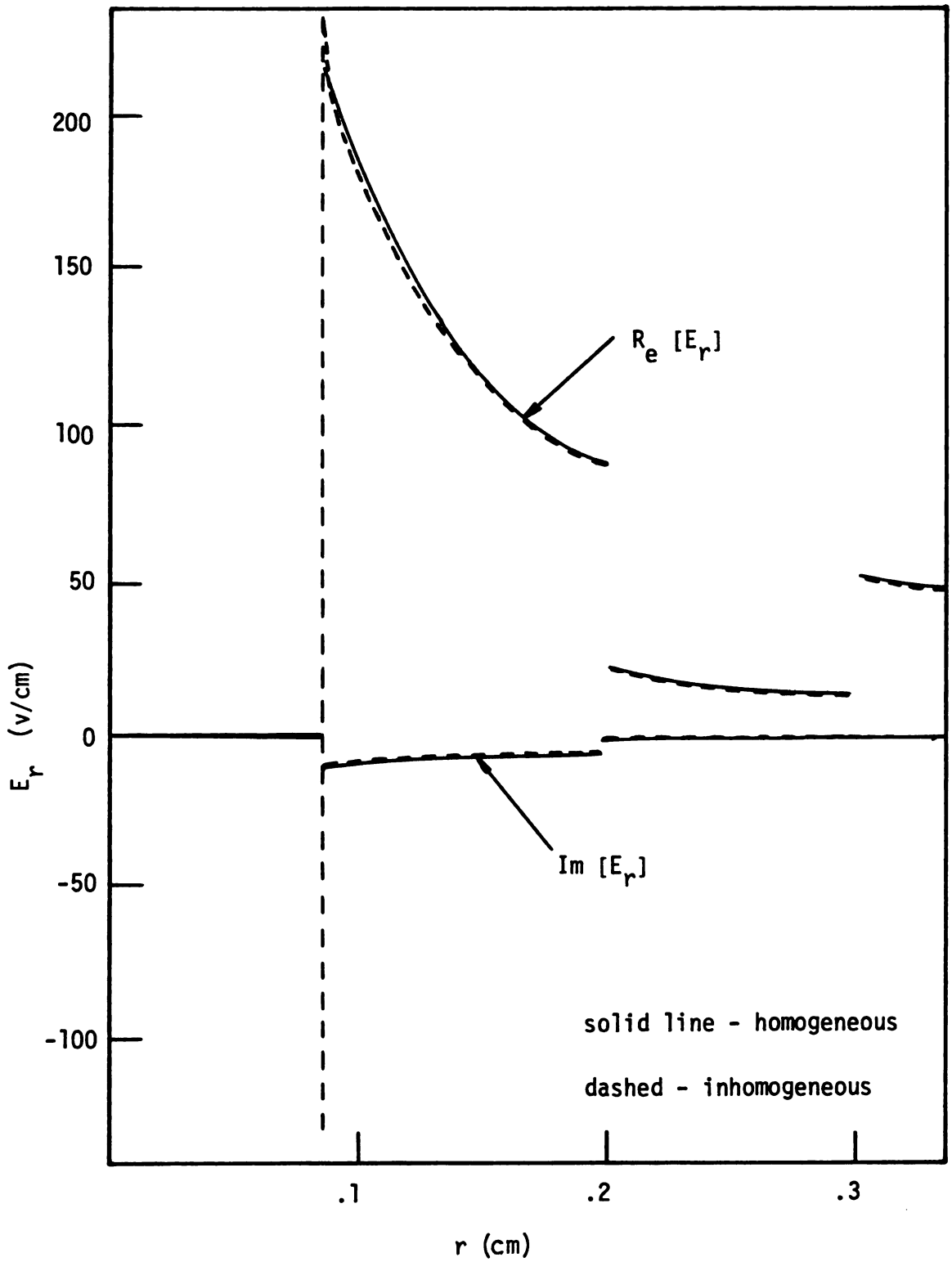

Figure A-10 $E_r(r)$ for the homogeneous and inhomogeneous cases.

the use of a homogeneous plasma model is adequate for diagnosing average discharge properties. Depending on the actual density profile, the peak electron density could be as high as three times the average density. Further experimental work should be done on determining actual electron density profiles. The integral operator technique [41] is a useful analytical tool for the radially inhomogeneous surface waveguides. The extension of this approach to handle a radially inhomogeneous plasma inside a cylindrical metal waveguide should be investigated.

Similar standing surface wave discharges in other gases should be investigated experimentally. Such experiments may require the construction of surface wave launchers capable of operating at high microwave power levels.

APPENDIX B

APPENDIX B

PROPERTIES OF STEADY-STATE, LOW PRESSURE ARGON MICROWAVE DISCHARGES

B-1 Introduction and Objectives

Low pressure argon microwave discharges were investigated using the experimental system and analysis described in the main body of this dissertation. In contrast to the high pressure filaments, these steady-state discharges filled the tube cross section. Electrons and ions were probably lost by diffusion to the quartz wall and subsequent recombination at the wall. The pressure regime of these experiments was .02 - 1.0 torr and quartz tubes of inner diameter up to 25 mm were used to contain the discharges. All experiments were carried out in the TM_{012} cavity mode using a filtered, variable power microwave source of frequency near 2.45 GHz.

The main objectives of these experiments were to:

1. determine properties of argon microwave discharges at pressures less than 1.0 torr for comparison with previous work on argon microwave discharges (using Langmuir probes as the diagnostic technique [16]) and for comparison with positive column theories [42,43]
2. determine the microwave field distributions in the plasma and cavity, and determine the effective electric field strength in low pressure argon microwave discharges
3. measure the dependence of microwave coupling efficiency (defined

in Section 5.2) as a function of pressure, electron density and discharge tube size.

Throughout this appendix, references to chapters, sections and figures refer to those of this dissertation.

B-2 Experimental Considerations

Differences in experimental techniques of these experiments from the high pressure cavity experiments will be described in this section. Figure B-1 illustrates the general appearance of the discharge in the TM_{012} cavity mode. Since the discharges appeared to fill the tube cross section, discharge diameters were assumed to be the inner diameter of the quartz tube. As in the high pressure experiments, the discharges were non-uniform both axially and radially as observed by variations in light emission. The radial electron density profile for a diffusion controlled discharge is theoretically expected to be proportional to J_o (2.405 r/a), where a is the plasma radius and J_o is the Bessel function of the first kind of order zero [31]. The axial non-uniformities in the discharges in most cases followed the axial standing wave of $|E_z|$, i.e. the most visually intense regions of plasma were located in regions of high $|E_z|$. An exception to this appearance will be described later. As in the high pressure experiments, the use of the homogeneous plasma model means that determined plasma properties are spatial averages over both axial and radial variations in the plasma.

Gas pressures were measured with Hastings vacuum tube gauges located at both ends of the quartz tube. Although only a slight amount of gas flow was present (to ensure purity of the gas), at pressures below .1 torr there was a small pressure drop down the tube which increased

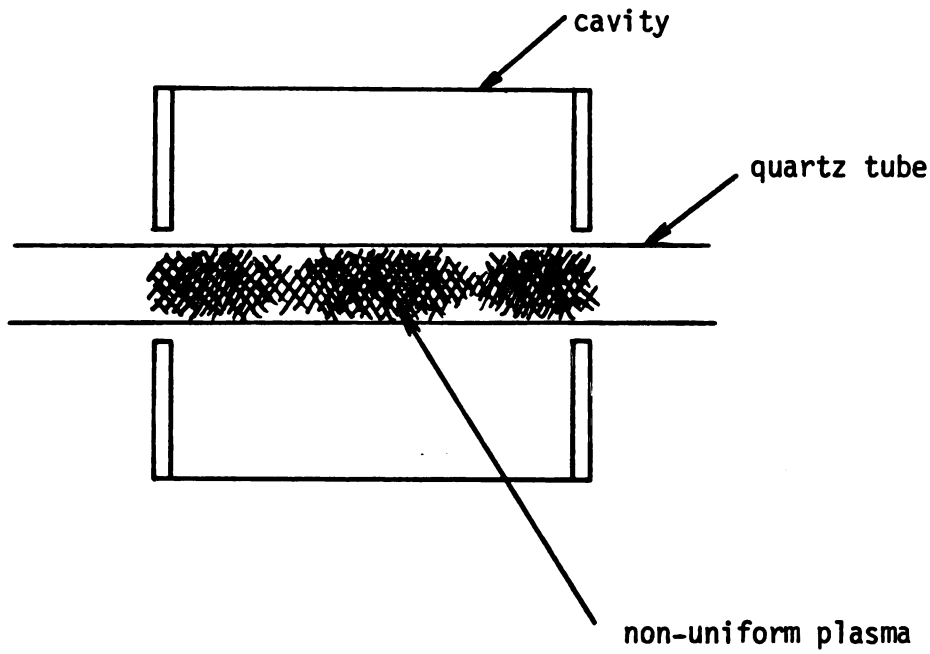

Figure B-1 General discharge appearance at low pressure in the TM_{012} mode.

with decreasing pressure. In these instances, gas pressure in the discharge was determined by assuming a linear pressure drop down the quartz tube. The results on these low pressure discharges were assumed to reflect properties of non-flowing discharges. However, this should be investigated further.

As can be seen from Figure 6.2 (for the high pressure argon filaments) gas temperatures appear to be approaching the quartz wall temperature in the pressure range of 1-10 torr. Thus, the gas temperature in these low pressure discharges was assumed to be at 300^{o} K for use in the calculation of electron temperatures. Because electron-ion recombination on the quartz wall can cause the wall to heat up significantly, external air cooling of the tube was essential for maintaining the wall near 300^{o} K.

As gas pressure is decreased, Q_u generally increases due to lower plasma losses. Higher values of Q_u for these low pressure experiments led to differences in the tuning process of the cavity from the high pressure experiments. When a low pressure plasma was present in the cavity, critical coupling was often not achieved in the TM_{012} mode. This was due to the discharge/circuit instability which can occur under high Q plasma/cavity operation [10]. Briefly, frequency drifts or imperfect filtering of the microwave signal can cause a momentary non-intersection of the plasma load line with the circuit resonance curve or can cause a shift to an unstable intersection point. When either happens, the plasma abruptly extinguishes. The lower the plasma losses (i.e. the higher the Q_u), the more likely this phenomenon occurs.

Figure B-2 illustrates an actual plasma load line and the approximate cavity resonance curves associated with each operating point. Although the proper way to display an intersection point on this type of curve is

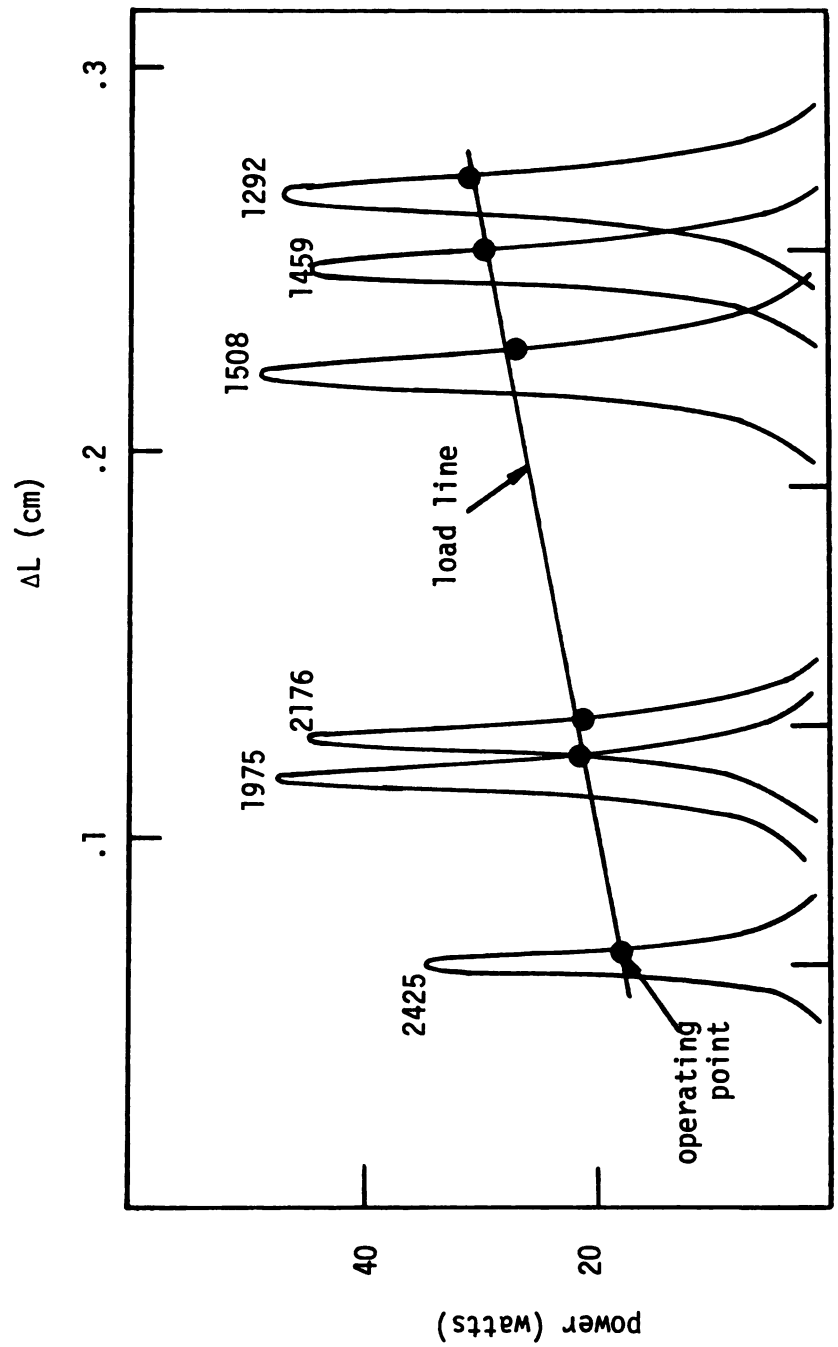

Figure B-2 Plasma load line and approximate cavity resonance curves for a constant length argon plasma in the 13 mm tube at .03 torr.

with a circuit resonance curve, Figure B-2 indicates the general graphical approach. In this pressure regime and for the relative size of the plasma to the cavity, there was nearly a linear relationship between cavity length shift and electron density. Thus, both quantities are displayed on the horizontal axis. The vertical axis represents power absorbed by the cavity (the height of the operating point) or incident power (the height of the resonance curve). The number above each curve is the measured Q_u at that operating point.

In each case illustrated in the figure, critical coupling could not be achieved since either reducing the power level or increasing the cavity length caused the plasma to abruptly extinguish. As the electron density increased (i.e. Q_u decreased), the ability to match power into the cavity improved. For Q_u less than 1000, the cavity could be nearly critically coupled (often less than 1% of the incident power was reflected). As Q_u increased above 1000, the ability to match power into the cavity declined rapidly. Although the plasma/cavity could not be critically coupled when $Q_u > 1000$, a significant error was not introduced into the results because the resonance curves were so narrow compared to the cavity length shift.

B-3 Comparison of Discharge Properties in Different Tube Sizes

A series of data points was taken in three different sizes of quartz tubes (4.0, 7.0 and 13 mm i.d.) with the plasma length always approximately 16 cm as indicated in Figure B-1. Absorbed power was adjusted to be roughly the same in all tubes at a constant pressure so that differences in discharge properties could be attributed to the different tube diameters. Figure B-3 displays the absorbed power in the plasma

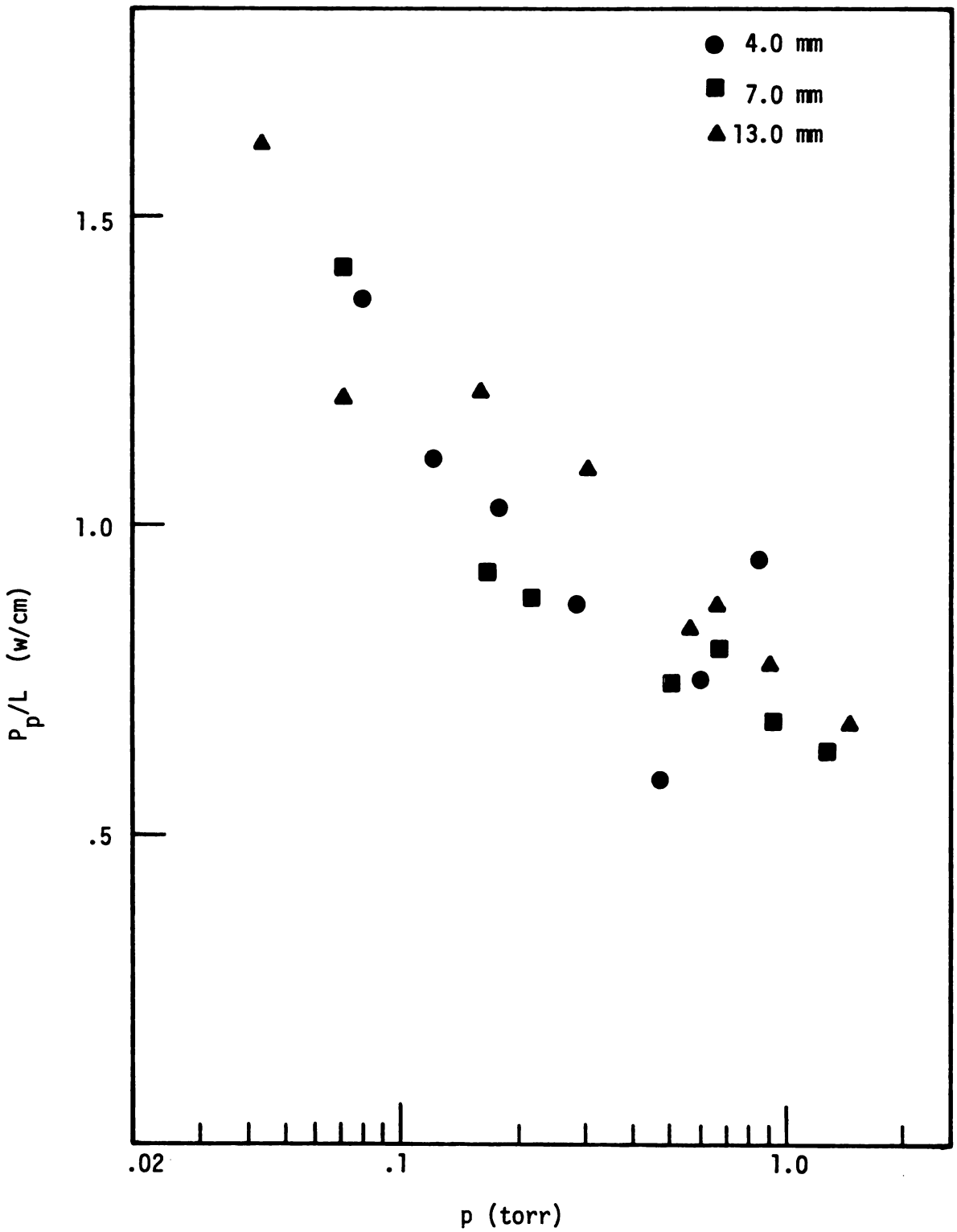

Figure B-3 Absorbed power per unit length (P_p/L) versus tube size and pressure.

per unit length (P_p/L) for the data in the three tubes.

As the quartz tube diameter decreased, absorbed power density, <P>, and electron density, N_e, both increased at a constant pressure. These results are shown in Figures B-4 and B-5. Q_u, however, changed relatively little in the three tubes at a constant pressure as shown in Figure B-6. These values of Q_u indicate that microwave coupling efficiencies generally decreased with pressure from about 99% at 1.0 torr to about 85% at .04 torr. Coupling efficiencies will be examined in more detail in the next section.

Figure B-7 displays effective collision frequency, ν_e, as a function of pressure for the three tube sizes. In general, ν_e appeared to be independent of the tube size and appeared to decrease nearly linearly with pressure. Data points in the 4.0 mm tube below .2 torr, however, deviated from the above generalization. These values of ν_e (which were experimentally repeatable) were about 2-3 times higher than values of ν_e in the larger tubes at the same pressure. Figure B-8 displays electron temperatures, T_e, calculated from ν_e as a function of the reduced pressure-discharge radius product, p_oR. Except for the four data points in the 4.0 mm tube below .2 torr, there was good agreement as to both order of magnitude and the general pressure dependence of T_e with positive column theories [42,43]. For the p_oR range of .08 - 1.0 torr-cm, there was especially good agreement with the Langmuir probe data taken on microwave generated argon surface wave discharges [16]. Both sets of data (using different types of diagnostic techniques) indicate a flat pressure dependence of T_e in that p_oR range with values between 25,000^o K and 30,000^o K.

The four data points in the 4.0 mm tube below .2 torr corresponded

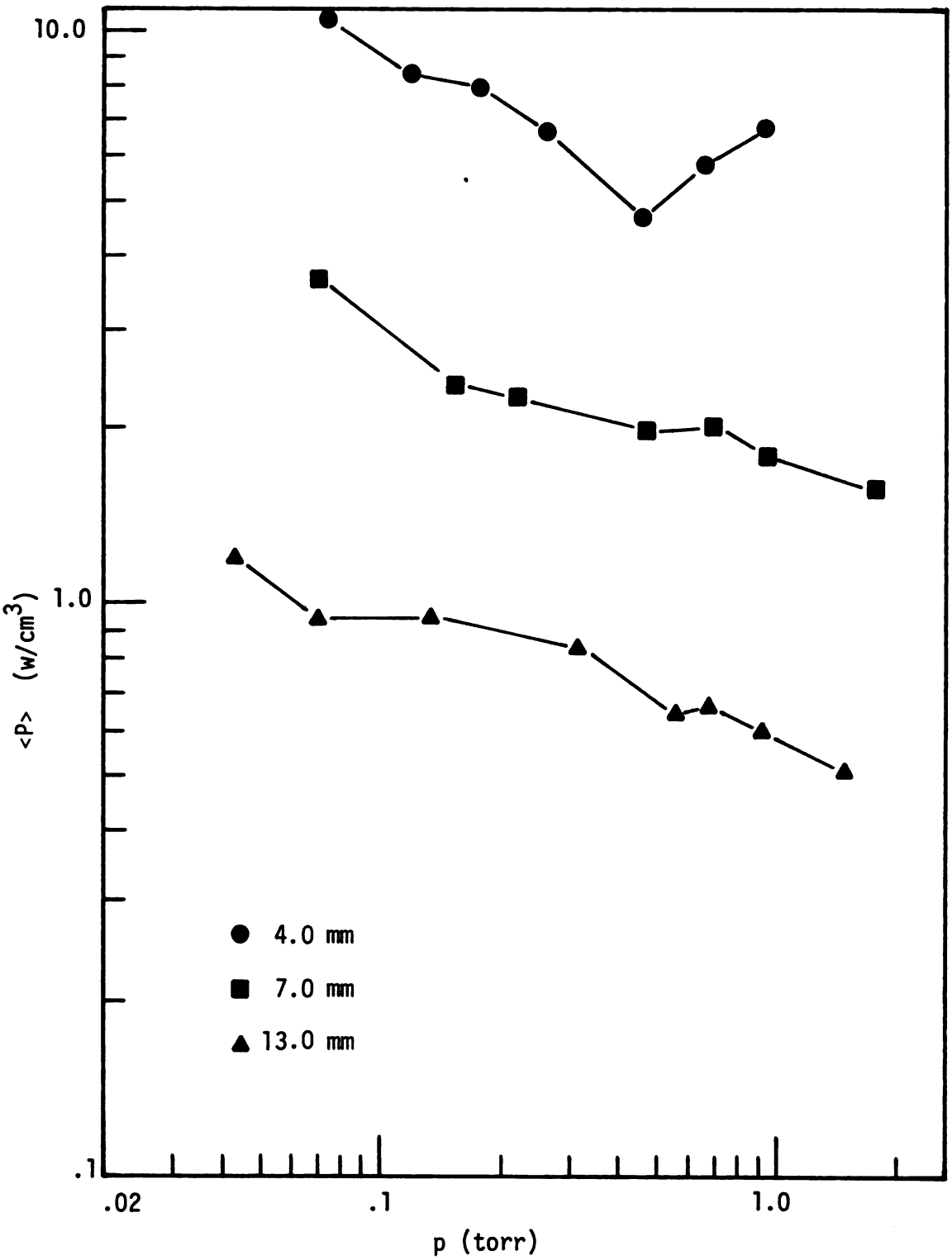

Figure B-4 Absorbed power density, <P>, versus pressure and tube size.

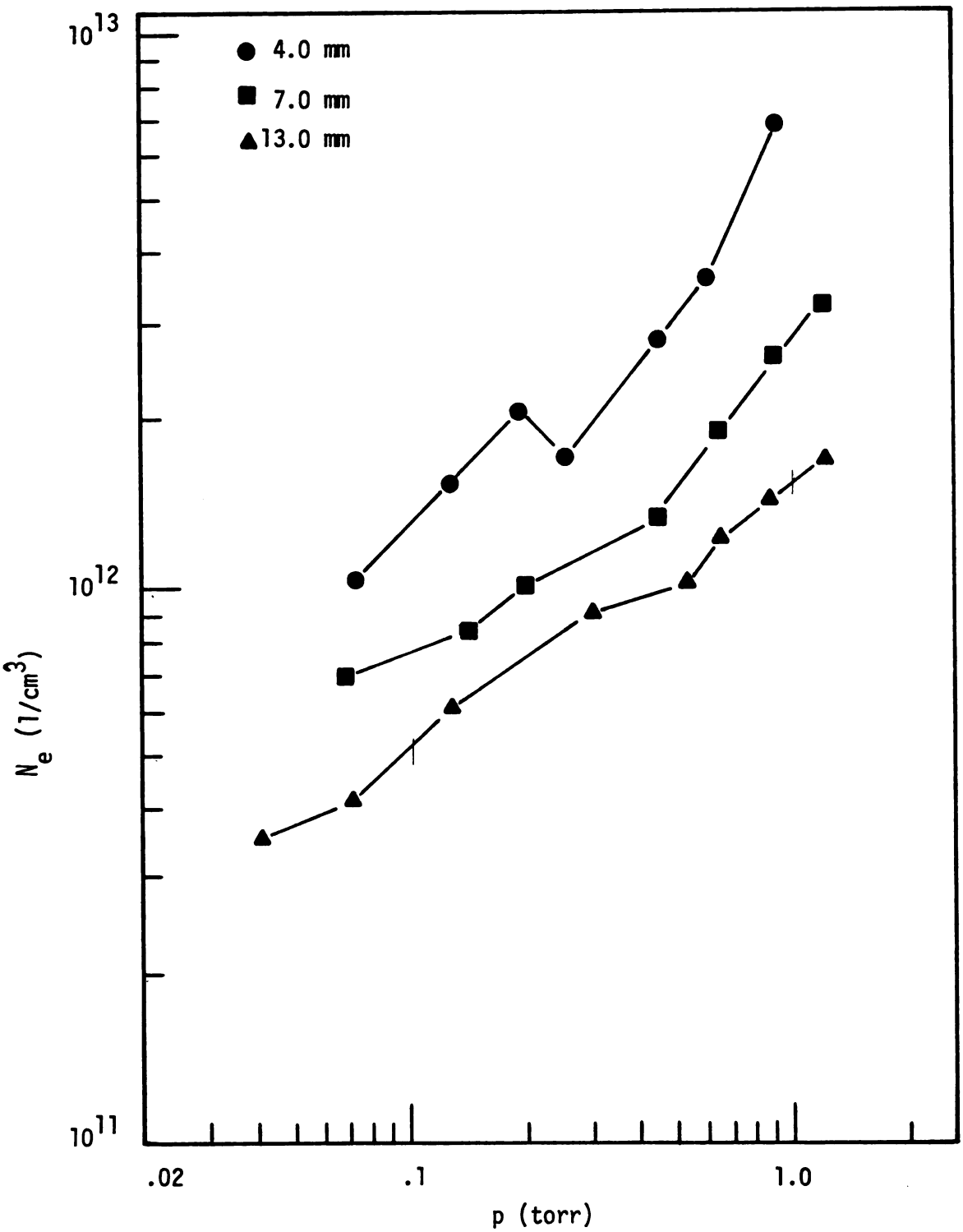

Figure B-5 Electron density, N_e, versus pressure and tube size.

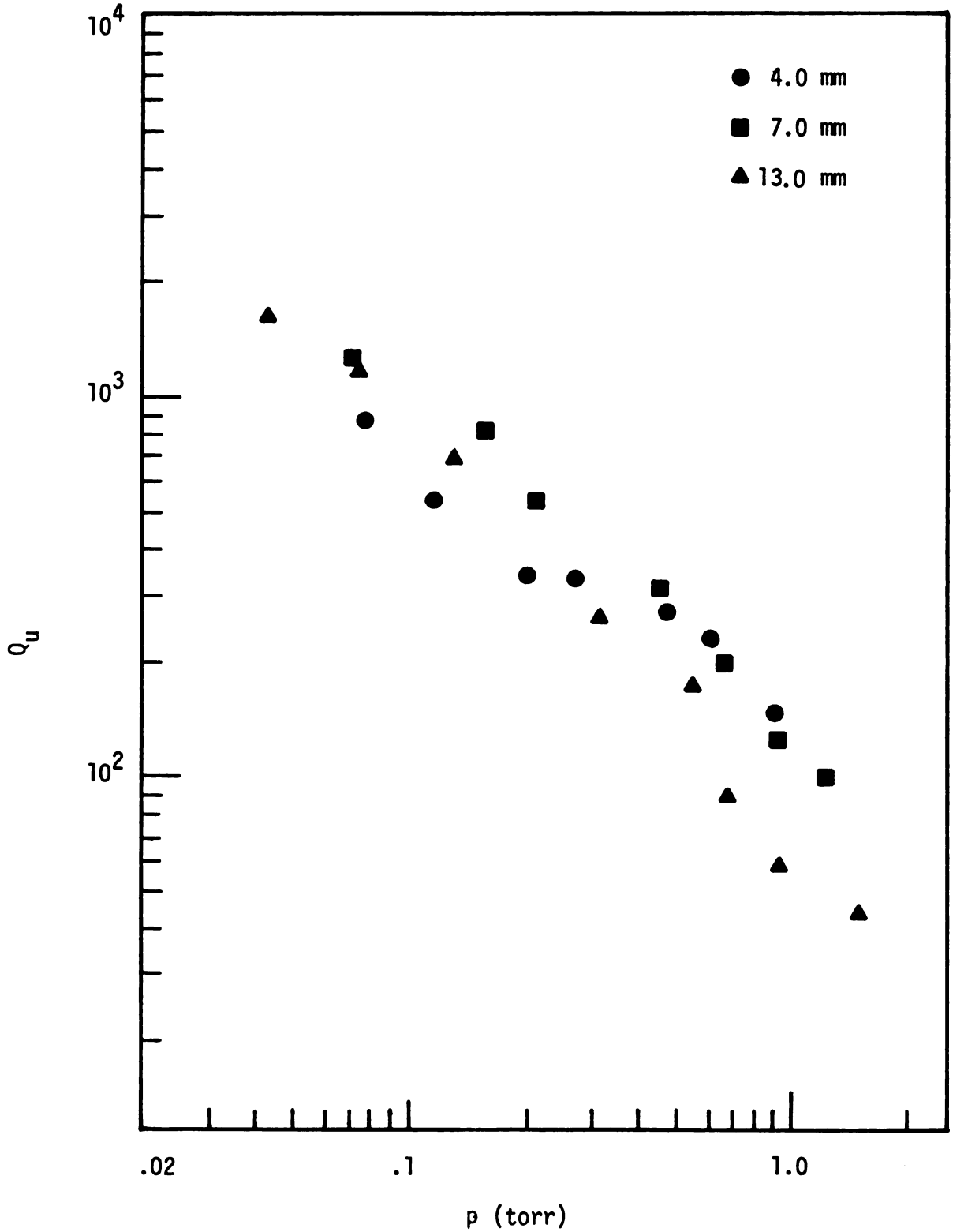

Figure B-6 Unloaded cavity Q, Q_u, versus pressure and tube size.

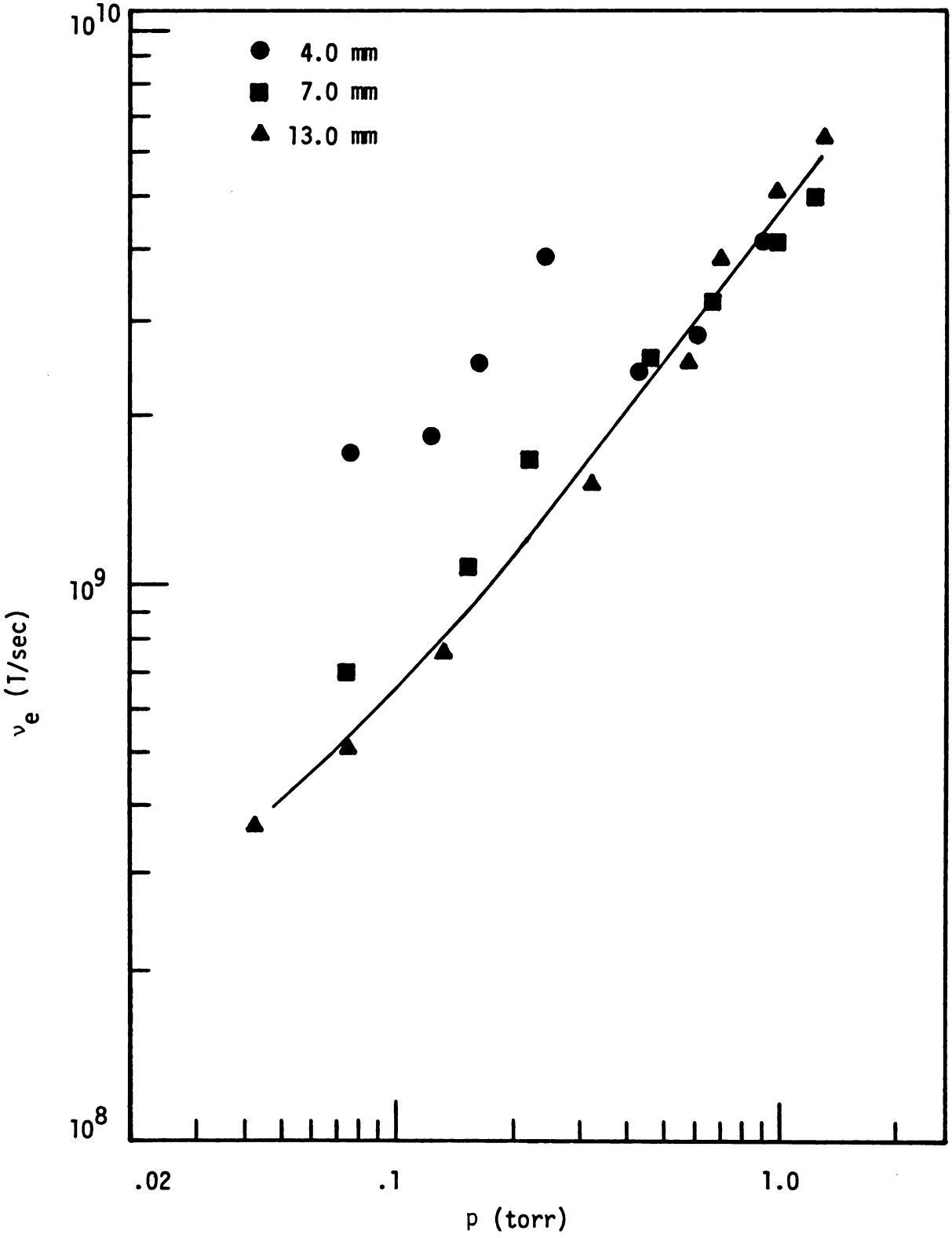

Figure B-7 Effective collision frequency, ν_e, versus pressure and tube size.

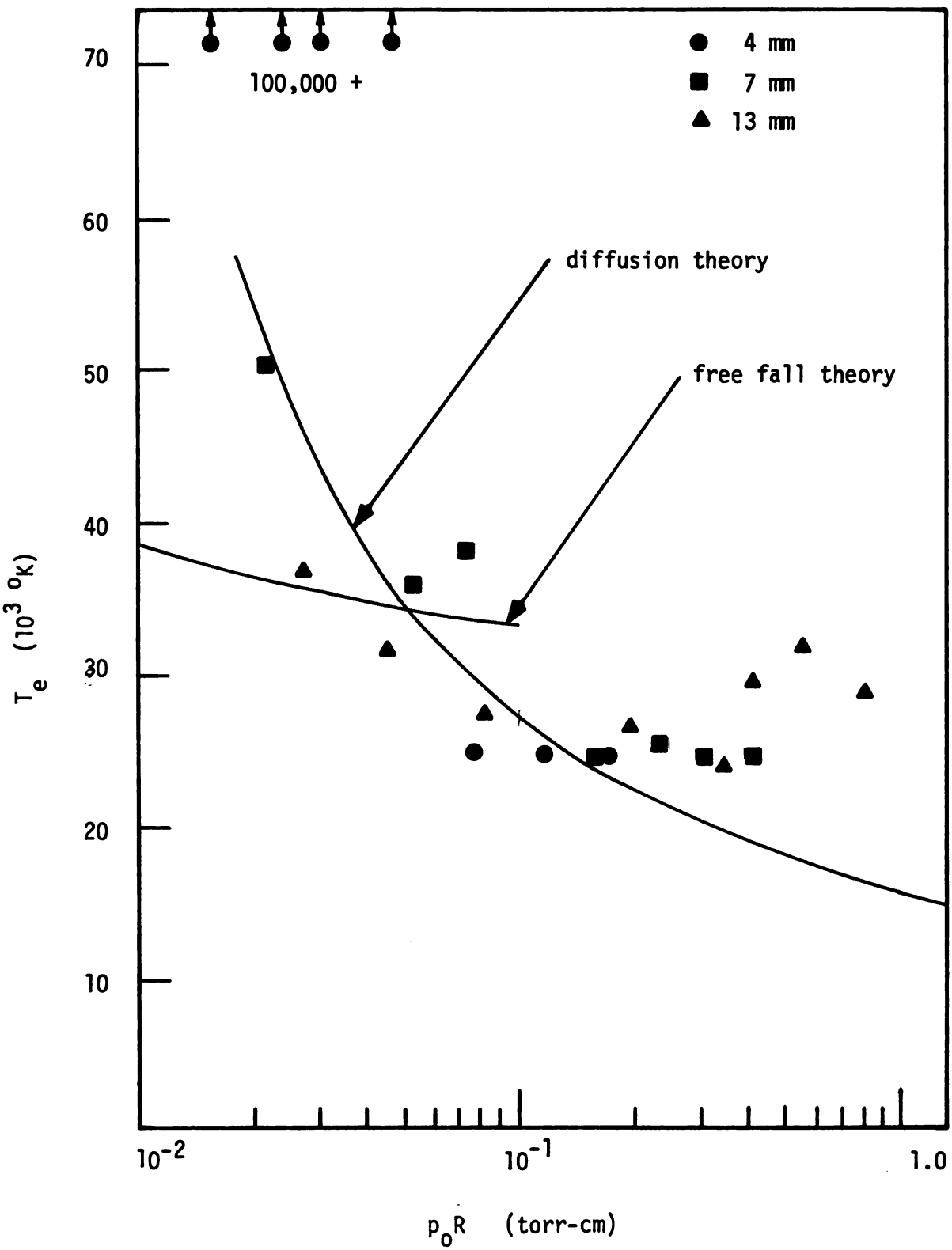

Figure B-8 Electron temperature, T_e, versus p_oR and tube size.

to improbably high values of T_e ($\geq 10^5$ ^oK) when compared with the Langmuir probe data in [16]. These unexpected results could have been due to: (1) space charge sheaths or some other phenomenon causing elevated electron temperatures [43], (2) large deviations in the velocity distribution function from the Maxwellian distribution, and/or (3) heating mechanisms other than electron-neutral collisions.

Microwave electric field strengths in the discharges behaved similarly with pressure in all three tubes. E_p (the spatially averaged, peak absolute value microwave field strength defined in Section 5.3) increased from 10-20 v/cm at 1.0 torr to 90-100 v/cm at .07 torr. Typical cross sectional distributions of $|E_r(r)|$ and $|E_z(r)|$ for a .04 torr discharge in the 13 mm tube are displayed in Figure B-9. As in the results of Chapter VI, this cross section represents the average axial point in the standing wave of the TM_{012} mode. A difference in these low pressure E-field distributions is that $|E_r(r)|$ near the plasma boundary was relatively low for these low pressure results.

Effective electric field strengths, E_e, of the discharges were relatively constant with pressure in each tube size. Over the pressure range of .04 - 1.0 torr, E_e varied from 2.0 - 2.8 v/cm in the 13 mm tube, 3.0 - 3.8 v/cm in the 7 mm tube and 3.8 - 8.0 v/cm in the 4.0 mm tube. Figure B-10 displays $E_e/(p_oR)$ versus p_oR for the data in all three tubes.

B-4 Microwave Coupling Efficiency

The definition of microwave coupling efficiency was given in Section 5.2 and is restated here for convenience:

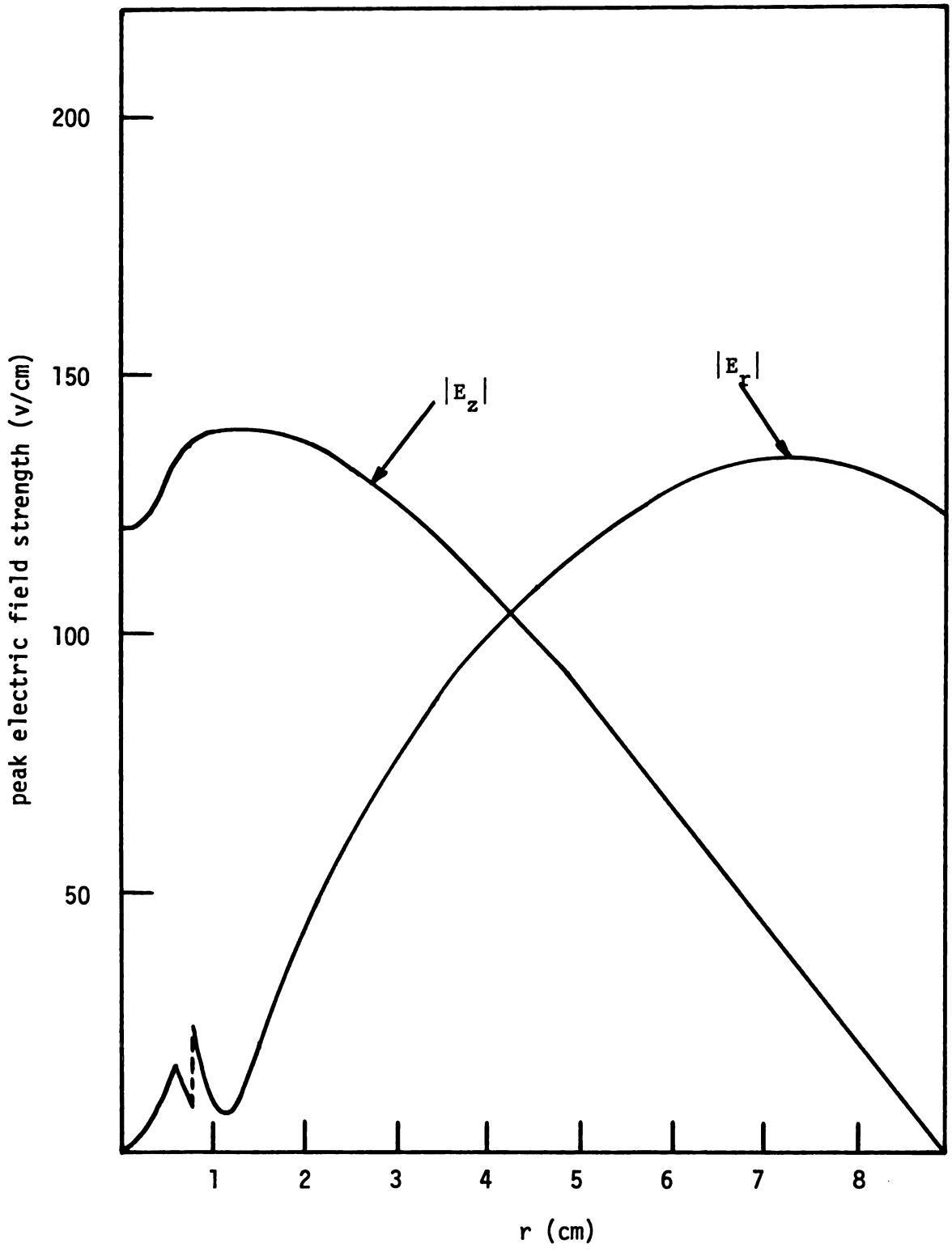

Figure B-9 Radial dependence of $|E_z(r)|$ and $|E_r(r)|$ for an argon discharge at .04 torr in the 13 mm tube.

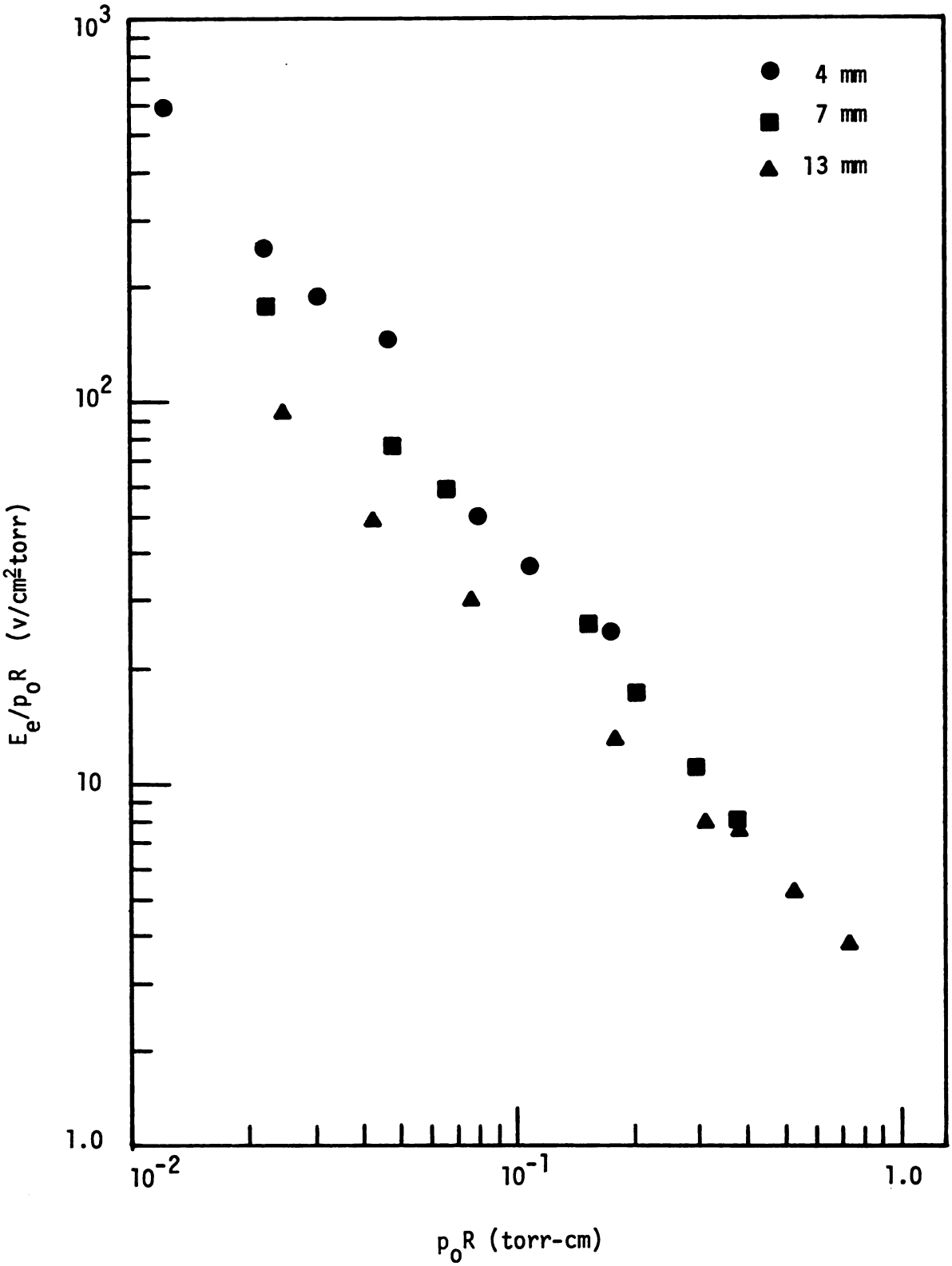

Figure B-10 E_e/p_oR versus p_oR

$$\text{Eff} = 100\% \times \frac{\text{Power absorbed in the plasma}}{\text{Total power absorbed in the cavity}}$$

Figure B-11 displays values of Eff versus pressure for discharges in the 13 mm tube having different values of P_p/L at a constant pressure (but all having the same discharge length pictured in Figure B-1). In general, Eff decreased with pressure as described in Section B-3. At a constant pressure, Eff was higher in discharges having a higher electron density. This variation of Eff with N_e was investigated carefully at a pressure of .03 torr in the 13 mm tube. Figure B-12 displays Eff and N_e as a function of power absorbed in the plasma. Except for the data point at the lowest P_p, there appeared to be roughly a linear dependence of Eff with N_e. This was a consequence of other discharge properties and the wall electric field measurement (E_{rw}) remaining approximately constant for all data points except the one at the lowest P_p:

$$T_e \cong 50{,}000\ ^{o}K$$
$$\nu_e \cong 3.2 \times 10^{8}/\text{sec}$$
$$E_p \cong 120\ \text{v/cm}$$
$$E_{rw} \cong 120\ \text{v/cm}$$

The data point in Figure B-12 at the lowest value of P_p produced an unexpectedly high efficiency which was repeatable. For an average density of approximately $8 \times 10^{10}/\text{cm}^3$ (close to $\omega_p = \omega$), Eff was 90% --significantly higher than would be expected by observing the dependence of Eff with N_e for the other data points. E_{rw} for this case was 60 v/cm, resulting in coupling structure losses of about 1/4 of those of the

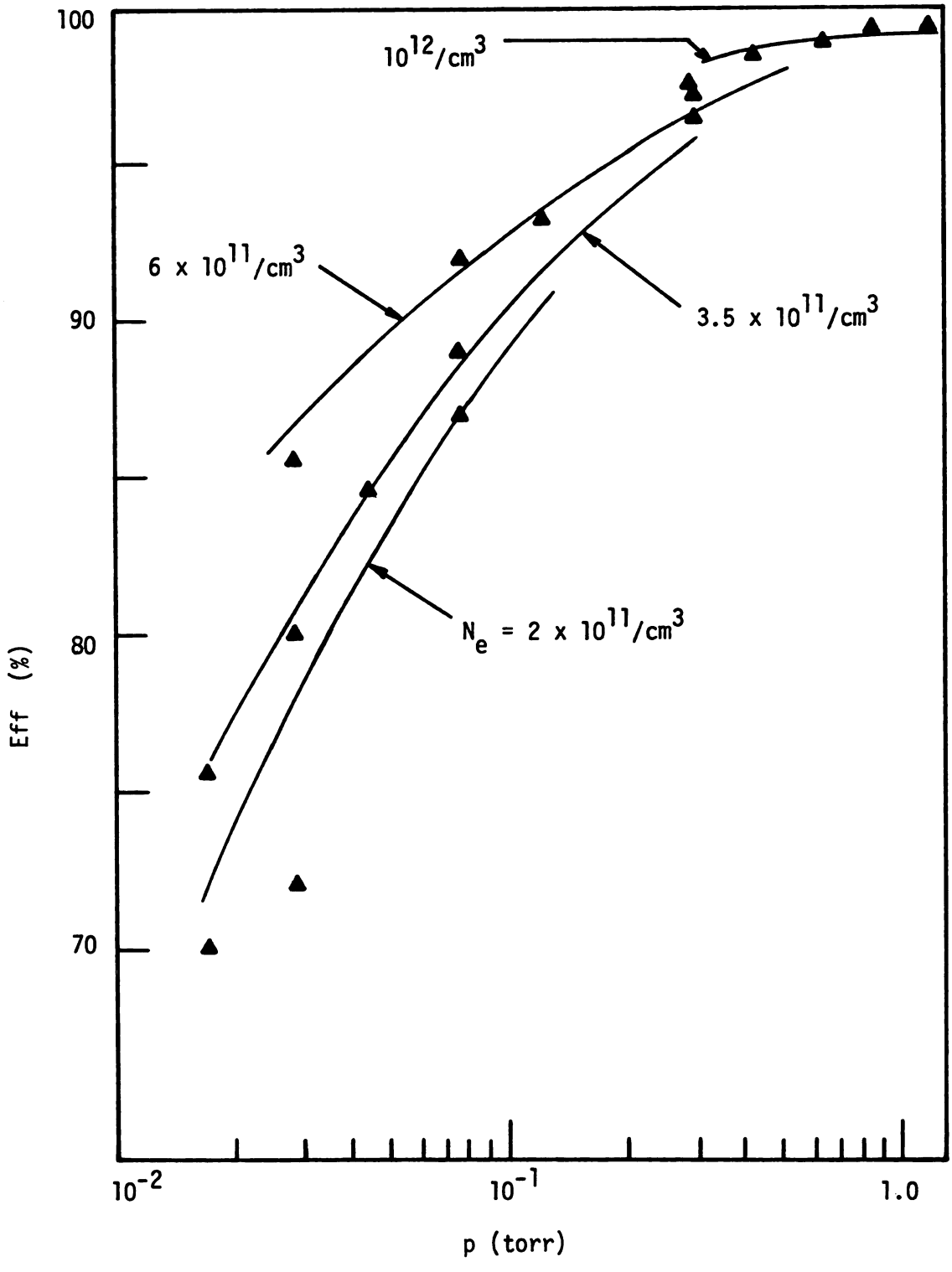

Figure B-11 Microwave coupling efficiency, Eff, versus pressure in the 13 mm tube.

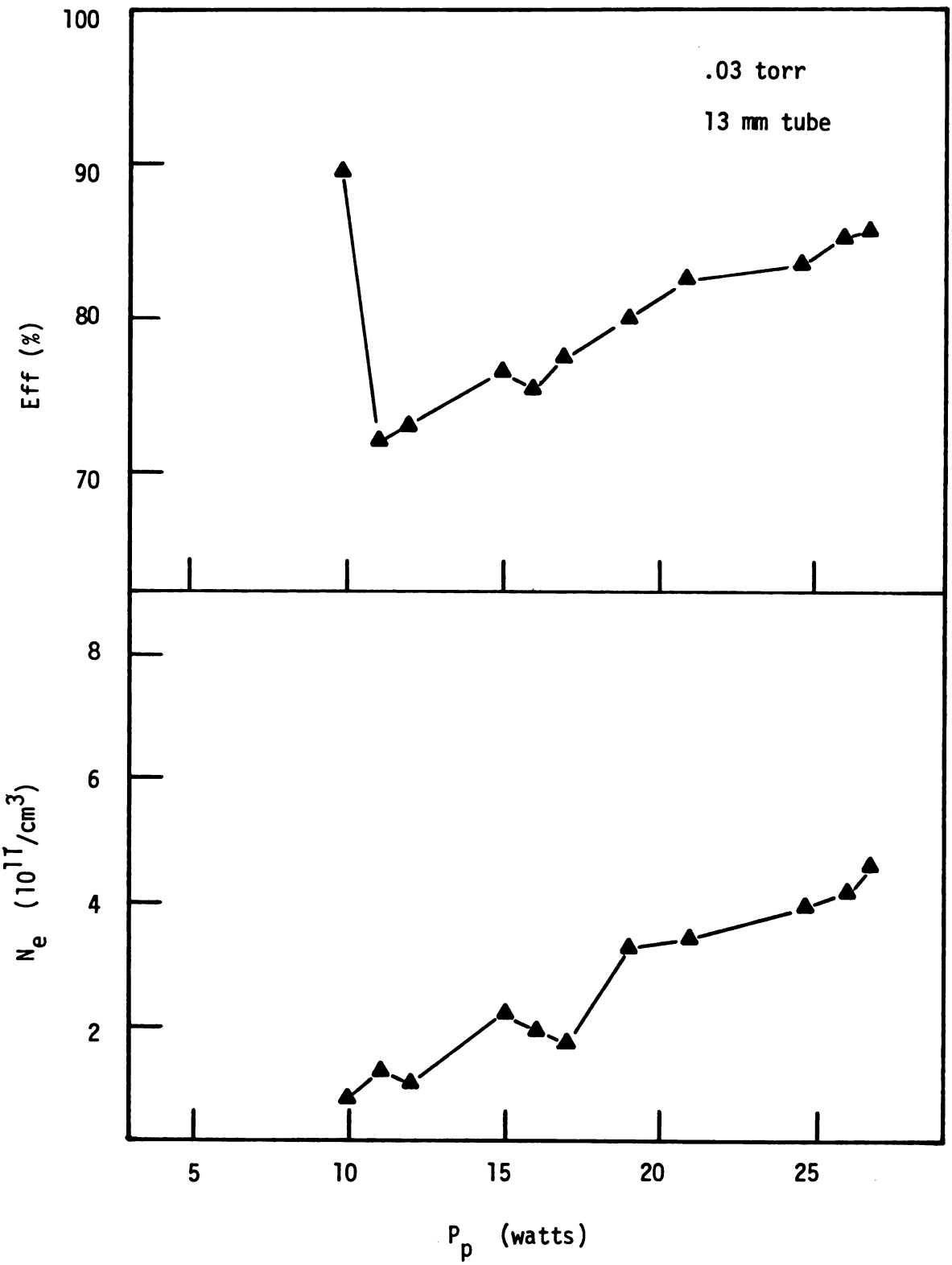

Figure B-12 Microwave coupling efficiency, Eff, and electron density N_e, versus absorbed power in the discharge, P_p, at .03 torr.

other data points. In a 25 mm i.d. tube at .02 torr, a similar unusually high value of Eff was found near the electron density where $\omega_p = \omega$. In this tube, the change in Eff was measured to be from 60% for an N_e slightly lower than $\omega_p = \omega$ to 98% when N_e was increased to about $\omega_p = \omega$ (by a slight adjustment of the cavity length). In this case, E_{rw} dropped from 113 v/cm to 27 v/cm while the power absorbed in the cavity actually increased.

The dominant electrogmagnetic mode in the cavity when the phenomena described above occurred was still verified to be the TM_{012} mode by the measured axial distribution of $|E_r|^2$ along the wall and by the start up and tuning process. Thus, the unusually high efficiencies described above were probably not due to a change in the cavity EM mode and were therefore accurately measured. The high efficiencies near $\omega_p = \omega$ were attributed to a transverse resonance in the plasma column which is predicted by the type of plasma/waveguide analysis described in Chapter V [28]. This explanation was supported by an observation on how the axial variation of light emission changed from that of Figure B-1. As shown in Figure B-13, the regions of intense plasma were located near the axial position of high $|E_r|$. This would be likely to occur if the phenomenon was a transverse resonance.

B-5 Conclusions and Recommendations

Microwave discharge properties are affected by discharge tube size. For a constant pressure and constant P_p/L: (1) average power density and electron density increase as the tube diameter decreases and (2) unloaded cavity Q and effective collision frequency remain about constant. For small tube diameters at low pressures, values of ν_e can be higher than

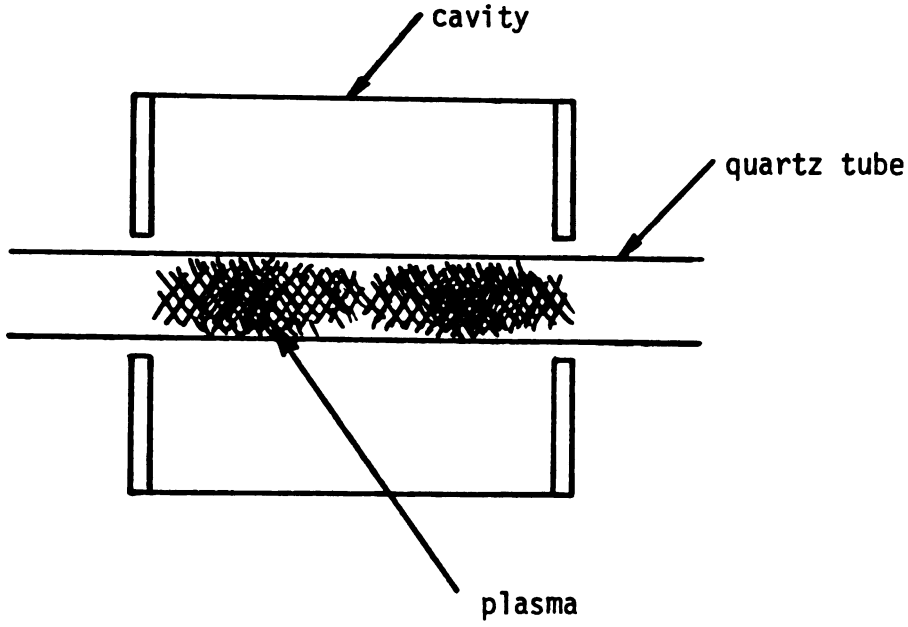

Figure B-13 Change in discharge appearance in the TM_{012} mode for the high efficiency point in Figure B-12.

expected from values in larger tube sizes at the same pressure. These higher values may reflect heating mechanisms other than electron-neutral collisions and should be investigated further.

Electron temperatures in low pressure argon microwave discharges appear to be of the same order of magnitude as electron temperatures predicted by positive column theory. T_e determined by this investigation agreed well with values determined by Langmuir probes in the p_oR range of .08 - 1.0 torr-cm. Thus, the overall measurement technique used in this dissertation appears to be valid, especially for pressures higher than about .5 torr. Electron temperatures of p_oR less than .08 torr-cm should be investigated further by both techniques and possibly with a third diagnostic method.

Effective electric field strengths in argon microwave discharges also behave in a fashion similar to that predicted by positive column theory. This should be investigated further and the values obtained in this investigation should be compared with experimental E-field strengths in d.c. discharges.

Microwave coupling efficiencies generally decrease with decreasing pressure. At a constant pressure, efficiencies generally increase with increasing electron density. A resonance phenomenon near an electron density where $\omega_p = \omega$ appears to enhance microwave coupling efficiencies at low pressures. An increase in efficiency from 60% to 98% was attributed to this phenomenon with only a slight change in electron density. This resonance phenomenon and coupling efficiencies at lower gas pressures than those considered in this investigation need further experimental and analytical work. The use of cyclotron resonance (with a d.c. magnetic field present in the discharge) to enhance microwave coupling

efficiencies should also be investigated.

The overall system efficiency of coupling microwave power to a discharge is limited by the coupling efficiency defined in this dissertation. In a practical device, reflected power has to be reduced to only a small fraction of the incident power to approach the limiting efficiencies. For high Q plasma/cavity operation (i.e. $Q_u > 1000$), a very well filtered microwave source is required to match impedance at the resonant frequency. Experiments similar to those described in this Appendix, but at lower gas pressures, will require a better filtered source than was used in these experiments.

APPENDIX C

APPENDIX C

BASIC EQUATIONS

C-1 TM_{012} Mode Fields of the Ideal Empty Cavity

Consider an axially uniform, circular waveguide of radius d having perfectly conducting walls. The fields of the cavity mode can be obtained by a superposition of forward and backward traveling waves. Denote ψ^+ as the forward wave in the TM_{01} waveguide mode and ψ^- as the backward traveling wave. Solving equations 5.4, 5.5 and 5.6 (rewritten in terms of ordinary Bessel functions and noting that there is only one region interior to the waveguide):

$$\psi^+(r,z) = \frac{A}{2} J_0(k_c r) e^{-j\beta z}$$

$$\psi^-(r,z) = \frac{A}{2} J_0(k_c r) e^{j\beta z}$$

where A/2 is an amplitude coefficient, J_0 is the ordinary Bessel function of the first kind of order zero and k_c was determined by the boundary condition at the metal wall (r = d):

$$k_c = \frac{X_{01}}{d}$$

where X_{01} is the first zero of $J_0(x)$ and $X_{01} = 2.405$.

The fields associated with each of these waves are:

$$E_z^+ (r,z) = \frac{A}{2} J_0(k_c r)\, e^{-j\beta z}$$

$$E_r^+ (r,z) = \frac{A}{2} \frac{j\beta}{k_c} J_1(k_c r)\, e^{-j\beta z}$$

$$H_\phi^+ (r,z) = \frac{A}{2} \frac{j\omega\varepsilon}{k_c} J_1(k_c r)\, e^{-j\beta z}$$

and

$$E_z^- (r,z) = \frac{A}{2} J_0(k_c r)\, e^{j\beta z}$$

$$E_r^- (r,z) = -\frac{A}{2} \frac{j\beta}{k_c} J_1(k_c r)\, e^{j\beta z}$$

$$H_\phi^- (r,z) = \frac{A}{2} \frac{j\omega\varepsilon}{k_c} J_1(k_c r)\, e^{j\beta z}$$

The superposition of these two waves (i.e. $\vec{E} = \vec{E}^+ + \vec{E}^-$ and $\vec{H} = \vec{H}^+ + \vec{H}^-$) gives:

$$E_z (r,z) = A J_0(k_c r) \cos \beta z$$

$$E_r (r,z) = A \frac{\beta}{k_c} J_1(k_c r) \sin \beta z$$

$$H_\phi (r,z) = A \frac{j\omega\varepsilon}{k_c} J_1(k_c r) \cos \beta z$$

The TM_{012} mode can thus be formed by placing perfectly conducting shorts at z = 0 and z = L with the requirement that:

$$\beta = \frac{2\pi}{L}$$

Note that β is purely real for the ideal cavity mode. Figure C-1 describes the axial and radial distributions of E_r and E_z for the TM_{012} mode assuming that the excitation frequency was 2.45 GHz, d = 8.9 cm and L = 14.4 cm. H_ϕ has a radial distribution similar to E_r, an axial distribution similar to E_z and is 90^o out of time phase with $\vec{E}$.

C-2 Characteristic Equation Used in the Analysis of Chapter V

Equation 5.7 is the characteristic equation pertaining to the geometry of Figure 5.3. The form of equation 5.7 is described in this section and the notation is fully defined in Section 5.3. The plasma/quartz/waveguide dimensions (i.e. a,b,c,d) are defined in Figure 5.3.

Define:

$$A_{11} = I_0(k_{c2}b) - \frac{C_1}{C_2} K_0(k_{c2}b)$$

$$A_{12} = - I_0(k_{c3}b) + \frac{C_3}{C_4} K_0(k_{c3}b)$$

$$A_{21} = \frac{\varepsilon_2}{k_{c2}} [I_1(k_{c2}b) + \frac{C_1}{C_2} K_1(k_{c2}b)]$$

$$A_{22} = \frac{-\varepsilon_3}{k_{c3}} [I_1(k_{c3}b) + \frac{C_3}{C_4} K_1(k_{c3}b)]$$

where:

$$C_1 = \frac{\varepsilon_1}{k_{c1}} I_1(k_{c1}a) \frac{I_0(k_{c2}a)}{I_0(k_{c1}a)} - \frac{\varepsilon_2}{k_{c2}} I_1(k_{c2}a)$$

$$C_2 = \frac{\varepsilon_1}{k_{c1}} I_1(k_{c1}a) \frac{K_0(k_{c2}a)}{I_0(k_{c1}a)} + \frac{\varepsilon_2}{k_{c2}} K_1(k_{c2}a)$$

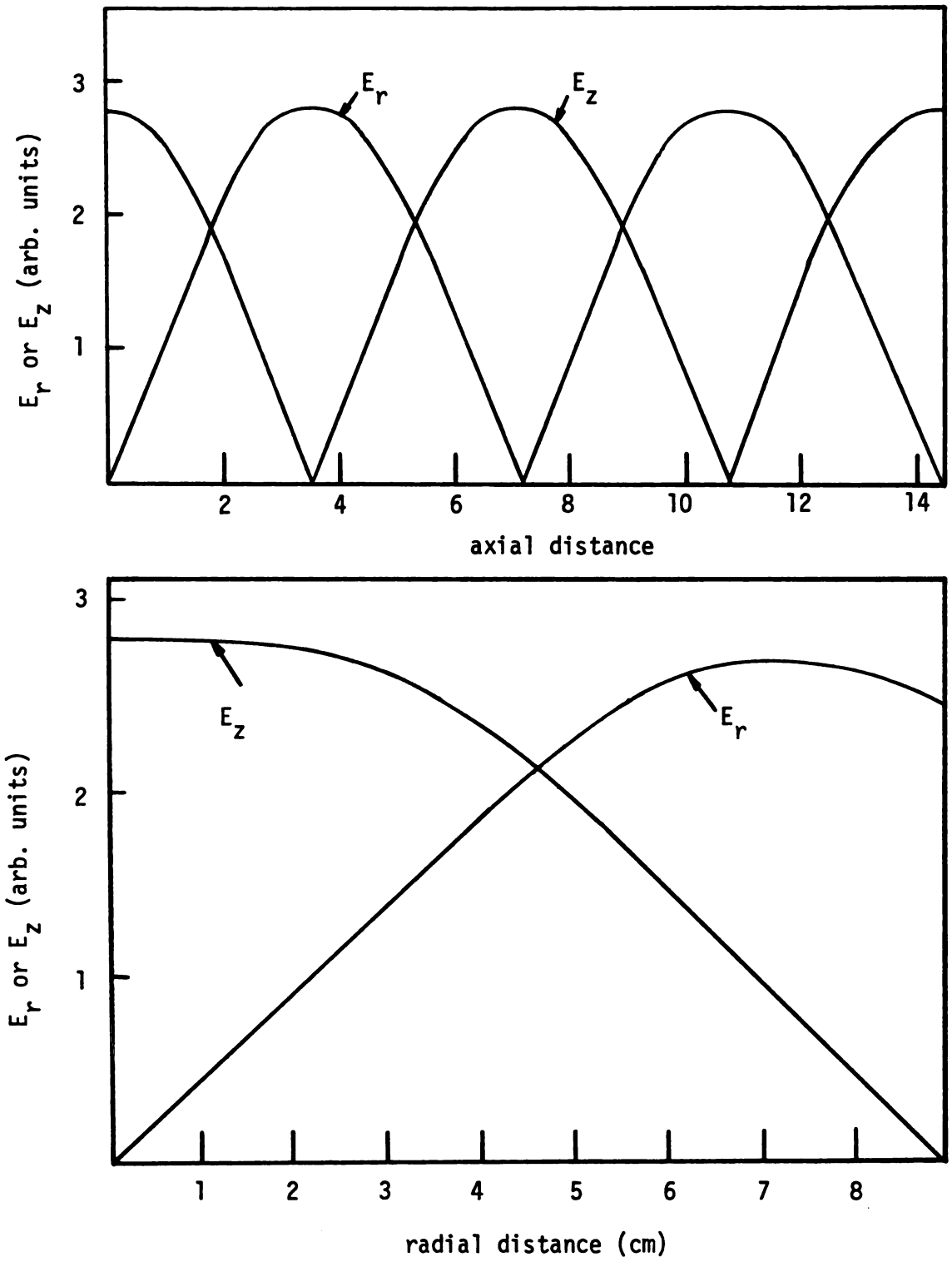

Figure C-1 Theoretical radial and axial distributions of E_r and E_z in the TM_{012} mode.

$$C_3 = \frac{\varepsilon_4}{k_{c4}} \frac{C_6}{C_5} I_0(k_{c3}c) + \frac{\varepsilon_3}{k_{c3}} I_1(k_{c3}c)$$

$$C_4 = \frac{\varepsilon_4}{k_{c4}} \frac{C_6}{C_5} K_0(k_{c3}c) - \frac{\varepsilon_3}{k_{c3}} K_1(k_{c3}c)$$

and where

$$C_5 = I_0(k_{c4}c) - \frac{I_0(k_{c4}d)}{K_0(k_{c4}d)} K_0(k_{c4}c)$$

$$C_6 = - [I_1(k_{c4}c) + \frac{I_0(k_{c4}d)}{K_0(k_{c4}d)} K_1(k_{c4}c)]$$

The characteristic equation is:

$$A_{11} A_{22} - A_{12} A_{21} = 0$$

where $f(\beta,\varepsilon_1)$ in equation 5.7 is thus:

$$f(\beta,\varepsilon_1) = A_{11} A_{22} - A_{12} A_{21}$$

REFERENCES

REFERENCES

1. R. Fritz, "An Experimental Investigation of the Characteristics of RF Surface Wave Generated Plasmas", MS Thesis, Michigan State University, 1979.

2. J. Asmussen and J. Rogers, "An Assessment of the Potential Application of Microwave Discharges to Electric Propulsion Engines", MSU/NASA Lewis Research Center Conference on Advanced Propulsion Concepts Using Time Varying EM Fields, Michigan State University, Feb. 23-25 1982.

3. J.D. Cobine and D.A. Wilbur, "The Electronic Torch and Related High Frequency Phenomena", J. Appl. Phys. 22(6), 835-841, June 1951.

4. S. Miyake, S. Takeuchi and Y. Arata, "Experimental Investigation of Coaxial Microwave Plasmatron in Nitrogen Gas", Jap. J. Appl. Phys. 13(2), 296-305, February, 1974.

5. J. Rogers and J. Asmussen, "The Experimental Production of Microwave Plasma Filaments and Discharges at High Pressure, 1981 IEEE International Conference on Plasma Science, Paper 5E4, May 18-20, 1981.

6. Y. Arata, S. Miyake, A. Kobayashi and S. Takeuchi, "Research of a Stationary High Power Microwave Plasma at Atmospheric Pressure", J. Phys. Soc. Japan 40(5), 1456-1461, May 1976.

7. J. Janca, "Spectral Diagnostics of a Unipolar High Frequency Discharge Excited in Nitrogen and Argon at Pressures From 1-12 ATM". Czech. J. Phys. B17(9), 761-772, 1967.

8. V.M. Batenin, V.S. Zrodnikov, V.K. Roddatis and V.F. Chinnov, "Spectroscopic Investigation of a Microwave Discharge in Hydrogen", High Temp. 13(2), 250-257, March - April 1975.

9. P.L. Kapitza, "Free Plasma Filament in a High Frequency Field at High Pressure", Sov. Phys. JETP 30(6), 973-1224, June 1970.

10. J. Asmussen, Jr., R. Mallavarpu, J.R. Hamann and H.C. Park, "The Design of a Microwave Plasma Cavity", Proc. IEEE 62(1), 109-117, Jan. 1974.

11. R. Mallavarpu, J. Asmussen and M.C. Hawley, "Behavior of a Microwave Cavity Discharge Over a Wide Range of Pressures and Flow Rates", IEEE Transactions on Plasma Science PS6(4), 341-354, December 1978.

12. P.L. Kapitza and S.I. Filamonov, "Apparatus for the Production of a Free Plasma Filament. Determination of the Current and Resistance

of the Filament", Sov. Phys. JETP 34(3), 542-553, March 1972.

13. B.M. Dymshits and Ya P. Koretskii, "Temperature of a Free Plasma Filament in a High Frequency Field at High Pressure", Opt. Spect. 33 (1), 17-18, July 1972.

14. Y. Arata, S. Miyake and A. Kobayashi, "High Power Microwave Discharge in Atmospheric Hydrogen Gas Flow", J. Phys. Soc. Japan 44(3), 998-1003, March 1978.

15. M. Moisan, R. Pantel and J. Hubert, "Propagation of a Surface Wave Sustaining a Plasma Column at Atmospheric Pressure", Internal Report, Dept. of Physics and Dept. of Chemistry, University of Montreal, May 1980.

16. J. Rogers and J. Asmussen, "Standing Waves Along a Microwave Generated Surface Wave Plasma", IEEE Trans. on Plasma Science PS10(1), 11-16, March 1982.

17. J. Hubert, M. Moisan and A. Ricard, "A New Microwave Plasma at Atmospheric Pressure", Spectrochimica Acta 33B, 1-10, 1979.

18. M. Moisan, P. Leprince, C. Beaudry and E. Bloyet, U.S. Patent No. 4,049,940.

19. J.D. Jackson, Classical Electrodynamics, Wiley, New York, 1975.

20. R.F. Harrington, Time-Harmonic Electromagnetic Fields, McGraw-Hill, New York, 1961.

21. H.A. Atwater, Introduction to Microwave Theory, McGraw-Hill, New York, 1962.

22. D.D. King, Measurements at Centimeter Wavelength, Boston Technical Publishers, 1965.

23. S.C. Brown and D.J. Rose, "Methods of Measuring the Properties of Ionized Gases at High Frequencies. I. Measurements of Q", J. Appl. Phys 23(7), 711-718, July 1952.

24. B. Agdur and B. Enander, "Resonances of a Microwave Cavity Partially Filled with a Plasma", J. Appl. Phys. 33(2), 575-581, February 1962.

25. J. Asmussen, unpublished experimental results and personal photographs.

26. D.J. Rose and S.C. Brown, "Methods of Measuring the Properties of Ionized Gases at High Frequencies. III. Measurement of Discharge Admittance and Electron Density", J. Appl. Phys. 23(9), 1028-1032, September 1952.

27. J.L. Shohet and C. Moskowitz, "Eigenvalues of a Microwave-Cavity-Lossy-Plasma System", J. Apply. Phys. 36(5), 1756-1759, May 1965.

28. R. Mallavarpu, "An Investigation of the Electromagnetic Behavior of a Microwave Plasma Source Over a Wide Range of Pressures and Flow Rates", PhD Dissertation, Michigan State University, 1976.

29. R.E. Collin, Field Theory of Guided Waves, McGraw-Hill, New York, 1960.

30. B.S. Tanenbaum, Plasma Physics, McGraw-Hill, New York, 1967.

31. B.E. Cherrington, Gaseous Electronics and Gas Lasers, Pergamon Press, Oxford, 1979.

32. R.F. Whitmer and G.F. Herrmann, "Effects of a Velocity-Dependent Collision Frequency on Wave Plasma Interactions", Phys. Fluids 9(4), 768-773, April 1966.

33. W.G. Vincenti and C.H. Kruger, Jr., Physical Gas Dynamics, Wiley, New York, 1965.

34. J.G. Eden and B.E. Cherrington, "Radial Neutral Gas Temperature and Density Profiles in Low Pressure Argon Discharges", J. Appl. Phys. 44(11), 4920-4926, November 1973.

35. S.C. Brown, Basic Data of Plasma Physics, MIT Technology Press and John Wiley & Sons, New York, 1959.

36. D.A. McPherson, R.K. Feeney and J.W. Hooper, "Microwave Transient-Response Measurements of Elastic Momemtum-Transfer Collision Frequencies in Argon", Phys. Rev. A 13(1), 167-179, January 1976.

37. V.M.M. Glaude, M. Moisan and R. Pantel, "Axial Electron Density and Wave Power Distributions Along a Plasma Column Sustained by the Propagation of a Surface Wave", J. Appl. Phys 51(11), 5693-5698, November 1980.

38. L.J. Varnerin, Jr. and S.C. Brown, "Microwave Determinations of Average Electron Energies and the First Townsend Coefficient in Hydrogen", Phys. Rev. 79(6), 946-951, September 15, 1950.

39. Yu, B. Golobovskii,Yu. M. Kagan and R.I. Lyagushchenko, "Spectroscopic and Probe Investigation of a Contracted Discharge Column", Opt. Spect. 20(4), 317-320, April 1966.

40. I. Kato, H. Tsuchida and M. Nagai, "Radial Distribution of Excited Atoms in a New Coaxial Line Type Microwave CW Discharge Tube", J. Appl. Phys. 51(10), 5312-5315, October 1980.

41. T.M. Sipe and D.P. Nyquist, "An Integral Operator Based Perturbation Analysis of Surface Wave Modes on Heterogeneous Dielectric Waveguides", Paper B7-7, Digest of the National Radio Science Meeting, January 12-16, 1981.

42. A. Von Engel, Ionized Gases, Clarendon Press, Oxford, 1955.

43. R.N. Franklin, Plasma Phenomena in Gas Discharges, Clarendon Press, Oxford, 1976.